FERMILAB-MASTERS-2024-04

Muon Time-of-Flight studies for cosmic background rejection in the Short Baseline Near Detector

Annalea Corallo

Università degli Studi di Ferrara
Department of Physics and Earth Sciences

Master's degree in Physics

Academic Year 2024 - 2025

Supervisor	Prof. Roberto Calabrese
Co-Supervisors	Dr. Michelle Stancari
	Dr. Henry Lay
	Dr. Lan Ngyuen

Abstract

The Short-Baseline Neutrino (SBN) program at Fermilab is a cutting-edge project in experimental neutrino physics. One of its main goals is to systematically investigate the possible existence of eV-scale sterile neutrinos. This phenomenon has been hypothesized to explain some anomalies found in short-range experiments and, if confirmed, would imply a substantial extension of the Standard Model.
SBN also offers an important opportunity to deepen the understanding of neutrino-nucleus interactions in the GeV energy range, through the use of Liquid Argon Time Projection Chambers (LArTPC) detectors, a fundamental technology also for the future DUNE experiment.

The SBN experimental infrastructure consists of three detectors aligned along the Booster Neutrino Beamline at Fermilab. Among them, the detector located closest to the neutrino source, SBND (Short-Baseline Near Detector), positioned approximately 110 meters from the target, plays a key role in directly characterizing the initial neutrino flux. This allows for a direct comparison with the measurements from the far detector, ICARUS, located about 600 meters from the source, in order to search for potential signs of anomalous neutrino oscillations.

My master's thesis focuses on the commissioning and characterization activities of the SBND detector, with particular reference to the Cosmic Ray Tagger (CRT). The CRT is a subsystem for identifying and rejecting events produced by cosmic rays, which constitute the main source of background for surface experiments like SBND.
The activity began with the commissioning of the final components of the detector, as well as their validation to verify their correct functioning and signal acquisition. A central part of my work involved studying the veto efficiency of the CRT system, analyzing the rate of cosmic ray-induced events to quantify any loss of neutrino-induced events caused by cosmic background. This allowed for a more precise evaluation of the systematic impact of the CRT on the useful physics sample.

A further phase of my analysis involved an in-depth study of the temporal correlation between the CRT signals and those acquired by the LArTPC's internal photodetector system, consisting of photomultiplier tubes and X-ARAPUCA devices. The objective is to explore the possibility of using combined temporal information as an additional criterion for discriminating between cosmic signals and signals

genuinely due to neutrino interaction. Preliminary results indicate the presence of characteristic temporal signatures that could be exploited to improve event selection and increase the purity of the neutrino-induced sample.

These methodologies will certainly contribute to the optimization of SBND analysis strategies and, more generally, to a better understanding of background mechanisms in next-generation LArTPC experiments.

Sommario

Il Short-Baseline Neutrino program (SBN) presso il Fermilab è un progetto all'avanguardia nella fisica sperimentale dei neutrini. Uno dei suoi principali obiettivi è indagare sistematicamente la possibile esistenza di neutrini sterili con massa nell'intervallo degli eV. Questo fenomeno è stato ipotizzato per spiegare alcune anomalie osservate in esperimenti a corto raggio e, se confermato, implicherebbe un'estensione sostanziale del Modello Standard. Il programma SBN offre inoltre un'importante opportunità per approfondire la comprensione delle interazioni neutrino-nucleo nell'intervallo di energie dell'ordine del GeV, grazie all'utilizzo di camere a proiezione temporale in Argon liquido (LArTPC), una tecnologia fondamentale anche per il futuro esperimento DUNE.

L'infrastruttura sperimentale di SBN è costituita da tre rivelatori allineati lungo la linea di fascio di neutrini Booster al Fermilab. Tra questi, il rivelatore più vicino alla sorgente di neutrini, SBND (Short-Baseline Near Detector), posizionato a circa 110 metri dal bersaglio, riveste un ruolo chiave nella caratterizzazione diretta del flusso iniziale di neutrini. Questo consente un confronto diretto con le misure del rivelatore più distante, ICARUS, situato a circa 600 metri dalla sorgente, al fine di cercare eventuali segnali di oscillazioni anomale dei neutrini.

La mia tesi magistrale si concentra sulle attività di commissioning e caratterizzazione del rivelatore SBND, con particolare riferimento al sotto rivelatore Cosmic Ray Tagger (CRT). Il CRT è un sottosistema per l'identificazione e il rigetto degli eventi prodotti da raggi cosmici, che costituiscono la principale sorgente di fondo negli esperimenti in superficie come SBND. L'attività è iniziata con la messa in funzione dei componenti finali del rivelatore e la loro validazione, per verificarne il corretto funzionamento e l'acquisizione dei segnali. Una parte centrale del mio lavoro ha riguardato lo studio dell'efficienza di veto del sistema CRT, analizzando il tasso di eventi indotti da raggi cosmici per quantificare eventuali perdite di eventi da neutrino causate dal fondo cosmico. Questo ha permesso una valutazione più precisa dell'impatto sistematico del CRT sul campione utile di eventi fisici.

Una fase successiva della mia analisi ha previsto uno studio approfondito della correlazione temporale tra i segnali del CRT e quelli acquisiti dal sistema di fotorivelazione interno alla LArTPC, costituito da tubi fotomoltiplicatori e dispositivi X-ARAPUCA. L'obiettivo è esplorare la possibilità di utilizzare l'informazione temporale combinata come criterio aggiuntivo per discriminare tra segnali cosmici e

segnali realmente dovuti all'interazione dei neutrini. I risultati preliminari indicano la presenza di firme temporali caratteristiche che potrebbero essere sfruttate per migliorare la selezione degli eventi e aumentare la purezza del campione indotto dai neutrini.

Queste metodologie contribuiranno certamente all'ottimizzazione delle strategie di analisi di SBND e, più in generale, a una migliore comprensione dei meccanismi di fondo nei futuri esperimenti LArTPC di nuova generazione.

Contents

1 General introduction

In recent years, Liquid Argon Time Projection Chambers (LArTPCs) have become a leading technology in neutrino detection, offering exceptional spatial resolution, particle identification, and calorimetric performance. These detectors are rapidly scaling in both size and complexity, culminating in large-scale experiments such as the Deep Underground Neutrino Experiment (DUNE), which will employ multi-kiloton LArTPC modules to perform precision studies of neutrino oscillations. Over the coming decade, LArTPC-based experiments are expected to provide critical insights into some of the most fundamental questions in neutrino physics.

The DUNE experiment will focus on long-baseline neutrino oscillation measurements, with the goal of determining the neutrino mass hierarchy and probing the presence of charge-parity (CP) violation in the lepton sector. In parallel, the Short-Baseline Neutrino (SBN) program at Fermilab aims to investigate a series of anomalous results observed in previous short-baseline experiments, which have been interpreted as potential signatures of physics beyond the Standard Model (BSM). Among these, the long-standing excess of low-energy electron-like events observed by the MiniBooNE and LSND experiments has attracted particular interest.

This thesis presents an in-depth analysis of the timing characteristics of two of the three subsystems that make up the Short-Baseline Near Detector (SBND), the LArTPC detector at the near site of the SBN program. In particular, the work focuses on the Cosmic Ray Tagger (CRT), a fundamental component for surface-based experiments, used as an external veto system to identify and reject cosmic-induced signals originating outside the active TPC volume. The temporal response of the CRT is studied in detail and compared with that of the Photon Detection System (PDS), another key subsystem surrounding the TPC, which detects the prompt scintillation light produced by particle interactions in liquid argon. By analyzing and comparing the timing distributions of these two subsystems, this work investigates their potential to serve as a combined veto tool, capable of discriminating between external background events and genuine neutrino interactions occurring inside the TPC.

The first part of the thesis is dedicated to the physics context and experimental framework. After presenting an overview of the current status of neutrino physics, with particular emphasis on the sterile neutrino hypothesis and its relevance to low-

energy anomalies, the LArTPC detection technology is introduced and discussed in detail, with a specific focus on its application within the SBN program.

A detailed description of the SBND detector follows, highlighting its 112-ton active volume, high-precision reconstruction capabilities, and high-efficiency photon detection system. SBND, located 110 meters downstream of the BNB target, began data collection in July 2024, following the successful commissioning of all subsystems. Its combination of high mass, proximity to the neutrino source, and advanced instrumentation makes it a powerful platform for BSM searches and precision neutrino studies.

The second part of this thesis presents the original work I carried out during my research activity. In the summer of 2024, I actively contributed to the installation, commissioning and validation of the CRT system, playing a key role in its full integration into the detector and the start of joint data-taking operations. As part of the initial validation phase, I measured the veto efficiency of the CRT by comparing the rate of cosmic rays with the rate of neutrino spills. After completing the commissioning activities, I focused on a dedicated analysis of the temporal distributions of the CRT and PDS signals. This analysis, which is described in detail in the latter chapters, outlines the methodology I developed to extract and correlate timing information from the two subsystems, and investigates how such timing correlations can be exploited to improve the rejection of cosmic-induced background in the selection of neutrino interactions.

Finally, the thesis concludes with a discussion of the results and their implications for future data analyses and detector performance optimization in SBND and the broader SBN program.

Part I

Neutrino Physics and Experimental Context

2 Neutrino Physics Overview

2.1 Neutrinos in the Standard Model: from discovery to today

The story of the neutrino is one of the most intriguing in elementary particle physics, marked by a unique journey from theoretical postulation to experimental confirmation and, ultimately, to reshaping our understanding of the fundamental laws of nature. Neutrinos, neutral particles that interact only weakly, were first theorized to resolve a serious problem in the early 20th-century physics concerning the phenomenon of beta decay.

The initial puzzle emerged from the observation of beta decay, a form of radioactivity in which a continuous energy spectrum of electrons was emitted. This spectrum, first identified by J. Chadwick in 1914 and later confirmed by Ellis and Wooster, stood in stark contrast to the discrete energy lines observed in alpha and gamma decays (see Figure 2.1). At the time, beta decay was expected to be a two-body process, which would imply that the emitted electron should carry a fixed kinetic energy, resulting in a discrete spectrum. Instead, experimental results revealed a continuous distribution, a hallmark of three-body decays, where the available energy is shared among multiple particles. This unexpected behavior posed a serious challenge to the fundamental principles of energy conservation and spin statistics within the atomic nucleus.

To reconcile these inconsistencies, Wolfgang Pauli proposed a radical solution in a letter dated December 4, 1930. He suggested the existence of a new, neutral, weakly interacting spin-1/2 particle, which we now know as the neutrino, emitted alongside the electron during beta decay:

$$n \longrightarrow p + e^- + \bar{\nu}_e$$

$$p \longrightarrow n + e^+ + \nu_e$$

This hypothetical particle, escaping detection due to its elusive nature, would carry away the missing energy and angular momentum, thus preserving the conservation laws. Pauli initially referred to it as a "neutron" and speculated its mass to be on the order of the electron mass, or at least no larger than 0.01 proton masses.

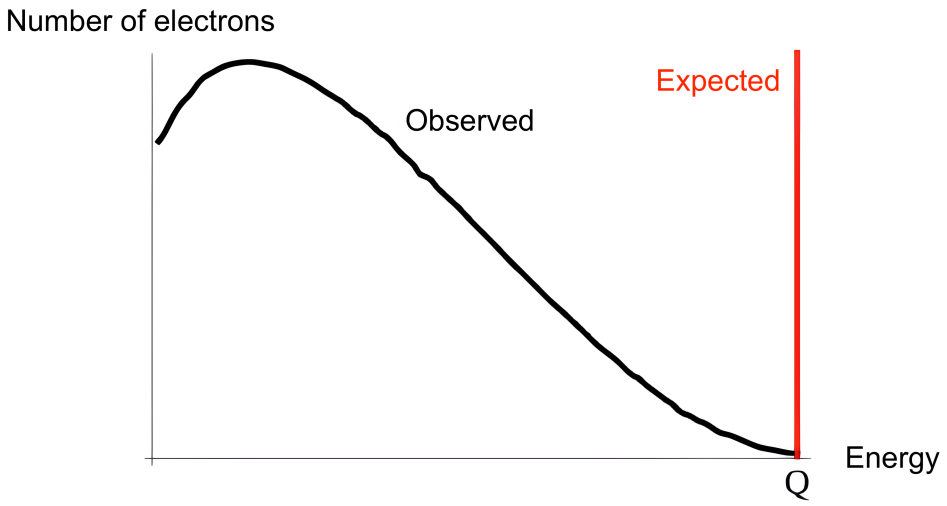

Figure 2.1: The image shows a beta decay spectrum. The observed spectrum (black curve) is continuous, with electrons emitted across a range of energies. This contrasts with the initially expected spectrum (red line), which predicted all electrons would be emitted with a single, specific energy Q. This discrepancy led to the discovery of the neutrino, a particle that carries away the "missing" energy, explaining the continuous nature of the observed spectrum.

Following Chadwick's discovery of the known neutron in 1932, Enrico Fermi renamed Pauli's particle the neutrino and, in 1934, formulated a successful theory of beta decay [14].

Fermi's theory, developed by analogy with quantum electrodynamics (QED), described the weak interaction as a local coupling of four spin-1/2 fields. This theory, even today, remains valid for describing most low-energy weak processes and is considered a low-energy limit of the later electroweak model.

Despite its theoretical success, the neutrino remained a phantom for decades. Its direct experimental discovery came in 1956, when Clyde Cowan and Frederick Reines detected antineutrinos ($\bar{\nu}_e$) emitted from a nuclear reactor. This groundbreaking experiment, originally envisioned using a nuclear bomb explosion, provided the first concrete evidence for the existence of these elusive particles [12].

A pivotal development in understanding the neutrino's fundamental properties occurred with the discovery of parity violation in weak interactions in 1957. This led to the formulation of the two-component theory of massless neutrinos by Landau,

Lee and Yang, and Salam. In 1958, the Goldhaber experiment directly measured the helicity of the electron neutrino, confirming that it was left-handed (polarization opposite to its motion), in agreement with the two-component theory. This result solidified the V-A (Vector minus Axial-vector) structure of weak interactions, described by the combination $\gamma_\mu(1-\gamma_5)$, which accurately represented experimental data.

The landscape of neutrinos further diversified with the discovery that there were different "flavors" of neutrinos. In 1962, a pioneering accelerator neutrino experiment at Brookhaven National Laboratory, led by Lederman, Schwartz, and Steinberger, demonstrated that the muon neutrino (ν_μ) was distinct from the electron neutrino (ν_e). This was established by observing that muon-like events were produced when a beam of muon neutrinos interacted with matter, while electron-like events were rare, thus proving that $\nu_\mu \neq \nu_e$. Much later, the tau neutrino (ν_τ) was directly detected via charged-current interactions in the DONuT experiment in 2001 [2].

Today, neutrinos are an integral part of the Standard Model (SM) of particle physics, which describes the fundamental building blocks of matter and their interactions through three of the four known fundamental forces: electromagnetism, and the strong and weak interactions (gravity being excluded). Within the SM, neutrinos are classified as leptons and are spin-1/2 fermions, just like quarks and charged leptons (electrons, muons, and taus), as represented in Figure 2.2.

There are three known generations of neutrinos, corresponding to the three charged lepton flavors: electron neutrino (ν_e), muon neutrino (ν_μ), and tau neutrino (ν_τ). A defining characteristic of neutrinos in the SM is their participation only in the weak interaction, which is responsible for processes like beta decay.

The electroweak part of the Standard Model, unified in the Glashow-Weinberg-Salam (GWS) model, successfully describes both electromagnetic and weak interactions as manifestations of a single underlying force. This gauge theory, based on the local symmetry group $\mathrm{SU}(2)_L \times \mathrm{U}(1)_Y$, predicted the existence of weak neutral currents and the W and Z gauge bosons, all of which were subsequently discovered. In the original formulation of the SM, neutrinos were assumed to be massless, consistent with experimental observations at the time and the two-component theory of neutrinos. Furthermore, only left-handed neutrinos and right-handed antineutrinos were observed to interact [23].

However, the last few decades have seen a profound "revolution in neutrino physics". The most significant discovery is the establishment of a non-vanishing neutrino mass, a fact confirmed by numerous neutrino oscillation experiments.

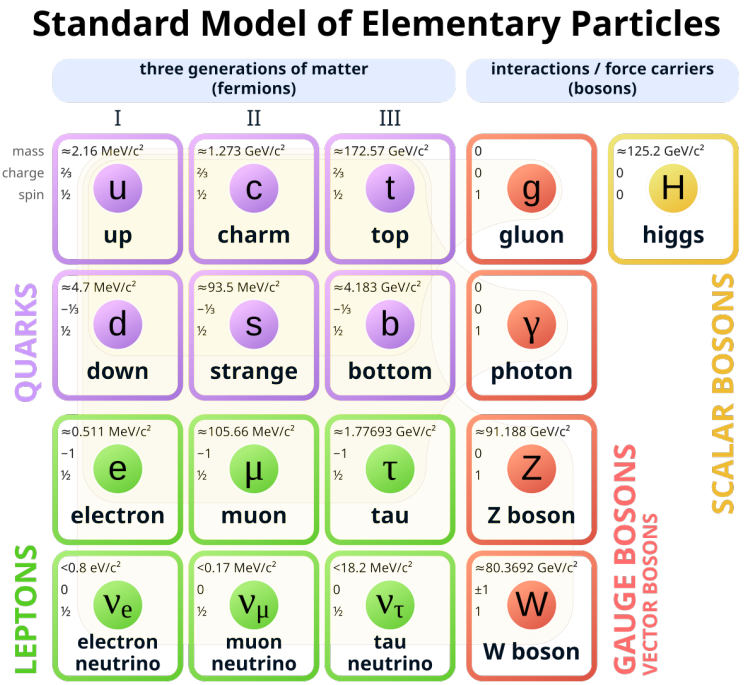

Figure 2.2: The Standard Model of Elementary Particles is the theoretical framework that explains the fundamental constituents of matter and the forces that act between them, with the exception of gravity. On the left are the fermions, which are divided into quarks and leptons. The quarks are arranged into three generations: up and down, charm and strange, top and bottom. Below the quarks are the leptons, which also appear in three generations: the electron, muon, and tau, together with their corresponding neutrinos. These are the particles that make up ordinary matter and carry electric charge or none at all in the case of neutrinos. On the right side of the diagram are the bosons, the particles responsible for mediating the fundamental interactions. The gluon is associated with the strong nuclear force, the photon with electromagnetism, while the W and Z bosons are linked to the weak nuclear force. In addition to these gauge bosons, the diagram shows the Higgs boson, a scalar particle whose field is responsible for giving mass to the elementary particles.

These experiments, such as Super-Kamiokande and the Sudbury Neutrino Observatory (SNO), definitively showed that neutrinos change flavor as they propagate, a quantum mechanical phenomenon that unequivocally requires them to have mass and to "mix". This mixing is described by a leptonic mixing matrix, analogous to the CKM matrix for quarks. The discovery of neutrino mass implies that the initial Standard Model description of massless neutrinos is incomplete and points to

physics beyond the Standard Model. Current research continues to refine measurements of neutrino mass differences and mixing parameters, seeking to determine their absolute values and whether neutrinos are Dirac or Majorana particles. The impact of massive neutrinos extends beyond particle physics, influencing our understanding of astrophysics and cosmology, including the nature of dark matter and the evolution of the universe [14].

2.2 Neutrino Oscillations and the PMNS Mixing Matrix

The journey of neutrinos, from their initial postulation to the definitive confirmation of their flavor oscillation, represents one of the most significant revolutions in modern particle physics. This phenomenon not only revealed that neutrinos are massive but also necessitated an extension of the Standard Model (SM) to accommodate these findings, leading to the development of the Pontecorvo-Maki-Nakagawa-Sakata (PMNS) mixing matrix.

2.2.1 The Discovery of Neutrino Flavor Oscillation

The concept of neutrino oscillation, a quantum mechanical phenomenon where neutrinos change from one flavor to another as they propagate, was first proposed in 1957 by Bruno Pontecorvo, inspired by the analogous K^0-$\bar{K}^0$ oscillations. Initially, Pontecorvo considered oscillations between neutrino and antineutrino states for Majorana neutrinos. Later, in 1962, Ziro Maki, Masami Nakagawa, and Shoichi Sakata considered a model involving the mixing of different neutrino flavors. This theoretical groundwork laid the foundation for understanding the solar neutrino problem and the atmospheric neutrino anomaly, which were the first experimental hints of neutrino oscillations [14].

The solar neutrino problem emerged from the observation that significantly fewer electron neutrinos (ν_e) from the Sun were detected on Earth than predicted by theoretical models of solar energy production, i.e. the Standard Solar Model. This long-standing discrepancy was definitively resolved by the Sudbury Neutrino Observatory (SNO) experiments in the early 2000s. SNO uniquely measured all three relevant interaction channels of solar neutrinos with deuterium and electrons: the charged-current (CC), sensitive only to ν_e; the neutral-current (NC), equally sensitive to all active neutrino flavors; and elastic scattering (ES), primarily sensitive to ν_e with a smaller contribution from ν_μ and ν_τ. These processes are summarized below:

- **Charged Current (CC)** interaction, sensitive only to ν_e:

$$\nu_e + d \quad \rightarrow \quad p + p + e^-$$

- **Neutral Current (NC)** interaction, sensitive to all flavors ν_e, ν_μ, ν_τ:

$$\nu_x + d \quad \rightarrow \quad p + n + \nu_x \qquad (x = e, \mu, \tau)$$

- **Elastic Scattering (ES)**, primarily sensitive to ν_e (with a smaller contribution from ν_μ, ν_τ):

$$\nu_x + e^- \quad \rightarrow \quad \nu_x + e^- \qquad (x = e, \mu, \tau)$$

The combined measurement of CC, NC, and ES interactions provided direct and model-independent evidence for neutrino flavor transformation, demonstrating that the electron neutrinos produced in the Sun were indeed arriving at Earth with a total flux consistent with the predictions of the Standard Solar Model, but had partially oscillated into muon (ν_μ) and tau (ν_τ) neutrinos [10].

Concurrently, the atmospheric neutrino anomaly pointed to a deficit of muon neutrinos produced in cosmic ray interactions in the Earth's atmosphere, particularly dependent on the zenith angle (indicating different travel distances through the Earth). The Super-Kamiokande experiment in Japan provided compelling evidence in 1998 for atmospheric neutrino oscillations, most notably ν_μ disappearance, through the observation of an up-down asymmetry in their flux. This was later confirmed by the OPERA experiment, which directly observed the appearance of tau neutrinos in a muon neutrino beam from CERN, thus proving the $\nu_\mu \rightarrow \nu_\tau$ oscillation channel [11].

Further confirmation came from reactor antineutrino experiments. The KamLAND experiment in 2002 observed the disappearance of reactor antineutrinos ($\bar{\nu}_e$) over distances of about 180 km, accompanied by an energy spectrum distortion consistent with neutrino oscillations. Subsequent reactor experiments like Daya Bay, RENO, and Double Chooz precisely measured the smallest mixing angle, θ_{13}.

Early accelerator experiments also contributed significantly to this understanding. The seminal 1962 experiment by Lederman, Schwartz, and Steinberger demonstrated that the muon neutrino was distinct from the electron neutrino. More recently, long-baseline accelerator experiments such as K2K, MINOS, T2K, and NOvA have further refined our understanding of neutrino mixing parameters.

2.2.2 The PMNS Mixing Matrix: Formal Treatment

The observation of neutrino flavor oscillations implies that the flavor eigenstates (ν_e, ν_μ, ν_τ), which participate in weak interactions, are not identical to the mass eigenstates (ν_1, ν_2, ν_3), which are the states that propagate freely with definite masses as the solutions of the Hamiltonian. Instead, each flavor eigenstate is a coherent superposition of the mass eigenstates. This relationship is formally described by the Pontecorvo-Maki-Nakagawa-Sakata (PMNS) mixing matrix:

$$U_{PMNS} = \begin{pmatrix} U_{e1} & U_{e2} & U_{e3} \\ U_{\mu 1} & U_{\mu 2} & U_{\mu 3} \\ U_{\tau 1} & U_{\tau 2} & U_{\tau 3} \end{pmatrix} \tag{2.1}$$

The PMNS matrix is a 3×3 unitary matrix that connects the flavor eigenstates to the mass eigenstates:

$$|\nu_\alpha\rangle = \sum_{i=1}^{3} U_{\alpha i}^{*} |\nu_i\rangle$$

where $\alpha = e, \mu, \tau$ represents the flavor and $i = 1, 2, 3$ represents the mass eigenstate. The elements $U_{\alpha i}$ quantify the extent to which each flavor state contains each mass state [21].

For the case of three active neutrinos, the PMNS matrix can be parameterized in terms of three mixing angles ($\theta_{12}, \theta_{13}, \theta_{23}$) and, depending on the nature of neutrinos, up to three CP-violating phases. If neutrinos are Dirac particles, there is one CP-violating phase (the Dirac phase δ_{CP}), analogous to the CKM matrix for quarks. However, if neutrinos are Majorana particles (meaning they are their own antiparticles), there are two additional CP-violating phases, known as Majorana phases (η_1, η_2). These Majorana phases, however, do not influence neutrino oscillation probabilities, as they cancel out in the expression for oscillation probability.

Consequently, for studying neutrino oscillations, the PMNS matrix can generally be expressed in a form that includes only the three mixing angles and the Dirac CP phase, accounting for the difference in the oscillations of neutrinos and antineutrinos:

$$U = \begin{pmatrix} 1 & 0 & 0 \\ 0 & c_{23} & s_{23} \\ 0 & -s_{23} & c_{23} \end{pmatrix} \begin{pmatrix} c_{13} & 0 & s_{13} e^{-i\delta_{\text{CP}}} \\ 0 & 1 & 0 \\ -s_{13} e^{i\delta_{\text{CP}}} & 0 & c_{13} \end{pmatrix} \begin{pmatrix} c_{12} & s_{12} & 0 \\ -s_{12} & c_{12} & 0 \\ 0 & 0 & 1 \end{pmatrix}$$

where $c_{ij} = \cos\theta_{ij}$ and $s_{ij} = \sin\theta_{ij}$ [15].

Values of δ_{CP} different from 0 or π would indicate CP violation in the lepton

sector, a crucial ingredient for theories explaining the matter-antimatter asymmetry in the universe.

An often convenient approximation is to consider neutrino mixing and oscillations between only two flavours. The mixing matrix in Equation 2.1 reduces to 2×2 and the probability of oscillation from one flavour to another can be expressed as:

$$P(\nu_\alpha \rightarrow \nu_\beta) = \sin^2(2\theta)\,\sin^2\left(1.27\,\frac{\Delta m^2\,[\mathrm{eV}^2]\cdot L\,[\mathrm{km}]}{E\,[\mathrm{GeV}]}\right) \tag{2.2}$$

where θ is the mixing angle, Δm^2 is the mass splitting between the two mass eigenstates, L is the distance the neutrino has propagated and E is the neutrino energy. In order for the oscillation probability $P(\nu_\alpha \rightarrow \nu_\beta)$ to be non-zero, the mass difference between neutrino states must be non-vanishing. This requirement implies that, within the three-flavour framework, at least two neutrinos must carry a non-zero mass.

The regions of the oscillation parameter space that can be explored experimentally depend on both the neutrino energy and the baseline, i.e. the distance between the source and the detector. For a fixed neutrino energy, oscillations driven by larger mass splittings are accessible at shorter baselines, while smaller splittings can be studied at longer distances. A schematic overview of the energies and baselines probed by various oscillation searches is shown in Figure 2.3.

The oscillation patterns driven by the two known mass-squared splittings, the atmospheric splitting Δm^2_{32} and the solar splitting Δm^2_{21}, are illustrated by the dashed curves in the figure.

Broadly speaking, accelerator-based neutrino experiments can be divided into two main categories: short-baseline searches, spanning distances of $\mathcal{O}(100\ \mathrm{m})$ to $\mathcal{O}(1\ \mathrm{km})$, and long-baseline searches, reaching up to $\mathcal{O}(1000\ \mathrm{km})$. Short-baseline programs, such as the Short-Baseline Neutrino (SBN) experiment (see Chapter 3), are particularly sensitive to large mass splittings and are designed to probe the region around $\Delta m^2 \sim 1\ \mathrm{eV}^2$, suggested by several anomalous experimental results. Long-baseline facilities, such as DUNE, NOνA, and T2K, instead target smaller mass splittings and aim to make precision measurements of oscillations primarily driven by Δm^2_{31}. In addition, complementary regions of parameter space are covered by atmospheric and reactor neutrino experiments.

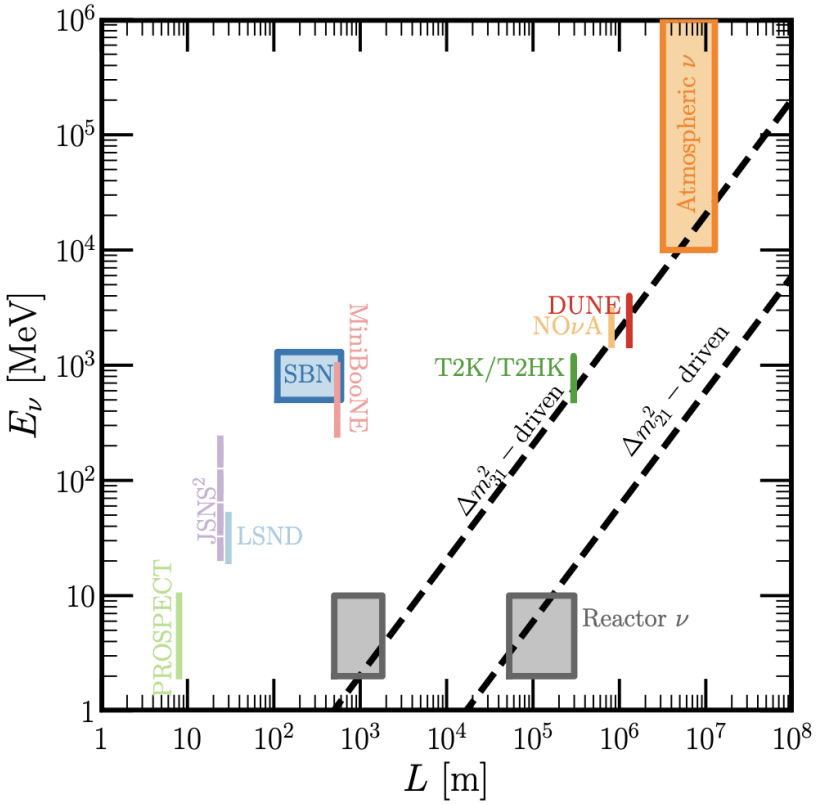

Figure 2.3: Overview of the neutrino energies and baselines covered by a variety of oscillation experiments [17].

2.2.3 Neutrino masses and mixing parameters

The discovery of neutrino oscillations demonstrated that neutrinos possess non-zero mass. Experimental results, however, constrain these masses to be extremely small. The most recent direct measurements of the absolute electron anti-neutrino mass by the KATRIN experiment set an upper bound of $m_{\bar{\nu}_e} < 0.8$ eV [7]. Even stronger limits arise from cosmological observations, which require the sum of the three neutrino masses to be below roughly 0.2 eV.

Oscillation experiments, while insensitive to the absolute mass scale, provide precise information on the neutrino mass splittings and mixing parameters. Global fits combining data from solar, atmospheric, reactor, and accelerator experiments are continuously improving the determination of the PMNS matrix parameters. Two possible scenarios for the ordering of the three neutrino masses are usually considered, as shown in Figure 2.4:

- **Normal Ordering (NO)**: $m_1 < m_2 < m_3$
- **Inverted Ordering (IO)**: $m_3 < m_1 < m_2$

A clear hierarchy among the neutrino mass splittings has been established, with $\Delta m^2_{21} \ll |\Delta m^2_{31}| \approx |\Delta m^2_{32}|$. This ordering was determined through the observation of matter effects, which modify neutrino oscillations as they propagate through dense media such as the Earth or the Sun.

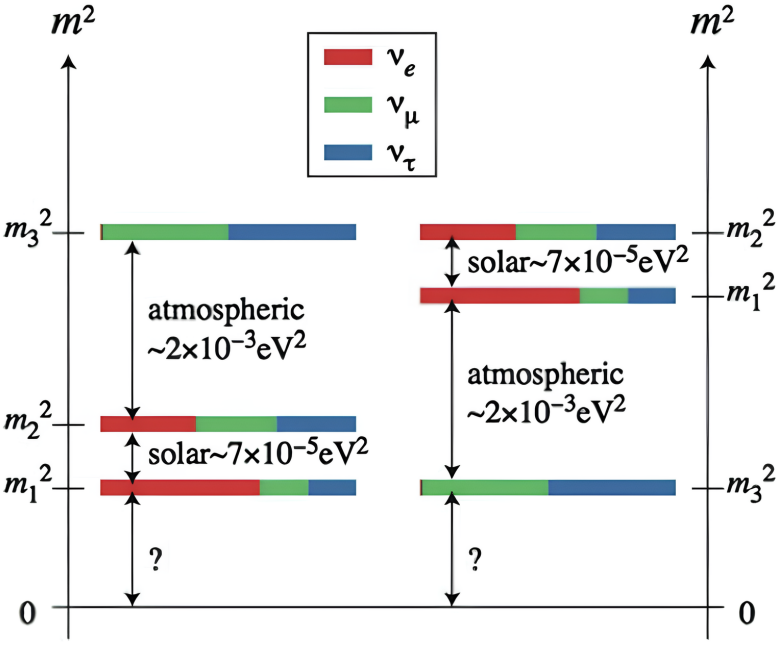

Figure 2.4: Schematic illustration of the two possible neutrino mass orderings: normal (left) and inverted (right). The measured solar and atmospheric mass splittings are indicated. The absolute neutrino mass scale remains unknown but is constrained to be below the eV level.

According to the most recent global analyses, as summarized by the Particle Data Group (PDG) [16], the PMNS parameters are currently determined with the following precision:

- **Solar mixing angle** (θ_{12}): governs solar neutrino oscillations. Best-fit $\sin^2\theta_{12} \simeq \mathbf{0.304 \pm 0.012}$ (NO and IO).

- **Reactor mixing angle** (θ_{13}): the smallest mixing angle, relevant for CP violation and mass ordering. Best-fit $\sin^2\theta_{13} \simeq \mathbf{0.02219 \pm 0.00062}$ (NO) and $\mathbf{0.02239 \pm 0.00063}$ (IO).

- **Atmospheric mixing angle** (θ_{23}): dominates atmospheric and long-baseline oscillations. Best-fit $\sin^2\theta_{23} \simeq \mathbf{0.570 \pm 0.017}$ (NO) and $\mathbf{0.575 \pm 0.016}$ (IO).

- **Solar mass splitting** (Δm^2_{21}): $\mathbf{7.39 \pm 0.20 \times 10^{-5}}$ eV^2 (both orderings).

- **Atmospheric mass splitting** (Δm^2_{31} or Δm^2_{32}): $\mathbf{2.528 \pm 0.028 \times 10^{-3}}$ eV^2 (NO), and $\mathbf{-2.511 \pm 0.028 \times 10^{-3}}$ eV^2 (IO). The negative sign in IO reflects the inverted hierarchy.

- **Dirac CP-violating phase** (δ_{CP}): current hints suggest $\mathbf{232^\circ \pm 35^\circ}$ (NO) and $\mathbf{277^\circ \pm 30^\circ}$ (IO). Values near 270° (or $\pm 90^\circ$) would correspond to maximal CP violation.

The determination of these parameters requires combining results from a wide range of experiments. Despite the significant progress achieved, the absolute neutrino mass scale, the true mass ordering, and the precise value of δ_{CP} remain open questions. Their resolution represents one of the major goals of current and future neutrino physics, with the potential to uncover new physics beyond the Standard Model.

2.3 Beyond the Standard Model

The landscape of neutrino physics has been profoundly shaped by the discovery of neutrino oscillations, unequivocally establishing that neutrinos possess mass and mix among their flavors. While the Standard Model (SM) of particle physics successfully describes fundamental interactions, the existence of massive neutrinos necessitates an extension beyond its original framework, as the SM postulates massless neutrinos. Intriguingly, for over two decades, several experimental results have hinted at phenomena that cannot be fully explained within the established three-neutrino oscillation paradigm, pointing towards what are commonly referred to as Short-Baseline Neutrino Anomalies. These anomalies suggest the presence of an additional, non-weakly interacting neutrino species, a sterile neutrino, which could drive new oscillation effects among the active flavors [22].

2.3.1 Short-Baseline Neutrino Anomalies

LSND The Liquid Scintillator Neutrino Detector (LSND) experiment, conducted at Los Alamos National Laboratory, was designed to search for $\bar{\nu}_\mu \to \bar{\nu}_e$ oscillations. LSND employed a stopped-pion source that produced an intense flux of $\bar{\nu}_\mu$ with energies up to 53 MeV. A liquid scintillator detector, located approximately 30 m from the source, was optimized to detect $\bar{\nu}_e$ events via inverse beta decay:

$$\bar{\nu}_e + p \to e^+ + n$$

The experimental signature relied on the prompt Čerenkov and scintillation light from the positron, followed by the delayed 2.2 MeV photon from neutron capture. The main backgrounds arose from conventional $\bar{\nu}_e$ production in the beam stop and from π^- decay-in-flight processes leading to $\bar{\nu}_\mu + p \to \mu^+ + n$ with subsequent μ^+ misidentification. After careful background subtraction, LSND observed an excess of 87.9 ± 22.4 (stat.) $\pm$ 6.0 (syst.) $\bar{\nu}_e$ events, corresponding to a 3.8σ deviation from expectations [8]. Interpreted in terms of neutrino oscillations, this result requires an additional mass-squared splitting of $\Delta m^2 \gtrsim O(0.1\ \text{eV}^2)$, pointing to physics beyond the three-flavor framework. This unexpected observation is commonly referred to as the LSND anomaly.

MiniBooNE To directly test the sterile neutrino interpretation of the LSND anomaly, the MiniBooNE experiment was constructed at Fermilab. MiniBooNE utilized the Booster Neutrino Beam (BNB), peaking at $E_\nu \sim 700$ MeV, with a detector placed 540 m downstream of the production target. This configuration probed the same $\frac{L}{E}$ range as LSND, making it sensitive to oscillations driven by mass-squared splittings of $O(1\ \text{eV}^2)$. The MiniBooNE detector, based on mineral oil Čerenkov technology, was optimized to observe Čerenkov rings from electrons and muons. After extensive running in both neutrino and antineutrino modes, MiniBooNE reported excesses of electron-like events corresponding to a 4.7σ deviation from expectations [9]. These excesses, especially concentrated in the low-energy region of the spectra, were found to be consistent with the LSND signal, thereby reinforcing the overall short-baseline anomaly.

2.3.2 The Sterile Neutrino Hypothesis

The collective body of short-baseline anomalies, including LSND and MiniBooNE, hinted at the existence of sterile neutrinos. A sterile neutrino is a hypothetical particle that, unlike active neutrinos, does not participate in any of the known fun-

damental forces of the Standard Model except gravity. Its existence must therefore be inferred indirectly through its mixing with active neutrinos, which could induce new oscillation effects.

The resolution of these anomalies through the sterile neutrino hypothesis typically involves extending the SM's particle content to include at least one sterile neutrino, often referred to as the 3+1 scenario (three active neutrinos plus one sterile neutrino). In this framework, neutrino oscillations arise from the fact that the flavor eigenstates ($\nu_e, \nu_\mu, \nu_\tau, \nu_s$) are non-trivial linear combinations of the mass eigenstates ($\nu_1, \nu_2, \nu_3, \nu_4$). The relationship between these states is described by an extended mixing matrix, which becomes a 4×4 unitary matrix in the 3+1 scenario, incorporating additional mixing angles and phases related to the sterile neutrino.

For short-baseline experiments, where the dominant mass-squared difference satisfies $\Delta m^2_{41} \gg |\Delta m^2_{31}|, \Delta m^2_{21}$, the oscillation probability can be well approximated by a two-flavor vacuum formula:

$$P_{\alpha\beta} = \delta_{\alpha\beta} - 4|U_{\alpha 4}|^2\left(\delta_{\alpha\beta} - |U_{\alpha 4}|^2\right)\sin^2\left(\frac{\Delta m^2_{41} L}{4E}\right), \tag{2.3}$$

where L is the source-detector distance, E the neutrino energy, and $U_{\alpha 4}$ the elements of the extended PMNS matrix describing the mixing between a flavor ν_α and the additional mass eigenstate ν_4.

In this framework, different short-baseline anomalies can be expressed in terms of effective mixing angles, depending on the oscillation channel considered:

- **Appearance channel $\nu_\mu \to \nu_e$**: this is the channel directly relevant to the LSND and MiniBooNE anomalies, which reported an excess of electron-like events in a predominantly muon neutrino (or antineutrino) beam. The probability is governed by

$$\sin^2 2\theta_{\mu e} \equiv 4|U_{\mu 4}|^2|U_{e4}|^2.$$

- **Electron neutrino disappearance $\nu_e \to \nu_e$**: reactor and gallium experiments observed fewer ν_e or $\bar{\nu}_e$ interactions than predicted, a deficit that can be parametrized as

$$\sin^2 2\theta_{ee} \equiv 4|U_{e4}|^2(1 - |U_{e4}|^2).$$

- **Muon neutrino disappearance $\nu_\mu \to \nu_\mu$**: unlike the other two cases, no

convincing anomaly has been seen here. The survival probability depends on

$$\sin^2 2\theta_{\mu\mu} \equiv 4|U_{\mu 4}|^2(1 - |U_{\mu 4}|^2).$$

An important consequence of this scheme is the intrinsic connection between different oscillation channels. In particular, if $\nu_\mu \rightarrow \nu_e$ appearance is observed, both $|U_{e4}|$ and $|U_{\mu 4}|$ must be non-zero. This automatically implies that a fraction of ν_e and ν_μ events should disappear in dedicated disappearance searches. The comparison between appearance and disappearance data therefore provides a powerful consistency check and plays a central role in constraining the sterile neutrino hypothesis [22].

2.3.3 Current Status and Future Outlook

Despite the initial appeal of the sterile neutrino hypothesis in explaining the short-baseline anomalies, the global experimental picture remains puzzling. In particular, combined analyses of ν_e appearance and disappearance data reveal strong inconsistencies: the regions of parameter space allowed by different channels often fail to overlap, with global fits showing a $\sim 4.7\sigma$ tension in the 3+1 framework. This suggests that a simple extension of the PMNS matrix with one sterile neutrino may not be sufficient to account for all observed anomalies.

The null results reported by MicroBooNE in its dedicated searches for an excess of ν_e interactions have further challenged the sterile neutrino interpretation of the MiniBooNE low-energy excess. These findings underscore the need for a new generation of experiments capable of addressing the short-baseline puzzle with improved sensitivity and reduced systematic uncertainties.

The Short-Baseline Neutrino (SBN) program at Fermilab has been designed precisely to provide a definitive test of the sterile neutrino hypothesis [22]. It consists of three detectors located along the Booster Neutrino Beam (BNB): the Short-Baseline Near Detector (SBND), MicroBooNE, and the ICARUS-T600 far detector. With this multi-detector configuration and the use of the same Liquid Argon Time Projection Chamber (LArTPC) technology in all detectors, SBN minimizes flux and cross-section uncertainties by enabling direct near–far data comparisons. Unlike LSND and MiniBooNE, which relied on single-detector setups and therefore on simulations to estimate the unoscillated spectrum, SBN will compare real data at different baselines, significantly reducing systematic errors.

SBN is optimized to probe both $\nu_\mu \rightarrow \nu_e$ appearance and ν_μ disappearance channels over the $\frac{L}{E}$ range relevant to the LSND and MiniBooNE anomalies. The near

detector (SBND) plays a critical role in measuring the unoscillated flux and neutrino interaction rates, while the far detector (ICARUS-T600) searches for oscillated spectra. This configuration provides the necessary sensitivity to confirm or exclude the parameter regions suggested by previous anomalies.

Looking ahead, the knowledge and technological developments from SBN will directly contribute to the Deep Underground Neutrino Experiment (DUNE), a next-generation long-baseline neutrino experiment that will also employ large LArTPC detectors. DUNE aims to address key open questions in neutrino physics, including the determination of the neutrino mass ordering and the measurement of CP violation in the lepton sector, with profound implications for the origin of the matter–antimatter asymmetry in the Universe.

Complementary to this approach, the Jiangmen Underground Neutrino Observatory (JUNO) in China will use a different detection technology, namely a massive liquid scintillator detector with unprecedented energy resolution. By observing reactor antineutrinos at a medium baseline of about 53 km, JUNO is designed to determine the neutrino mass hierarchy and provide high-precision measurements of oscillation parameters. Together, DUNE and JUNO will offer complementary perspectives: while DUNE focuses on accelerator-based long-baseline oscillations with sensitivity to CP violation, JUNO will constrain oscillation parameters and mass ordering from reactor neutrinos, thereby reinforcing the global neutrino physics program.

3 The Short Baseline Program

The motivation for SBN originates from a series of anomalous results in short-baseline neutrino experiments, most notably those obtained by LSND and MiniBooNE, as discussed in Section 2.3. These anomalies suggest the possible existence of sterile neutrino states, which, if they exist, would not interact through the weak interaction and would therefore remain invisible to direct detection. However, their mixing with the three active neutrino flavors could generate new oscillation phenomena. The SBN program has been specifically designed to provide a definitive test of these anomalies by combining multiple detectors located along the same neutrino beamline. If sterile neutrinos were to be discovered, their existence would represent a major breakthrough in particle physics, revealing a new and unexpected form of matter and opening up entirely new lines of experimental inquiry. On the other hand, a null result would close a long-standing puzzle in the field, consolidating the standard three-flavor oscillation framework. Moreover, sterile neutrinos, in some scenarios, could significantly affect the measurement of CP violation in DUNE and influence searches for neutrinoless double beta decay, which further underlines the importance of a precise and systematic exploration of this possibility at SBN [26].

3.1 The Experimental Layout

The experimental configuration of SBN, illustrated in Figure 3.1 is based on three large LArTPC detectors located along the Booster Neutrino Beam (BNB) at Fermilab. The near detector, SBND (Short-Baseline Near Detector), is positioned only 110 m from the neutrino production target, allowing a precise characterization of the neutrino beam before oscillations can develop. The MicroBooNE detector, with an active mass of 89 tons, has been operating at a distance of 470 m since 2015. The far detector, ICARUS-T600, with its 476-ton active volume, is located 600 m downstream of the target and has been refurbished and upgraded for optimal performance. The use of multiple detectors at different baselines, sharing the same technology and exposed to the same beam, is the defining feature of SBN. This configuration ensures a direct comparison of neutrino event spectra at different distances, which

strongly suppresses systematic uncertainties and provides world-leading sensitivity to oscillation signals.

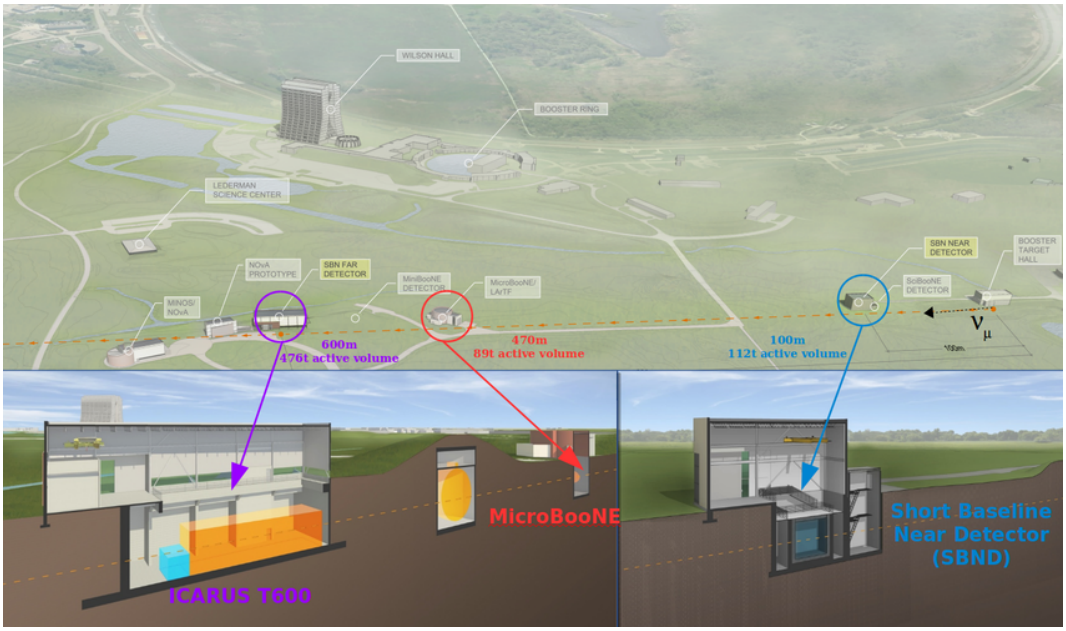

Figure 3.1: An aerial view of the SBN experimental area at Fermilab. To the right is the neutrino beam target area where 8 GeV protons from the Booster accelerator impinge a beryllium target. The beam is focused along the orange dashed line (approximately 7 m below ground) traveling toward the left (north).The near detector, MicroBooNE, and far detector building locations are indicated.

3.1.1 The Booster Neutrino Beam

A crucial element of the SBN program is the Booster Neutrino Beam (BNB), produced at Fermilab and directed toward the three LArTPC detectors. A schematic view of a conventional neutrino beamline is shown in Figure 3.2.

The production process begins in the Fermilab linear accelerator (Linac), where negative hydrogen ions are accelerated up to 400 MeV kinetic energy. After electron stripping, the resulting protons are injected into the 474 m circumference Booster synchrotron ring, where they are accelerated to 8 GeV. Electron stripping is a process in which the electrons bound to negative hydrogen ions (H^-) are removed, leaving bare protons (H^+) ready for acceleration. This technique allows for efficient injection into circular accelerators without the need for complex kicker magnets. The Booster can store 84 bunches of protons per cycle, of which 81 are typically

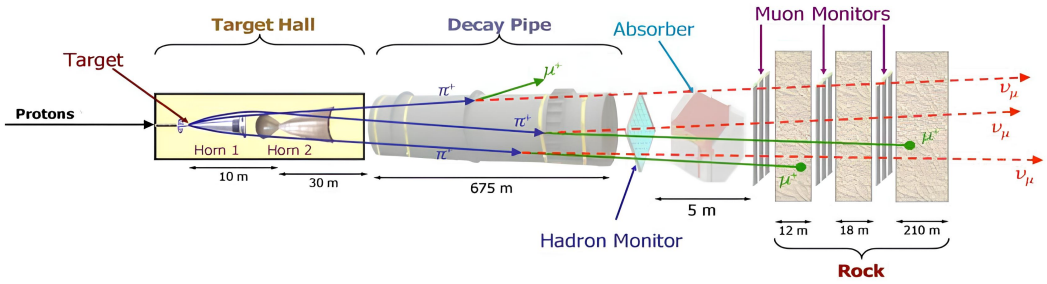

Figure 3.2: Schematic view of a conventional neutrino beamline. A high-energy proton beam strikes a target, producing secondary hadrons such as pions and kaons. Magnetic focusing horns select and guide charged mesons of a chosen sign into the decay pipe. As these mesons travel through the decay pipe, they decay primarily into muons and muon neutrinos. At the downstream end, an absorber stops the remaining hadrons and muons, while neutrinos continue toward the detectors.

filled. Each bunch contains about 6.2×10^{10} protons, spaced 19 ns apart and about 2 ns wide. The extraction of all 81 bunches corresponds to a single "spill," which delivers approximately 5×10^{12} protons within 1.6 μs. Spills can be produced at a maximum rate of 5 Hz. The whole process is represented in Figure 3.3. Additional information on the accelerator system and techniques can be found in [25].

The protons are directed onto a beryllium target of 0.51 interaction lengths in radius. Beryllium is chosen for its favorable thermal properties, which allow air cooling and reduced residual radiation. Interactions between the protons and the target produce secondary hadrons, mainly charged pions and kaons. These hadrons are focused by a pulsed aluminum magnetic horn operated at 174 kA, synchronized with the proton delivery in pulses of 143 μs. The polarity of the horn can be reversed to select either positively charged hadrons (neutrino mode) or negatively charged hadrons (antineutrino mode).

The focused hadrons are directed into a 50 m-long cylindrical decay tunnel filled with air, where they predominantly decay via the processes summarized in Table 3.1.

Neutrino mode	Antineutrino mode
$\pi^+ \to \mu^+ + \nu_\mu$	$\pi^- \to \mu^- + \bar{\nu}_\mu$
$K^+ \to \mu^+ + \nu_\mu$	$K^- \to \mu^- + \bar{\nu}_\mu$

Table 3.1: Main hadron decay channels producing neutrinos and antineutrinos.

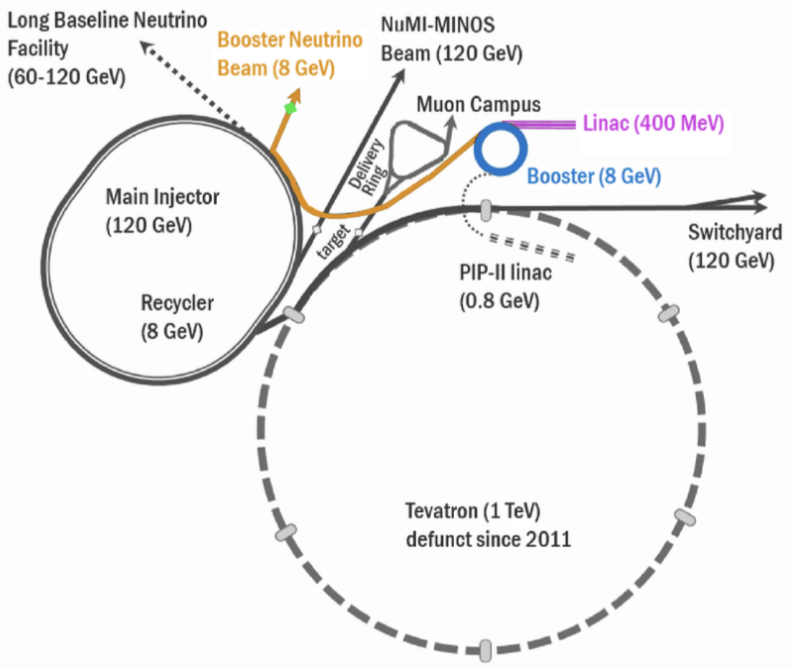

Figure 3.3: The different components of the BNB production system are highlighted in color. Protons exiting the 400 MeV Linac (purple) are accelerated to kinetic energy of 8 GeV in the Booster synchrotron (blue). These protons are then directed at a beryllium target (green) to produce secondary hadrons (orange), which subsequently decay, resulting in the creation of the neutrino beam.

At the end of the decay region, a steel and concrete beam stop absorbs the remaining hadrons and muons, while the produced neutrinos continue toward the detectors. Muon monitors placed downstream provide an indirect measurement of the neutrino flux. The whole process is schematically represented in Figure 3.2.

The BNB has been in operation for more than fifteen years and was originally employed by the MiniBooNE experiment, which performed detailed measurements and simulations of the beam spectrum and composition. In neutrino mode, the flux is overwhelmingly dominated by muon neutrinos, peaking at $E_\nu \sim 0.7$ GeV with a broad distribution from 0 to 3 GeV. The purity of the ν_μ component is about 95%, with $\sim 6\%$ $\bar{\nu}_\mu$ contamination and $\sim 0.5\%$ $\nu_e + \bar{\nu}_e$ contamination (see Figure 3.4).

Although the decay pipe length is optimized to suppress secondary muon decays, additional backgrounds remain. In particular, ν_e contamination arises from muon decays ($\mu^+ \longrightarrow e^+ + \nu_e + \bar{\nu}_\mu$) occurring before muons are absorbed in the beam stop, from π^- that escape horn focusing, and from rare kaon decays. These effects have

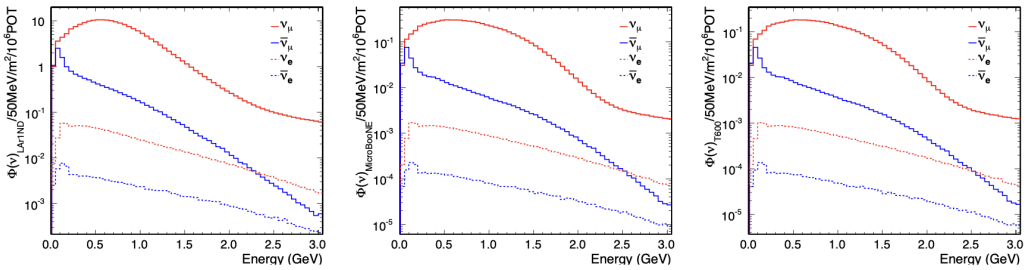

Figure 3.4: The ν_μ, $\bar{\nu}_\mu$, ν_e, and $\bar{\nu}_e$ components of the flux distributions for each SBN experiment are shown. On the left is SBND, in the middle is MicroBooNE, and on the right is ICARUS. The solid red and blue lines represent ν_μ and $\bar{\nu}_\mu$ respectively, while the dashed lines correspond to ν_e and $\bar{\nu}_e$.

been extensively studied, and thanks to MiniBooNE's analyses and external hadron production data, the BNB flux is now well constrained [22]. The well-characterized nature of the BNB, combined with the multi-detector configuration of SBN, provides the precision needed to test the sterile neutrino hypothesis.

3.1.2 Liquid Argon Time Projection Chambers

The three detectors that form the SBN program are based on the same LArTPC technology but optimized for their specific roles. SBND, the near detector, is a 112-ton active mass TPC designed to provide the most precise characterization of the BNB flux. MicroBooNE, which has been operating since 2015, combines neutrino cross-section measurements with the investigation of the MiniBooNE low-energy excess. ICARUS-T600, the largest of the three detectors, was previously operated at LNGS in Italy and has been upgraded for its role at Fermilab. Its very large active mass provides the statistical power required to explore oscillation signals with high significance. Together, SBND, MicroBooNE, and ICARUS provide an unparalleled capability for precision oscillation studies at the short-baseline scale.

LArTPCs represent a cutting-edge detector technology that has revolutionized neutrino physics measurements, offering unprecedented precision. The concept of the LArTPC was first proposed in 1977 by Carlo Rubbia as a new design for neutrino detectors [24]. This innovative approach is an evolution of the Time Projection Chamber (TPC) concept developed by Nygren, and the liquid Argon ionization chamber detectors designed by Willis and Radeka in the late 1960s and early 1970s.

Liquid Argon (LAr) serves as an ideal medium for neutrino detectors due to several key properties:

- *High Density:* at 1.41 g/cm^3, it is significantly denser than in its gaseous phase, making it highly effective for detecting elusive particles like neutrinos. This density also provides a large number of interaction targets; for instance, Argon-40 (which makes up 99.6% of naturally occurring Argon) contains approximately 2.1×10^{22} atoms per cm^3, corresponding to 3.8×10^{23} protons and 4.6×10^{23} neutrons.

- *Chemical Inertness:* LAr is a noble gas and is chemically inert, allowing ionization charge to drift over several meters without significant loss.

- *Excellent Scintillator:* it is an excellent scintillator, providing a prompt light signal crucial for precise interaction timing.

- *Transparency to its own Scintillation Light:* LAr is transparent to its own scintillation light, further aiding in signal detection and reconstruction.

- *Ease of Liquefaction and Purification:* Argon is relatively easy and economical to liquefy and purify, a vital aspect for large-scale experiments. It liquefies at approximately 87 K, which can be achieved on a large scale using readily available liquid nitrogen.

These characteristics enable the construction of LArTPC modules as massive as multiple kilotons, such as those planned for the Deep Underground Neutrino Experiment (DUNE) [3].

Other important properties of Argon, when held in a 500 V/cm electric field and at 87 K, are summarized in Table 3.2.

Property	Value
Electron drift velocity	1.6 mm/μs
Critical energy $e^{\pm}$	32.8 MeV
Critical energy $\mu^{\pm}$	485 GeV
Molière radius	9.04 cm
Radiation length	14.0 cm
Nuclear interaction length	85.7 cm
Minimum specific loss	2.12 MeV/cm

Table 3.2: Summary table of argon properties (for an electric field of 550 V/cm).

Operational Principle The basic operational principle of a LArTPC involves detecting the byproducts of neutrino interactions. When neutrinos interact with Argon atoms, they can produce secondary charged particles. These charged particles, in turn, ionize and excite the liquid Argon. The ionization electrons are then drifted by an applied electric field towards multiple planes of sense wires, typically located at the detector's anode. Simultaneously, the interacting particles produce scintillation light, which is detected by specialized photon detectors, such as photomultiplier tubes (PMTs) or silicon photomultipliers (SiPMs). This combination of charge and light signals allows for high-precision event reconstruction, excellent particle identification, and fine-sampling calorimetry. A scheme of a typical LArTPC is illustrated in Figure 3.5

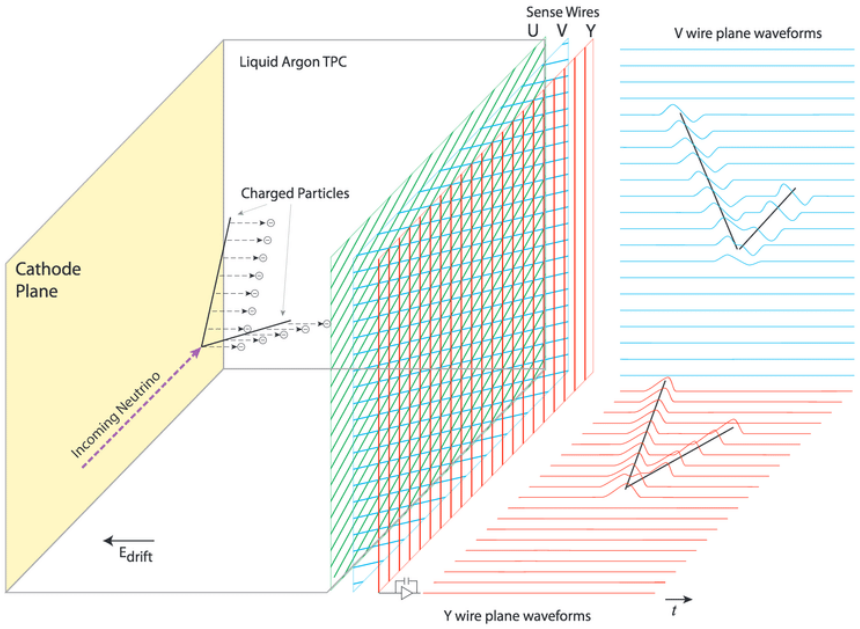

Figure 3.5: A schematic diagram of a Liquid Argon Time Projection Chamber. An incoming neutrino interacts with the liquid Argon, producing charged particles that ionize the Argon atoms. A strong electric field E_{drift} drifts the electrons toward the wire planes (U, V, and Y). The timing of the signal provides the drift distance (and thus the X coordinate), while the U, V, and Y planes provide a 2D projection that can be used to reconstruct the full 3D trajectory of the particles.

Neutrino-Nucleus interactions in Argon Studies of neutrino-nucleus interactions are essential for investigating the fundamental properties of neutrinos through the analysis of their interaction products. At neutrino energies below approximately 1 GeV, the dominant processes are Charged-Current Quasi-Elastic (CCQE) scattering and Neutral-Current Elastic (NCE) scattering, as shown in Figure 3.6. These interactions are typically described assuming that the neutrino scatters off a single nucleon. The most widely used formalism is the Llewellyn-Smith model, which incorporates the nuclear charge distribution through the axial mass and form factors.

For heavier nuclei, however, the single-nucleon approximation becomes insufficient. In such cases, multi nucleon effects must also be considered, such as those arising from Meson Exchange Currents (MEC), where the neutrino couples to two nucleons simultaneously, as illustrated in Figure 3.7.

As the neutrino transfers larger amounts of energy to the nucleus, it may excite nucleons into baryonic resonances, which promptly decay into mesons and nucleons. A well-known example is the production and decay of the Δ^{++} resonance (Figure 3.8). These processes are commonly described using the Berger-Sehgal model, where the neutrino interacts with a nucleon rather than a parton, since partons cannot fragment in this energy regime.

At even higher neutrino energies, the interaction can take place directly with the partonic constituents of the nucleon. This regime, known as Deep Inelastic Scattering (DIS), leads to the fragmentation of the struck parton and the subsequent production of a hadronic shower (Figure 3.9). DIS is typically modeled using the Bodek-Yang approach for structure functions, combined with hadronization models such as the Andreopoulos-Gallagher-Kehayias-Yang (AGKY) framework.

For a comprehensive overview of neutrino-nucleus interactions, see [1] and [13].

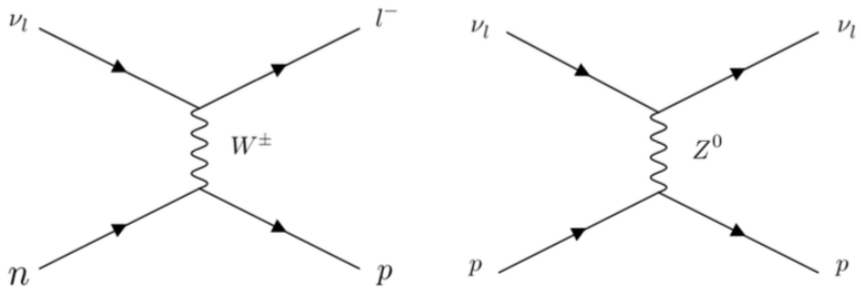

Figure 3.6: Feynman diagrams illustrating Charged-Current Quasi-Elastic (CCQE) scattering (left) and Neutral-Current Elastic (NCE) scattering (right).

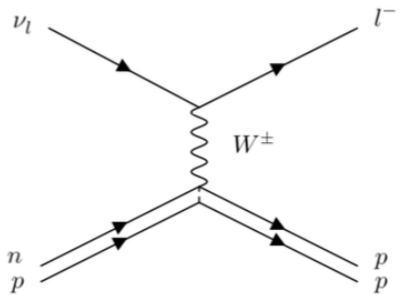

Figure 3.7: Example of a neutrino interaction with two nucleons via Meson Exchange Currents (MEC).

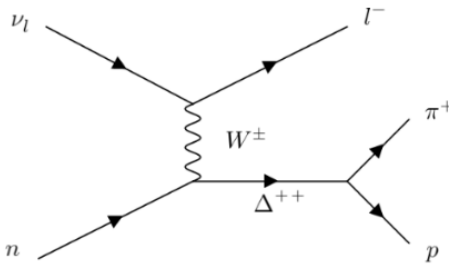

Figure 3.8: Resonant pion production through excitation and decay of the Δ^{++} resonance.

Particle Interactions in Liquid Argon In LArTPC detectors, particles traversing the liquid Argon volume manifest as either tracks or electromagnetic showers, depending on their behavior. Neutral particles, like neutrinos, are detected indirectly through the charged particles they produce upon interaction with the Argon.

Charged particles such as muons, pions, and protons create distinct tracks of ionization in the liquid Argon. The average amount of energy deposited per unit length, known as $\frac{dE}{dx}$, along these tracks is modeled by the Bethe-Bloch equation, which trend is shown in Figure 3.10 [16].

For minimally ionizing particles (MIPs) in liquid Argon, the average $\frac{dE}{dx}$ is approximately 2.12 MeV/cm (see Table 3.2). The energy loss depends on both the particle type and the detector medium. In the context of the BNB, muons and pions are predominantly produced in the minimally ionizing region, while protons often fall into the steeply rising part of the curve, meaning they are more highly ionizing.

Electrons and photons typically produce electromagnetic showers in liquid Argon. An electron initiates a shower through bremsstrahlung radiation, generating

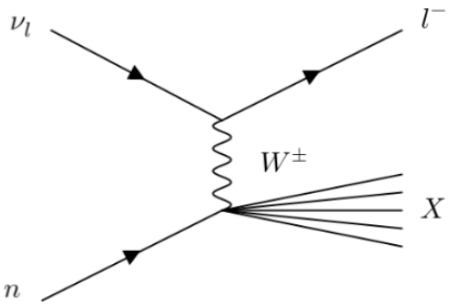

Figure 3.9: Deep Inelastic Scattering (DIS) where the neutrino interacts with a parton, leading to a hadronic shower.

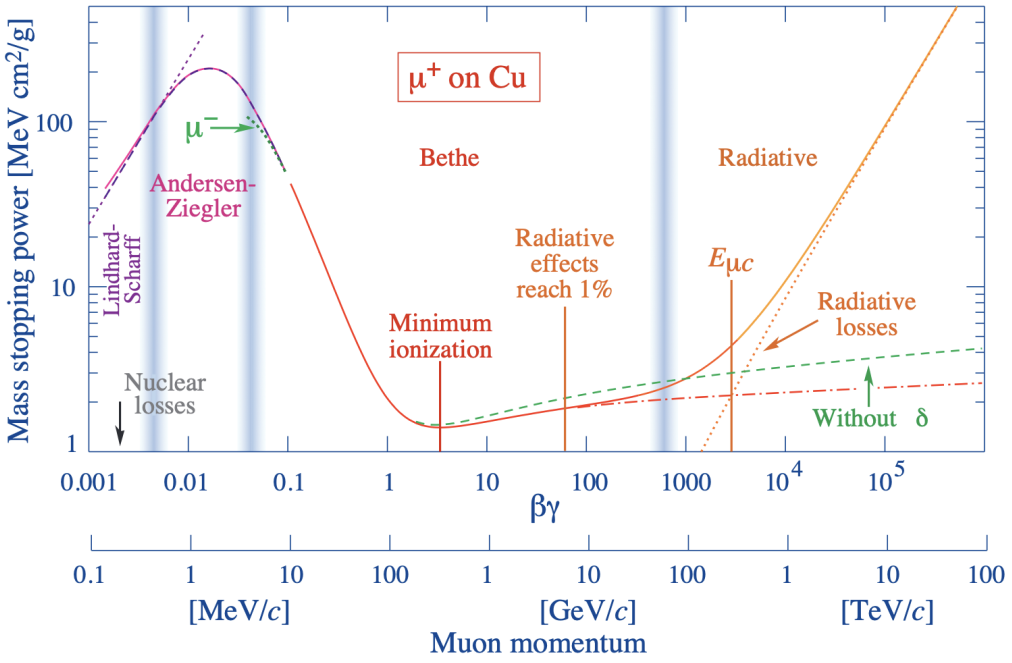

Figure 3.10: Mass stopping power (dE/ρ dx) for positive muons in copper as a function of $\beta\gamma = p/Mc$ over nine orders of magnitude in momentum.Solid curves indicate the total stopping power. Vertical bands indicate boundaries between different approximations.

a high-energy photon. This photon then undergoes pair production, creating an electron-positron pair. These newly created particles can, in turn, generate more bremsstrahlung photons and electron-positron pairs, leading to an electromagnetic cascade. The critical energy, below which ionization losses dominate over radiative losses, is 32.8 MeV for electrons in Argon. The radiation length for Argon is 14.0

cm, indicating the average distance over which an electron loses all but $1/e$ of its energy by bremsstrahlung (see Table 3.2).

LArTPC technology offers an advantage in distinguishing between photon-generated and electron-generated electromagnetic showers, a capability that was not reliably possible in earlier liquid scintillator detectors like MiniBooNE. This electron-gamma separation is implemented through calorimetric analysis.

Ionization Signal The ionization signal is a primary source of information in LArTPCs, providing calorimetric and spatial details of particle interactions.

- **Production:** when a charged particle traverses liquid Argon, it transfers energy to the Argon atoms, leading to their ionization and the creation of electron-ion pairs. The average energy expended per ion pair in liquid Argon is approximately 23.6 eV, assuming an electric field of 500 V/cm. However, some of these electron-ion pairs can recombine due to the electric field's influence. While the noble gas nature of Argon disfavors recombination, it is an observed process. The amount of recombination is dependent on the electric field strength, with stronger fields reducing recombination and thus increasing the collected charge.

- **Propagation:** once produced, the ionization electrons drift towards the anode due to the applied electric field. The drift velocity of these electrons is dependent on the electric field strength and on the medium. At a typical LArTPC electric field of 500 V/cm, the drift velocity is approximately 1.6 mm/μs. This means that in large-scale LArTPCs with drift distances of several meters, electrons can take milliseconds to reach the sense wires.

  The purity of the liquid Argon is crucial for effective electron drift. Electronegative impurities like oxygen, water, and carbon dioxide can attach to ionization electrons, suppressing the signal before it reaches the sense-wire planes. The effect of these impurities is often characterized by an electron lifetime, which modern LArTPCs, through sophisticated purification systems, have extended to as high as 100 ms, corresponding to contamination levels less than 5 ppt oxygen equivalent.

  During propagation, diffusion of the ionization electrons also occurs, leading to a spreading of the charge signal. This spreading can affect spatial resolution but typically has a minimal impact on large-scale LArTPCs.

- **Detection:** the drifting ionization electrons are detected by sense wires arranged in multiple planes at the anode of the detector. These wire planes typically have different orientations (e.g., induction planes at ±60° and a collection plane at 0° or 90° relative to the beam direction) to allow for three-dimensional imaging of particle tracks. The amount of charge induced or collected on these wires is directly correlated with the energy deposited in the detector, enabling calorimetry once recombination and propagation effects are accounted for. The wire plane configuration in a LArTPC allows for the production of neutrino event images comparable to those from bubble chamber experiments.

Scintillation Light Signal In addition to ionization, liquid Argon produces a prompt scintillation light signal, which is vital for precise event timing and for distinguishing different particle interactions.

- **Production:** liquid Argon is an excellent scintillator. Its scintillation light originates from the de-excitation of Argon dimer states (Ar_2^*). These excimer states are formed when excited Argon atoms (Ar^*) combine with ground-state Argon atoms. The de-excitation process results in the emission of Vacuum Ultra-Violet (VUV) photons with a narrow spectrum peaking at approximately 128 nm.

  The scintillation light signal is characterized by two distinct time components:

  - *Fast (or prompt) component* with lifetimes of approximately 6-7 ns.
  - *Slow (or late) component* with lifetimes of approximately 1.3-1.6 µs.

  The energy required to produce a scintillation photon is approximately 19.5 eV at 500 V/cm. For a Minimally Ionizing Particle (MIP), the light yield is about 4×10^4 photons/MeV. The ratio of the fast to slow components depends on the ionizing radiation, allowing for discrimination of different particles.

- **Propagation:** the propagation of scintillation light in liquid Argon is influenced by several factors:

  - *Transparency:* liquid Argon is transparent to its own VUV scintillation light.
  - *Rayleigh Scattering:* photons can undergo Rayleigh scattering, which depends on the wavelength of light. The Rayleigh scattering length (λ_{RS}) in liquid Argon has been measured to be around 100 cm.

  - *Group Velocity:* the group velocity of VUV photons emitted at 128 nm is approximately two times slower than that of visible light in Argon due to its high refractive index at VUV wavelengths.
  - *Absorption by Contaminants:* even at part-per-million levels, electronegative contaminants like nitrogen (N_2) and oxygen (O_2) can significantly absorb Argon scintillation light, reducing the signal. For nitrogen, an absorption length of 20 m corresponds to about 3 ppm of nitrogen equivalent.

- **Detection:** detecting scintillation light in LArTPCs requires specialized photon detectors (PDs) capable of operating at cryogenic temperatures (~ 87 K).
  - *PhotoMultiplier Tubes (PMTs):* historically, PMTs have been the primary photon-detector technology, with quantum efficiencies (QE) up to 30%. However, their size can make efficient placement challenging, leading to non-instrumented regions.
  - *Silicon PhotoMultipliers (SiPMs):* current and future detectors are increasingly adopting SiPMs due to their smaller size, lower power consumption, excellent noise performance at cryogenic temperatures, and high QEs (up to 40%).
  - *Light Traps:* devices like ARAPUCA and X-ARAPUCA are used to enhance light collection efficiency by trapping scintillation photons within highly reflective boxes, which are then detected by SiPMs (for the working principle see Figure 3.11). The X-ARAPUCA, an improved version, utilizes total internal reflection in an acrylic sheet to guide photons to SiPMs, further enhancing efficiency.

  Since the 128 nm VUV scintillation photons are strongly absorbed by the quartz windows of PMTs and SiPMs, a wavelength-shifting (WLS) compound, most commonly Tetraphenyl Butadiene (TPB), is applied to the detector surfaces or the PDs themselves. TPB converts the VUV light into visible wavelengths, peaking around 430 nm, to which the PDs are sensitive. This process introduces a characteristic decay time, as long as several microseconds, from the TPB re-emission.

  The scintillation light signal provides the most precise interaction timing information available in LArTPC detectors, with electronics and data acquisition chains typically designed for resolutions between 1-2 ns and 100 ns.

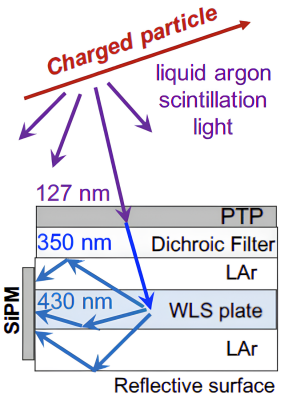

Figure 3.11: Working principle of an X-ARAPUCA cell. A charged particle passing through LAr produces scintillation light at a wavelength of 127 nm. A wavelength-shifting material is often applied to the cathode plane or internal surfaces to shift the ultraviolet (UV) scintillation light to a visible wavelength (e.g., 350 nm). A dichroic filter then transmits this light while reflecting unwanted wavelengths. The light is then guided into a wavelength-shifting (WLS) plate, which further shifts the light to a more suitable wavelength for the detector (e.g., 430 nm), and channels it toward the SiPM. The SiPM registers the number of photons, providing a fast signal that can be used for event timing and triggering.

3.1.3 MicroBooNE

Motivated by these persistent anomalies, in particular the MiniBooNE low-energy excess (see Subsection 2.3), the MicroBooNE experiment was launched as part of the Short-Baseline Neutrino (SBN) program at Fermilab. MicroBooNE employs the Liquid Argon Time Projection Chamber (LArTPC, see Subsection 3.1.2) technology, providing detailed 3D reconstruction and excellent particle identification. A crucial advantage of LArTPCs is their capability to distinguish between electromagnetic showers initiated by electrons and those initiated by photons, which represented a major background in MiniBooNE. While electrons produce a single minimum-ionizing track at the start of the shower, photons typically travel a short distance before converting into an e^+e^- pair, yielding a two-track signature. Exploiting this ability, MicroBooNE performed dedicated analyses of the MiniBooNE parameter space. Recent results from MicroBooNE disfavor the most popular sterile neutrino interpretations of the MiniBooNE excess, finding no significant evidence for an excess of ν_e events. Furthermore, no signal consistent with light sterile neutrino oscillations has been observed.

3.1.4 ICARUS

The Imaging Cosmic And Rare Underground Signals (ICARUS) program, initiated in 1985, has played a pioneering role in the development of the Liquid Argon Time Projection Chamber (LArTPC) technology for neutrino physics. Following the successful construction of prototype detectors with active masses of 3 and 14 tons, the program led to the design and realization of the ICARUS-T600 detector. Assembled and operated at the Gran Sasso National Laboratory (LNGS) between 2010 and 2013, the T600 represented the first large-scale LArTPC ever built. During its operation, the detector successfully demonstrated the feasibility of running a large underground liquid-Argon detector, measured the neutrino velocity, and carried out searches for neutrino oscillations using the CNGS neutrino beam [4].

The T600 consists of two identical adjacent modules (T300), housed in a common cryostat, with a total active LAr mass of 476 tons. Each T300 module hosts two TPCs separated by a vertical cathode. The active volume of each half-module measures 18.0 m $\times$ 3.2 m $\times$ 3.0 m (length $\times$ height $\times$ width). The maximum drift length, defined as the distance between the cathode and the anode wire planes, is 1.5 m, corresponding to a maximum drift time of approximately 950 μs for the nominal electric field of 500 V/cm. The cathodes are constructed from stainless-steel frames supporting punched panels and biased at -75 kV. Field-shaping electrodes connected through a resistor chain ensure the uniformity of the electric field across the drift volume.

Each drift volume is instrumented with three vertical parallel anode wire planes, spaced 3 mm apart, for a total of 53,248 wires made of AISI 304V stainless steel with a diameter of 150 μm. The wires are oriented at 0°, +60°, and $-60°$ relative to the horizontal, enabling 3D event reconstruction by combining the different views. Signals are processed through custom-designed front-end electronics: decoupling and bias boards provide voltage and test-signal distribution for groups of wires, while digitization and amplification are performed by motherboards housed in dedicated crates mounted on the external side of the cryostat feedthroughs.

A key difference between SBND and ICARUS is that SBND performs amplification and digitization in the cold, which reduces electronic noise compared to performing these operations in the warm.

In addition to the charge readout, each drift volume is equipped with a light detection system consisting of 90 eight-inch Hamamatsu R5912-MOD photomultiplier tubes (PMTs), arranged in a grid behind the anode wire planes. The PMTs are coated with Tetra-Phenyl Butadiene (TPB), which shifts the 128 nm VUV scintillation light produced in liquid Argon into the visible spectrum, where the tubes are

most sensitive. Each PMT is enclosed in a grounded stainless-steel cage to prevent electrical interference with the TPC wire planes [5].

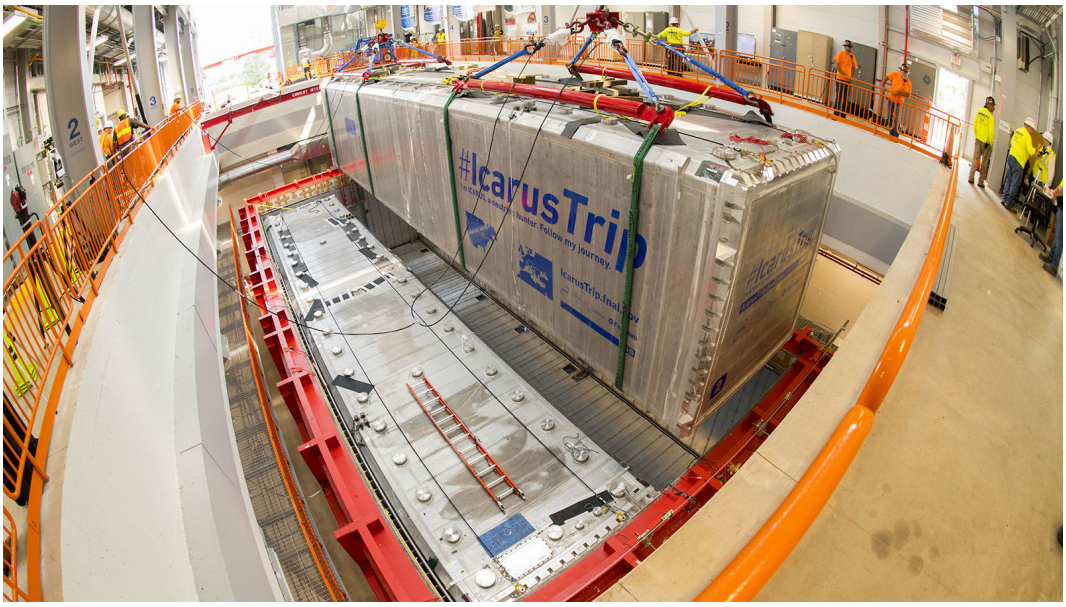

Figure 3.12: The ICARUS-T600 detector being lowered into position inside the SBN Far Detector hall at Fermilab in August 2018.

In 2014, the T600 was transported to CERN, where it underwent an extensive refurbishment campaign. The upgrades included:

- the installation of new high-performance TPC readout electronics hosted in compact crates mounted directly on the signal flanges,
- the implementation of a new scintillation light detection system with 360 eight-inch PMTs,
- the construction of new cold aluminum vessels, and
- a complete overhaul of the cryogenic and Argon purification systems.

Following refurbishment, the two modules were installed in their new vessels at CERN and subsequently transported to Fermilab in July 2017. Final installation in the SBN Far Detector building was completed in August 2018 (Figure 3.12). As with the near detector, ICARUS is surrounded by a segmented Cosmic Ray Tagger (CRT) system, composed of plastic scintillator panels read out by SiPMs, in order to identify and suppress cosmic-ray-induced backgrounds. The commissioning of

ICARUS on the Booster Neutrino Beam (BNB) began in 2021, marking the start of its physics program within the SBN experiment [6].

4 Short Baseline Near Detector

The Fermilab Short Baseline Neutrino (SBN) program includes the construction of the Short-Baseline Near Detector (SBND) in a dedicated new enclosure (see Figure 4.1). Leveraging the advanced design work performed for the Long-Baseline Neutrino Experiment (LBNE) and the recent experience from the MicroBooNE detector construction, SBND was developed with the potential for rapid progress and high performance.

As the near detector in the SBN program, SBND's close proximity to the neutrino source enables high-precision measurements of the unoscillated BNB neutrino flux and neutrino-argon cross-sections, which are essential for reducing systematic uncertainties in oscillation searches at $\Delta m^2 \sim 1$ eV^2. Technologically, SBND follows the MicroBooNE design as an engineering prototype for future LArTPC detectors, contributing to the development of large-scale detectors for long-baseline CP-violation studies, including DUNE.

The primary scientific goals of SBND include searches for eV-scale sterile neutrinos, investigations of physics beyond the Standard Model, and precise characterization of neutrino-argon interactions. The construction of the detector was completed by the end of 2023, with commissioning successfully concluded in July 2024 and has been taking neutrino data since December 2024 [22].

SBND consists of three sub-detectors: a Liquid Argon Time Projection Chamber, a photon detection system, and the Cosmic Ray Tagger (as illustrated in Figure 4.2).

4.1 SBND Time Projection Chamber

The core of the SBND detector is its sophisticated LArTPC, specifically engineered for high-resolution tracking and calorimetry of neutrino interactions. The active volume of the TPC measures 5.0 m in length (along the beam direction), 4.0 m in width, and 4.0 m in height, containing 112 metric tons of active liquid argon. This volume is geometrically divided into two distinct drift regions, each 2 meters long, separated by a central cathode. The electrons, liberated by ionizing particles, drift under the influence of an electric field perpendicular to the neutrino beam direction (see Figure 4.3).

Each drift volume is equipped with a pair of interconnected anode plane as-

Figure 4.1: Detector hall for SBND, located 110 meter downstream of the Booster Neutrino Beam (BNB) Target on Fermilab's Neutrino Campus.

semblies (APAs), which are responsible for reading out the ionization charge. An APA, measuring approximately 4.0 m by 2.5 m, supports three planes of 150 μm copper-beryllium wires, with a 3 mm wire pitch and 3 mm spacing between the planes. These wire planes include a vertical collection plane (Y) and two induction planes (U and V) oriented at $\pm 60^{\circ}$ relative to the vertical (see Figure 4.4). Signals from these wires are processed by cold electronics immersed in the liquid argon, an innovative design that shares its first-stage components with the DUNE experiment [18].

The central cathode plane assembly (CPA) is a robust, electropolished stainless steel structure that is biased at -100 kV, generating a uniform electric field of 500 V/cm throughout the drift volumes. To maintain the uniformity of this field, a field cage, constructed from roll-formed aluminum profiles, surrounds the liquid volume, mirroring the design used for DUNE. The entire TPC system is housed within a stainless steel membrane cryostat, which is suspended from the cryostat roof. This cryostat design is itself a prototype for the DUNE experiment, highlighting

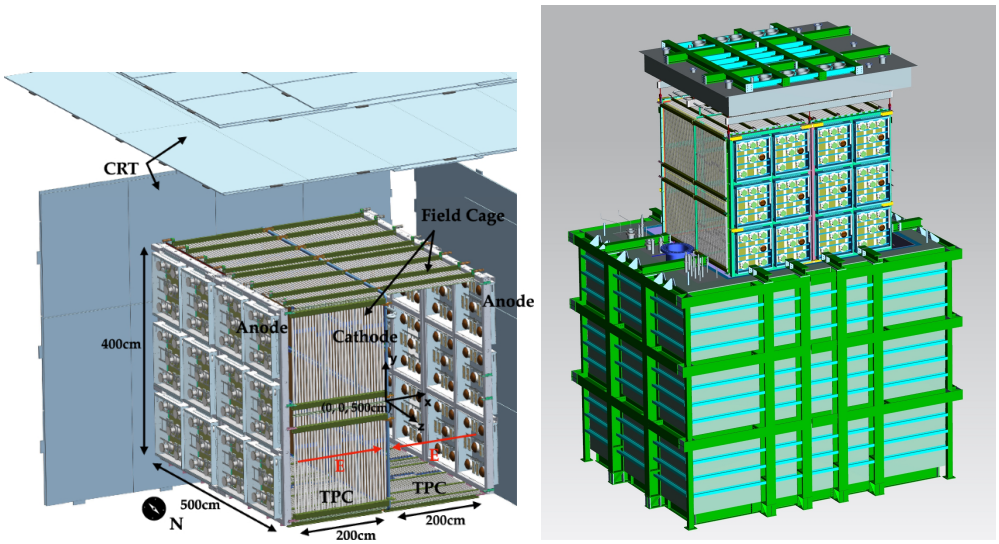

Figure 4.2: These images show the core components of the SBND detector. At its center is the TPC surrounded by a field cage, cathode, and anode planes to create a uniform electric field. The Photo Detection System, located behind the anode planes. The entire apparatus is enclosed by the Cosmic Ray Tagger, a system that identifies and tags cosmic rays.

SBND's role in advancing LArTPC technology [20]. Figure 4.5 shows the detector and cryostat lid assembly being lowered into the SBND membrane cryostat.

4.2 SBND Photo Detection System

The SBND incorporates a sophisticated composite photon detection system (PDS) designed to both enhance light collection and facilitate research and development in liquid argon scintillation detection. The primary PDS consists of an array of 120 8-inch Hamamatsu R5912-mod photomultiplier tubes (PMTs). 80% of these PMTs are coated with Tetraphenyl Butadiene (TPB), a wavelength-shifting compound that efficiently converts the 128 nm vacuum ultraviolet (VUV) scintillation light produced in liquid argon into visible light, peaking around 430–450 nm.

The detection of this prompt scintillation light is crucial for the operation of the TPC. It provides the essential t_0 (event time zero) for interactions within the detector volume, which is vital for accurately determining the position of ionization along the drift direction and for comprehensive 3D event reconstruction and calorimetry measurements. The SBND PDS is designed to achieve a high total light yield, up to 100 photoelectrons per MeV of energy loss.

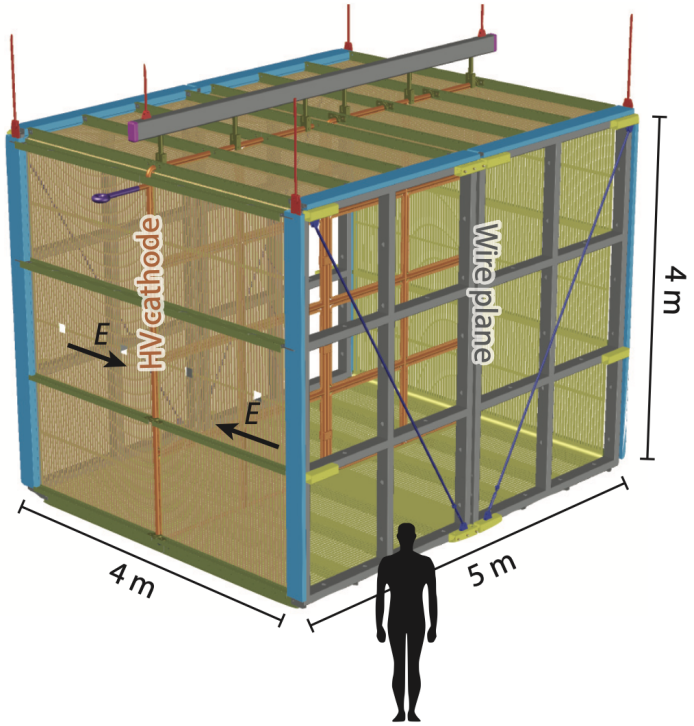

Figure 4.3: The SBND contains two TPC drift regions on either side of a central HV cathode. Each 2 m drift region is read out by a pair of coupled anode plane assemblies,each approximately 4 m tall by 2.5 m wide. The TPC and photon detectors are suspended from a removable cryostat lid.

In addition to providing event timing, the PMTs serve as the primary input to the SBND trigger system. Triggers are generated when a certain number of PMTs exceed a predefined threshold, in coincidence with the timing information from the Booster Neutrino Beam. The system also features a unique second, parallel TPC readout stream that continuously records ionization signals. This capability enables the detection of supernova neutrino interactions in the event of a galactic supernova burst during SBND's operational lifetime, and it contributes to the development of advanced TPC-based data selection and trigger strategies for future LArTPCs such as DUNE. Achieving nanosecond-level time resolution is a key objective for SBND, as it is critical for distinguishing signals from neutrino beam bunches and effectively rejecting backgrounds.

The first signal that alerts to the presence of an event is scintillation light, which arrives much sooner at the anode and cathode than electrons and ions. For this

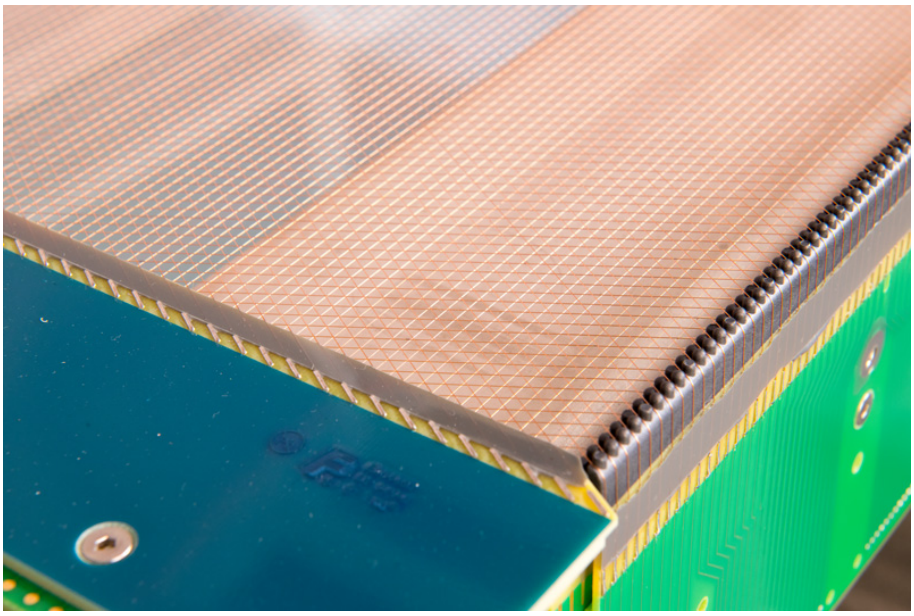

Figure 4.4: Detailed view of an Anode Plane Assembly (APA) showing the three layers of wires crossing at a 60 degree angle and spaced 3mm apart.

reason, a PDS is used in SBND to detect the scintillation light, thus providing almost immediate timing information about the event. The PDS consists of 24 PDS boxes, with 12 boxes behind each APA wall. Each box contains five PMTs: four TPB-coated PMTs positioned at the vertices of a square and one uncoated PMT at the center (see Figure 4.6).

The TPB coating is necessary because argon scintillation light falls in the VUV, a wavelength to which the PMTs are not sensitive. The coating shifts the light into the visible range, allowing detection. The uncoated PMT detects light reflected from the CPA wall, which is covered with a reflective TPB-coated foil. This configuration allows one to distinguish between direct and reflected scintillation light, which is crucial for reconstructing event topology. In particular, it enables the PDS to independently determine the position along the x-axis (drift direction).

Each box also contains eight ARAPUCAs (see Figure 3.11), an innovative device developed for LArTPC experiments. In SBND, ARAPUCAs are implemented to evaluate their performance for future use in DUNE. They capture scintillation photons with extremely high efficiency by trapping them inside a box with highly reflective inner surfaces, reducing the need for a large active photon detection system. UV scintillation light enters the ARAPUCA through a dichroic filter, which is transparent at the initial wavelength but reflective at other wavelengths. A

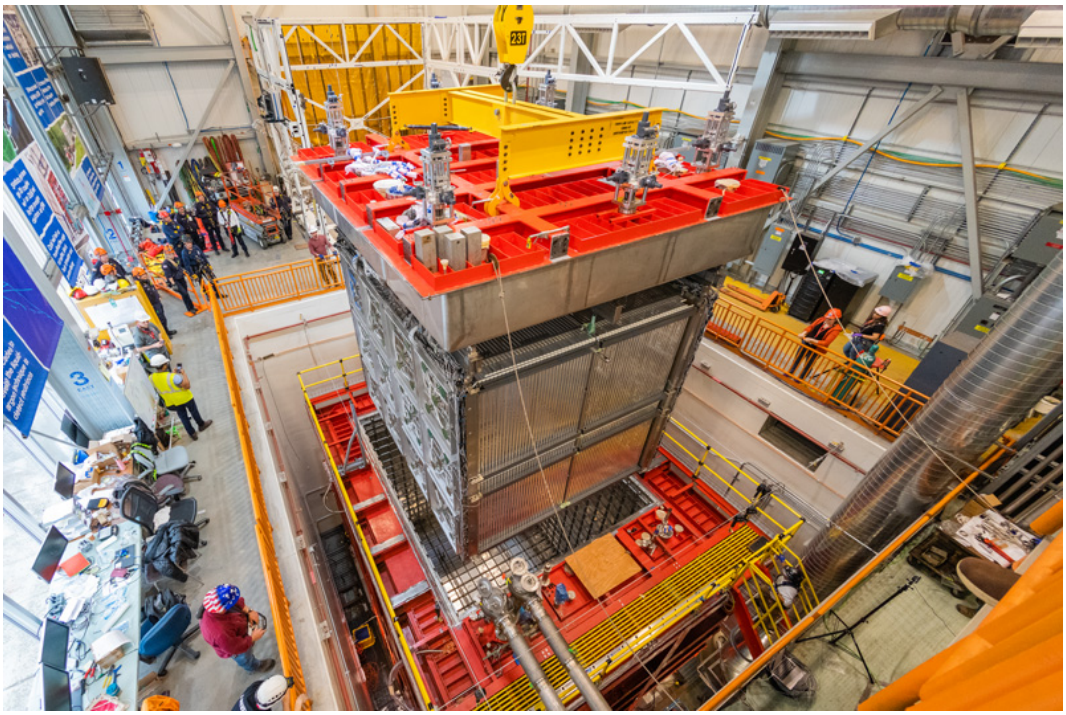

Figure 4.5: The assembly of detector and cryostat lid being lowered into the SBND membrane cryostat.

wavelength-shifting sheet on the input side converts photons into a range that can be reflected by the filter. Trapped light is then detected by a silicon photomultiplier (SiPM) on the inner surface of the box.

SBND uses an improved version called X-ARAPUCAs, which incorporates an acrylic sheet to capture photons via total internal reflection and guide them to one end where they are detected (see Figure 4.7). This reduces the number of photon collisions, enhancing the detection efficiency [18].

Figure 4.10 illustrates the geometric arrangement and spatial distribution of the PDS boxes.

4.3 SBND Cosmic Ray Tagger

Given its surface location, the SBND detector is continuously exposed to a substantial flux of cosmic rays, primarily muons, which could otherwise pose a significant background for neutrino analyses. To effectively mitigate this, SBND is equipped

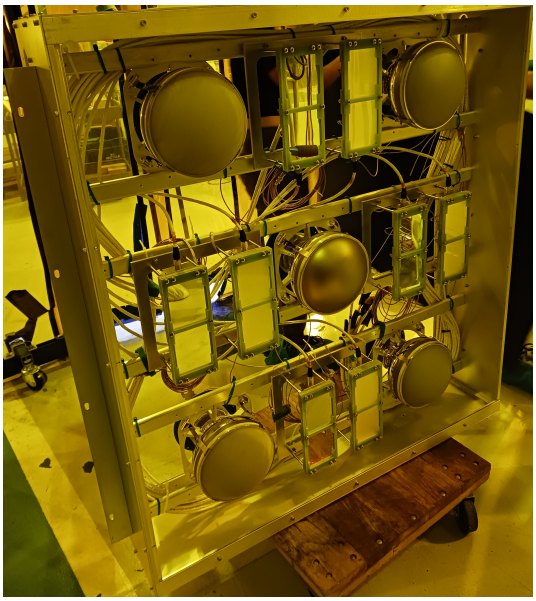

Figure 4.6: One of 24 Photon Detection System (PDS) modules, housing five PMTs and eight X-ARAPUCA devices for light detection.

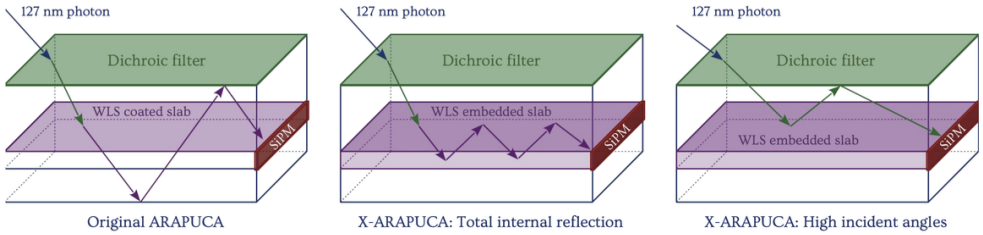

Figure 4.7: On the left is the first model of ARAPUCAs. The center and the right figures show the X-ARAPUCAs models when the photons undergo total reflection and when they have high incident angles respectively.

with an external Cosmic Ray Tagger (CRT) system, a vital tool that detects cosmic ray muons and precisely measures their crossing time and coordinates relative to events occurring within the TPC. This system is indispensable, as approximately five or six cosmic muons are expected per neutrino event in SBND.

The CRT system provides nearly 4π solid angle coverage around the detector, composed of planes of extruded scintillator strips read out by SiPMs. Specifically, it consists of seven such planes, each comprising multiple scintillating modules. To enhance resolution in the region of maximal cosmic ray flux, an additional pair of

planes is installed 3 meters above the top TPC layer, forming a telescope capable of achieving a high coordinate resolution, as shown in figure 4.8.

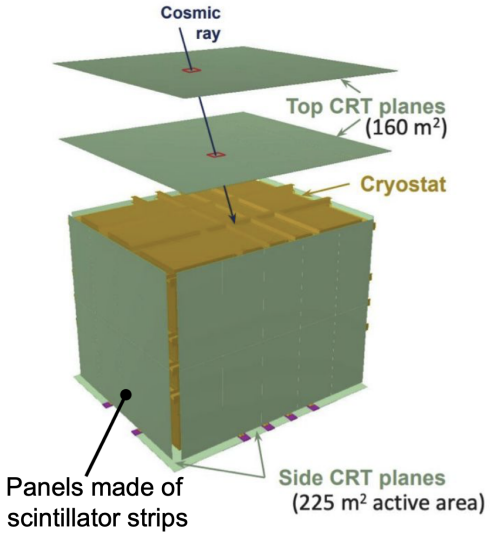

Figure 4.8: Schematic of the Cosmic Ray Tagger structure. It is composed of scintillating fiber panels covering the six faces of the detector, with an additional top layer to more efficiently reduce the influence of cosmic rays.

Individual scintillating strips are extruded from a polystyrene-based mixture, typically having a cross-section of 10x112 mm (with some variations for the bottom layer) and lengths ranging from 1.8 to 4.5 meters. SiPMs are connected to the edge of each strip, and their signals are transmitted to Front-End Boards (FEBs). These FEBs are designed to provide individual bias voltage to each SiPM, amplify and shape the output pulses, and generate time stamps with a resolution of approximately 1 ns.

The triggering logic of the CRT incorporates a hardware coincidence mechanism ("any in X and any in Y" layers, see Figure 4.9) to significantly reduce uncorrelated background noise, particularly from gamma-photons originating from environmental radioactivity. Cosmic ray data is precisely time-stamped using both external GPS signals (1 PPS) and accelerator beam spill signals, enabling accurate integration with data from other detector subsystems during event building.

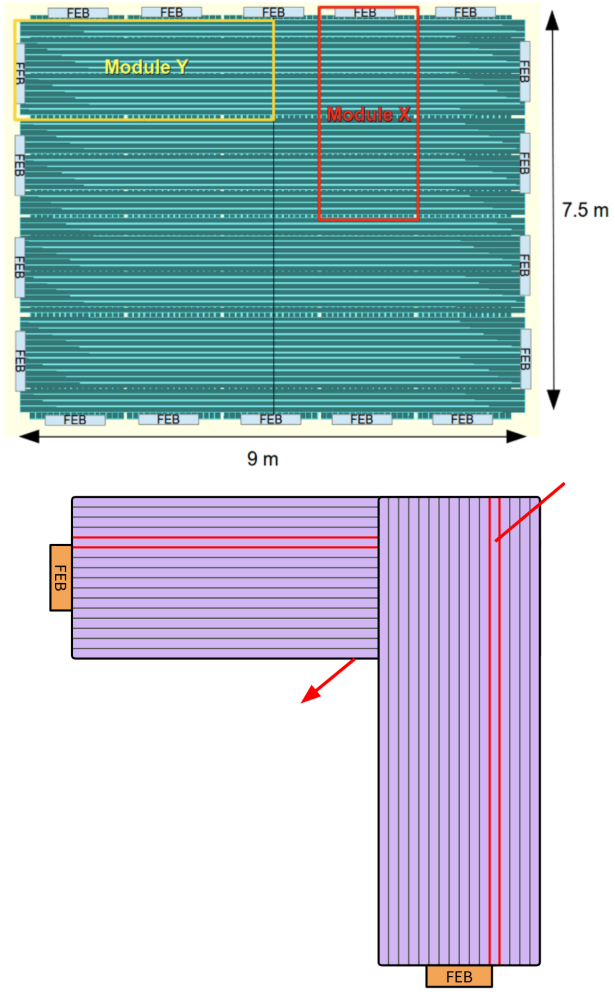

Figure 4.9: The SBND Cosmic Ray Tracker consists of seven planes made up of several scintillating modules. Each of these planes is composed of modules arranged in two perpendicular layers, with each module read out at its outer edge by a Front-End Electronics Board (FEB). Each FEB requires a coincident signal above the threshold from the two channels of a scintillating strip to avoid dark-noise fake hits. A strip in the perpendicular layer must also trigger simultaneously through connected trigger loops. This 4-fold coincidence greatly minimizes radiogenic backgrounds that do not pass through both scintillator layers. The figure above shows an example of the east or west wall.

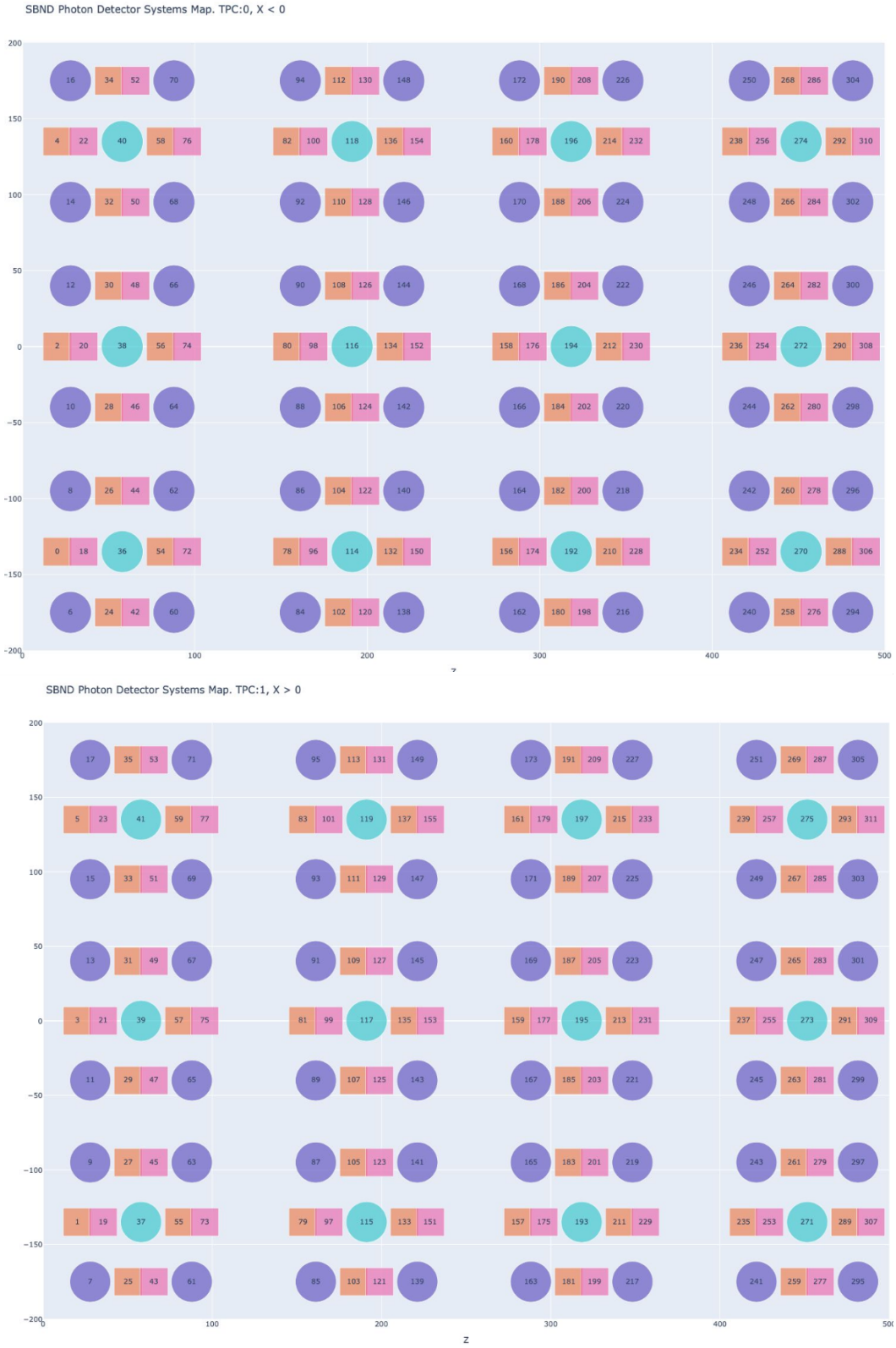

Figure 4.10: Map of the PDS box layout in the external areas of the East and West anodes.

Part II

Experimental Data Analysis

5 Commissioning of the Cosmic Ray Tagger

5.1 Hardware activities

A significant part of my internship at Fermilab was focused on hardware activities, particularly in assembling and commissioning the upper layers of the Cosmic Ray Tagger. Specifically, I worked on the CRT Top Low and CRT Top High layers. This involved hands-on participation in the integration and placement of scintillator modules, ensuring that the detection system was properly aligned and functioning. Additionally, I collaborated with other members of the CRT group to interconnect all modules and verify that they were properly grounded, ensuring stable and reliable electrical performance.

5.1.1 CRT Top Low commissioning

In the initial weeks of my internship, my role primarily involved verifying the proper delay of all cables that were later installed, utilizing an oscilloscope and a waveform generator to ensure that the signal waveform was not altered. Once each cable was tested, it was labeled to indicate its installation location, and colored tape was applied to differentiate the cables corresponding to each of the four types of signals connecting the FEBs. On August 13th, the installation and validation of the CRT Top Low were completed. As reference, in Figure 5.1, the apparatus status before the installation of the CRT Top Low and Top High layers is also shown.

5.1.2 CRT Top High commissioning

In the second part of my internship, I focused on the commissioning of the Top High layer of the CRT. The activities involved were essentially the same as those carried out for the installation of the CRT Top Low, including testing cable delays and signal shapes, as well as labeling each cable with colors and tags. Unlike the Top Low layer, however, the installation of the cables for the CRT Top High required the use of a basket (as shown in Figure 5.2), operated by specialized personnel, to access the FEBs in the central, north, and south regions of the CRT.

In addition to connecting the cables to the various FEBs, the grounding of the different modules was also performed. The installation of this layer was completed

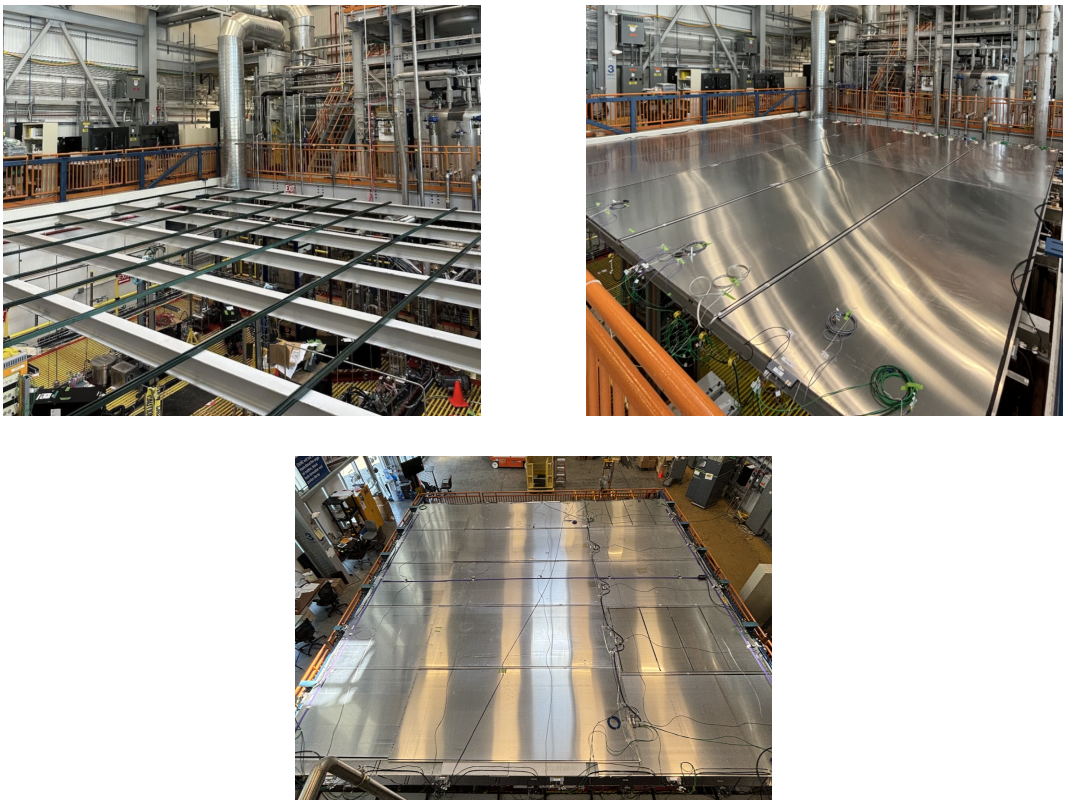

Figure 5.1: Commissioning stages of the CRT system: (top left) initial setup without the two top layers, (top right) installation of the Top Low module, and (bottom) final configuration with the Top High module.

one month after the installation of the CRT Top Low, on September 13th (see Figure 5.1).

5.2 Software and data analysis activities

Alongside the hardware activities of my internship, I also had the opportunity to analyze data collected by SBND. Specifically, I focused on three main tasks: first, I worked on resolving an issue related to the counting rate of the West Wall, which required direct intervention on the connections of the FEBs; second, I validated the timing distribution from the initial runs of the CRT Top High acquisition to ensure that the installation of all cables had been executed correctly; and finally, I calculated the veto efficiency of the CRT for contained neutrino events. For these

Figure 5.2: Photo of me working from the basket to ground the modules of the CRT Top High.

tasks, I wrote analysis scripts in ROOT, accessing the data trees of the experiment to extract and analyze the relevant information.

To understand how CRT data are reconstructed, it is important to first describe the logic of the readout electronics and the reconstruction process. The electronic readout system of the SBND Cosmic Ray Tracker (CRT) employs a sophisticated hardware coincidence logic, primarily implemented on the Front-End Board (FEB), to validate cosmic ray events and suppress uncorrelated background noise. Each FEB services 32 Multi-Pixel Photon Counters (MPPCs) from 16 scintillating strips, utilizing a Xilinx Spartan-6 FPGA for trigger realization. A preliminary event trigger is formed by applying an AND logic to the fast-shaped and discriminated signals (e.g., C0 & C1) corresponding to the two wavelength-shifting fibers within a single scintillating strip. These 16 strip-coincidence signals are then combined with an OR logic to form a primary event trigger.

A crucial aspect of the FEB design is the use of four external connections for synchronization and coincidence validation: two reference timing inputs, T_0 and T_1, and two coincidence ports, T_{in} and T_{out}. The T_0 input is typically connected to a 1-PPS signal from an external GPS unit, providing a global timestamp for events, while T_1 is reserved for the accelerator beam spill pulse. The T_{in} and T_{out} ports enable the necessary inter-layer hardware coincidence logic, rejecting background events by confirming that a charged particle has traversed both the X and Y coordinate layers. This is realized by daisy-chaining multiple FEBs within a layer using two

common coaxial cable rings that function as a wired-OR circuit for the trigger signals.

Upon an internal primary event trigger, the FEB generates a 160 ns pulse, T_{out}, which propagates onto its layer's coaxial ring. Simultaneously, the FEB awaits a valid event pulse at its T_{in} input within a 150 ns validation window. The T_{in} input for a module in the X-layer is sourced from the coaxial ring of the perpendicular Y-layer, and vice versa. The presence of a signal at T_{in} within this window validates the event, causing the internal Sample-and-Hold (S/H) circuit to maintain the HOLD state and permit digitization of the analog signals by the CPU. Conversely, if no signal is received, the HOLD signal is rapidly reset, and the event is discarded, thus minimizing dead time [18].

The data acquired by the CRT are initially in raw format and require a multi-step reconstruction process to be converted into physically meaningful objects for analysis. The reconstruction pipeline begins with a decoder that converts the raw data into an offline format. From this, the first reconstructed objects, called Strip Hits, are created. These objects identify which scintillating strips in each active module registered a signal above the hardware threshold, corresponding directly to the hardware trigger logic.

Following the identification of strip hits, the next step is the formation of Cluster Groups. This process groups coincident strip hits within each tagger wall (layer). These clusters represent the energy deposition from a single particle traversing the active volume of a given layer. The spatial information from these clusters is then used to create Space Points, which are 3D points derived from the clusters, representing a charged particle's position within a single tagger wall.

Finally, the reconstruction process culminates in the creation of Tracks. This step groups coincident space points between the X and Y tagger walls, establishing the trajectory of the particle through the CRT system. This complete process, from the initial hardware-level trigger to the final track reconstruction, is essential for filtering background noise and for accurately identifying and characterizing cosmic ray events within SBND [18].

5.2.1 Debugging of the West wall

During the first weeks of my internship, an unusually high rate of cosmic rays was observed in the West Wall, which had already been installed and validated. A possible cause for this anomaly could be a wrong connection between the T_{in} and T_{out} cables in the daisy chain of the wall. If these two cables are reversed, instead of obtaining two separate daisy chains, only a single chain is formed, removing this coincidence requirement and resulting in a high rate. The first step to verify this

behavior involved using four spare FEBs and a multimeter to measure the resistance between the two FEB chains, both in the correct connection scenario and in the case where the wires were inverted. Upon checking the actual impedance recorded between the ends of the two chains in the West Wall of the CRT, we found a value consistent with the situation where the cables were incorrectly connected, resulting in a single daisy chain instead of two separate ones. To definitively confirm that the intervention was correct, four different runs were acquired before and after the cables were properly connected. Specifically, two plots were generated for each run: one showing the rate of recorded events and another displaying the ratio of space points to strip hits. Space points are generated only when a coincidence and spatial overlap are found between the two perpendicular layers (as shown in Figure 4.9), while strip hits are associated with any signal generated in a given module, regardless of whether there is a coincidence in the perpendicular module. For a properly functioning system, we expect the ratio of space points to strip hits to be approximately 1, because the T_{in}/T_{out} coincidence system should ensure that we only read out strip hits that could contribute to a space point.
Figure 5.3 shows that with subsequent interventions, the rate recorded by the individual modules has indeed decreased, approaching a value similar to that recorded by the other walls. Additionally, the ratio of space points to strip hits has converged towards 1. In the first run, due to the lack of separation between the two daisy chains, the modules of the perpendicular layers were not properly coupled, resulting in too many strip hits.

As can be seen by observing the plot 5.3 in the top row, the rate of observed cosmic rays decreases to a value more similar to that recorded by the other walls. Additionally, it can be noted that the distribution of rates reflects the physical arrangement of the modules.

In the first four bins, as well as in the subsequent four, an increasing trend can be observed. These bins correspond to the two groups of horizontal modules, starting from the lowest one, which records the smallest rate, and gradually increasing up to the highest one. This effect is due to the stronger shielding experienced by the modules located in the lower positions.

In contrast, regarding the last groups of 5 bins, it is noted that within the individual groups, the rate remains fairly constant, while the rate recorded by the first group is greater than that recorded by the second. These groups correspond to the vertical modules, with the group with the higher rate corresponding to the group of vertical modules arranged in the upper row, while the one with the lowest rate corresponds to the one in the lower row. For a better visualization of the arrangement of the modules in space, please refer to Figure 5.4.

5.2.2 CRT Top High validation

The second part of my work focused on validating the timing signals of the CRT Top High after installation. To achieve this, I analyzed three different runs, each lasting approximately 20 minutes. The first run (number 16837) was acquired by sending the PPS signal to the T_0 channel, while a fake beam signal was provided to the T_1 channel. In this configuration, the fake beam consisted of a burst of pulses spaced by about 50 ms, with successive bursts separated by 900 ms. Two additional runs (numbers 16861 and 16903) were acquired by sending the PPS signal to T_1 instead. Having a simple, single frequency reset sent to T_1 allowed it to be verified in the same manner as T_0.

The first quantity analyzed was the set of flags recorded during these acquisitions. Each flag is an integer between 0 and 15 associated with a four-bit binary code: the ___x bit is set to 1 when the T_0 signal is valid, the __x_ bit plays the same role for T_1, the _x__ bit is set to 1 when the event corresponds to a reset signal of the T_0 channel, and the x___ bit indicates a reset of T_1. In this context, an invalid signal means that a reset was not received within the required time, causing the clock to roll over.

For run 16837, the expected flags were `0011`, `0111`, and `1011`, corresponding to flag values 3, 7, and 11, respectively. For the swapped-signal runs, the expected flags were `0010` and `1010`, corresponding to flag values 2 and 10. The recorded distributions matched these expectations, as shown in Figure 5.5.

After ensuring that the FEBs were correctly powered, it was important to verify that the four timing signals worked as expected. For the reference timing signals T_0 and T_1, two main analyses were performed. The first was to verify that the temporal distribution matched the signal sent to the detector. As seen in Figures 5.6 and 5.7, the expected behavior was indeed observed during the different runs.

Another important quantity to evaluate was the clock drift, i.e., the deviation of the FEB's internal clock from the more precise PPS signal between consecutive resets. To study this, only reset events were selected. For run 16837, I considered T_0 reset events with flag = 7, while for runs 16861 and 16903, I selected flag = 10 events corresponding to T_1 validation. The clock drift was obtained by subtracting 10^9 ns (1 s, the expected reset period) from the time signal. A stable clock corresponds to a narrow distribution centered around 0, which was indeed observed for the T_0 reset signal. In contrast, for T_1 the distribution remained narrow but was not centered at 0, showing instead random positive and negative offsets. The different behavior of the two timing signals is illustrated in Figure 5.8.

One possible cause for this behavior is that FEBs might struggle with the T_1 signal if they do not receive a proper T_0 signal. To test this hypothesis, a new

run was performed where the PPS signal was sent to T_0 (which previously had no reference signal) and a periodic signal, slightly phase-shifted from the PPS, was sent to T_1. In this new configuration, plotting the T_1 clock drift produced the expected zero-centered distribution, confirming the correct operation also of the T_1 channel.

In addition to validating the T_0 and T_1 signals, it was also necessary to verify the correct operation of the T_{in} and T_{out} daisy chains, in order to prevent issues similar to those that required the debugging described in Subsection 5.2.1.

For this, I created a plot where each point corresponded to any coincidence in the readout of X and Y modules. In Figure 5.9, distinct groups can be seen corresponding to the geometrical layout and overlap of the modules.

Modules with greater overlap (highlighted in green in Figure 5.9) have a higher rate, partially overlapping modules show a lower rate (orange, Figure 5.9), and modules with minimal overlap have the lowest rate (bordeaux, Figure 5.9). Black points in the lower part of the graph represent coincidental readouts from non-overlapping X and Y modules. This correspondence between rate and module geometry confirms that the T_{in} and T_{out} chains are functioning correctly.

Following these analyses, it can be concluded that the Top High layer of the Cosmic Ray Tagger has been successfully installed and is operating as expected.

5.2.3 Measurement of the efficiency of using a CRT veto in a contained neutrino trigger

One application of the CRT is to veto entire events, either at the trigger level or during analysis, whenever activity is recorded in coincidence with the beam spill. For this reason, the final analysis I carried out during the internship focused on evaluating the CRT veto efficiency in contained neutrino events, defined as the probability that the CRT remains untriggered during such an event. To determine this value, the first step was to analyze the time distribution of events around the trigger signal. I plotted the timestamp value relative to the T_0 reference signal, subtracting the trigger time in run 16906. As shown in Figure 5.10, the distribution is not uniform but rather trapezoidal in shape. For this reason, to calculate the veto efficiency, I considered only events recorded within a time window of ±15 ms from the trigger signal to ensure all signals were being captured within a reliable region.

Next, I plotted the temporal distribution of events within this selected time window, as shown in Figure 5.11.

The signals appeared clustered into subgroups lasting up to ~100 ns. It is reasonable to assume that each subgroup corresponds to the activity of a single source (one cosmic muon), which justifies grouping them together. Accordingly, I treated

all signals occurring within a 200 ns window from the first signal in each subgroup as a single event. I then counted the number of such 200 ns subgroups detected within each trigger window. This method provided a reliable estimate of the cosmic ray rate impacting the detector, based directly on the raw CRT data. Figure 5.12 shows the resulting distribution of the cosmic ray rate on the south, east, and Top Low walls of the CRT.

The CRT veto efficiency can then be estimated assuming the cosmic ray rates on the various walls are as follows:

- South wall: 1150 Hz;
- North wall: 1300 Hz;
- East wall: 1500 Hz;
- West wall: 1500 Hz;
- Bottom wall: 2300 Hz;
- Top Low wall: 5150 Hz;
- Top High wall: 5150 Hz.

The overall cosmic ray rate on the detector is approximately 18,000 Hz. Given that a neutrino beam spill lasts about 2 μs, the CRT veto efficiency, considering all walls (including the Top High), is about **96.4%**, demonstrating the high efficiency of the CRT's veto function.

It should be noted, however, that for this first study the measured rates of the individual CRT walls were analyzed independently of one another. As a consequence, the resulting efficiency represents more of a lower bound on the true CRT veto efficiency, since a single cosmic source can contribute to the rates of multiple walls simultaneously. A natural next step to improve this estimate would be to repeat the analysis while accounting for the geometry of reconstructed tracks and their correlated contributions across different CRT walls.

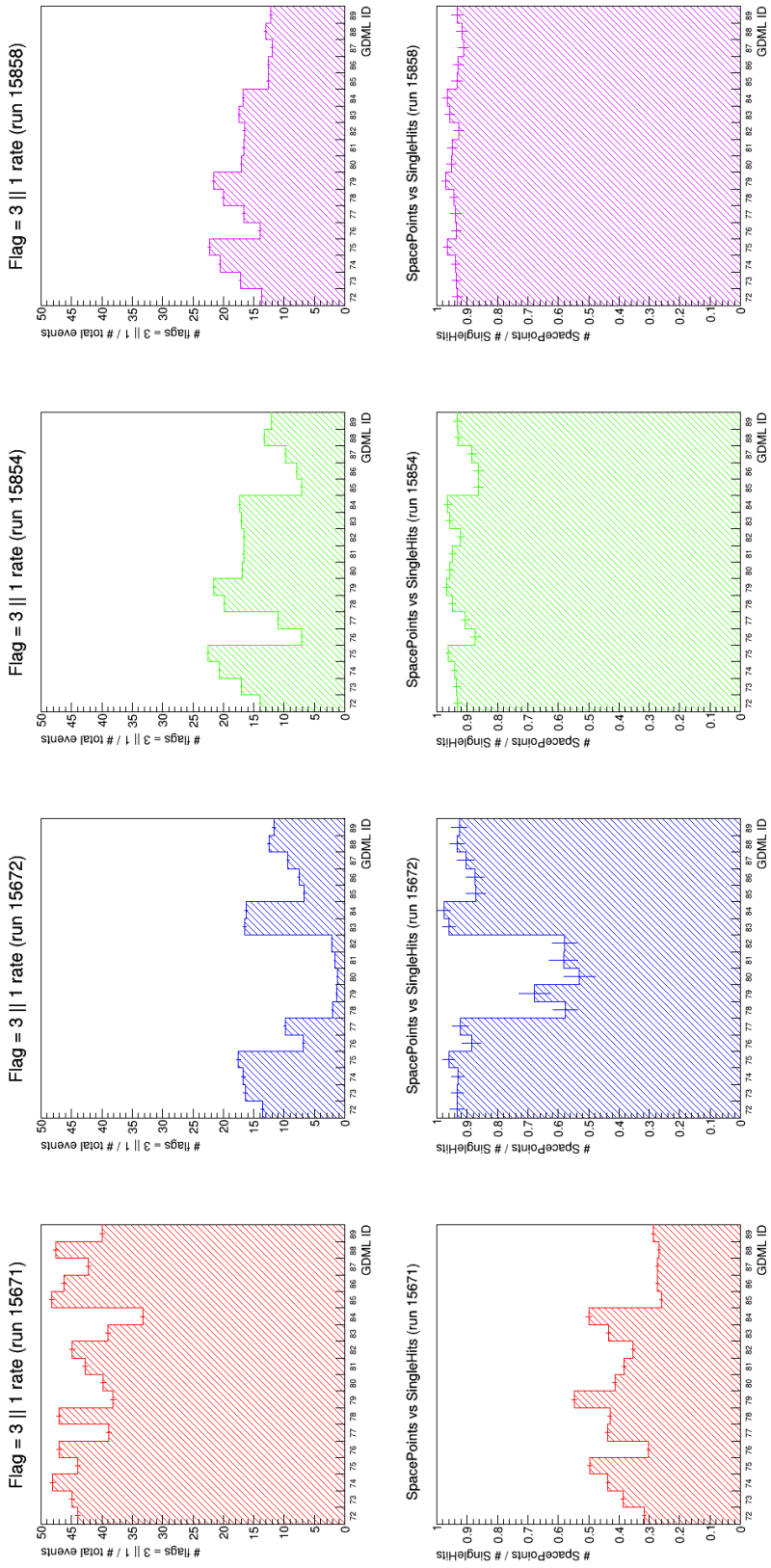

Figure 5.3: The top row displays the trend of the cosmic ray rate across the different modules of the West Wall throughout the various interventions. The second row shows the measured ratio between space points and strip hits.

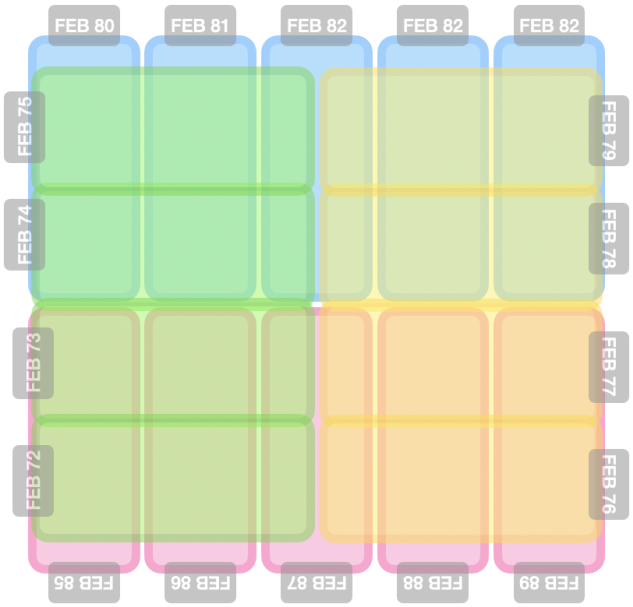

Figure 5.4: Schematic representation of the arrangement of the modules in the west wall, front view.

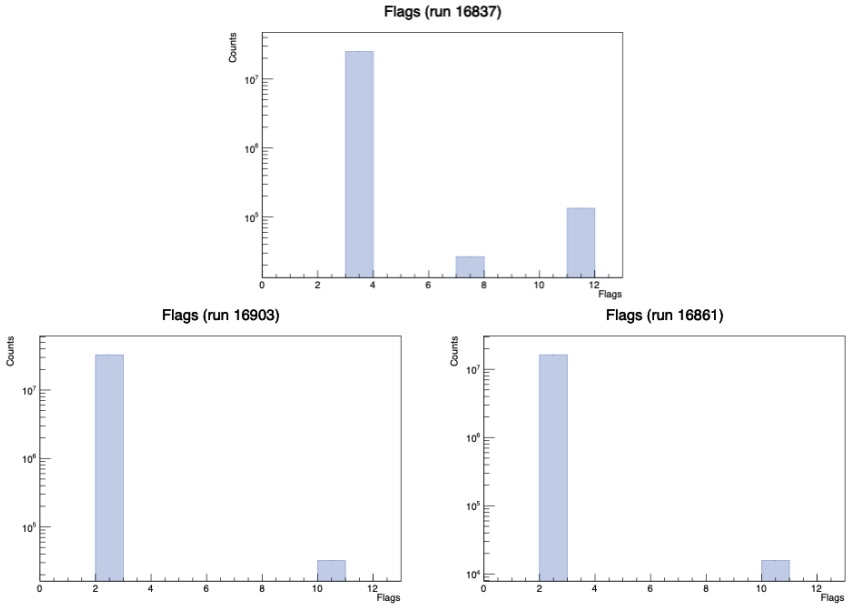

Figure 5.5: Plot of the flag values obtained during the three different runs.

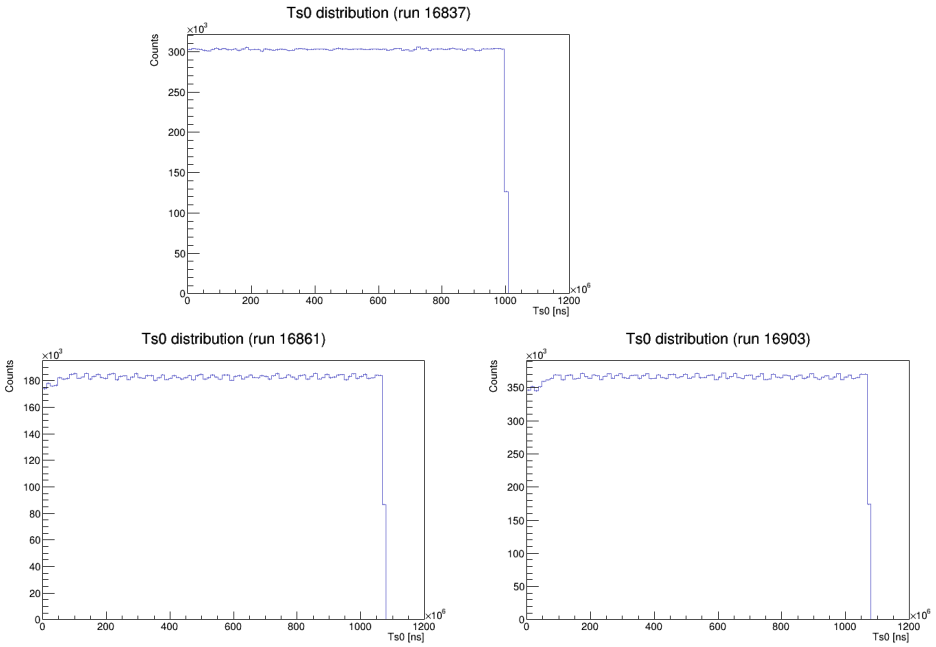

Figure 5.6: Distribution of T_0 for different runs, considering only events with flag values equal to 2 or 3.

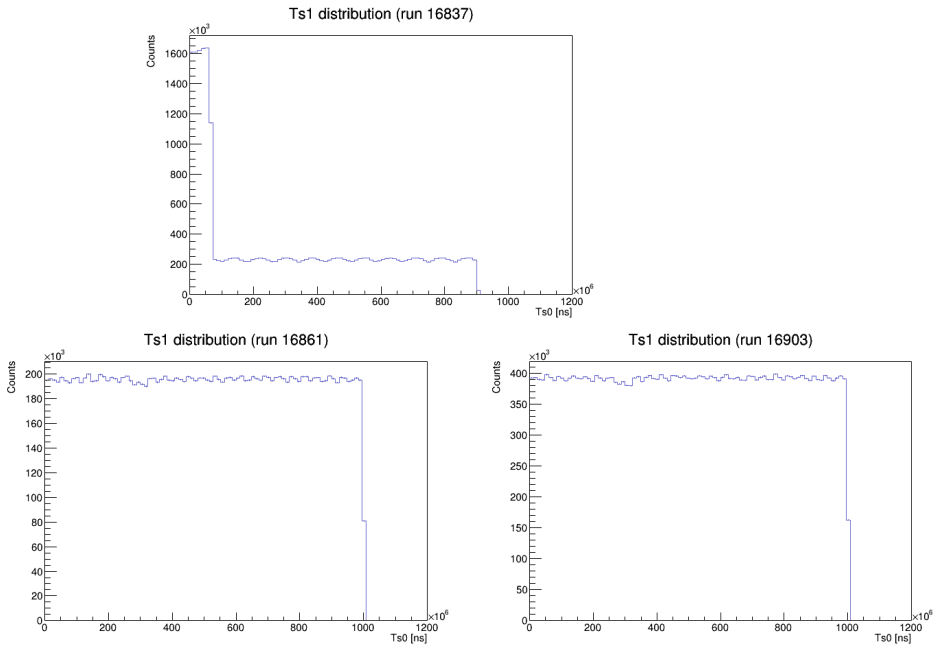

Figure 5.7: Distribution of T_1 for different runs, considering only events with flag values equal to 2 or 3.

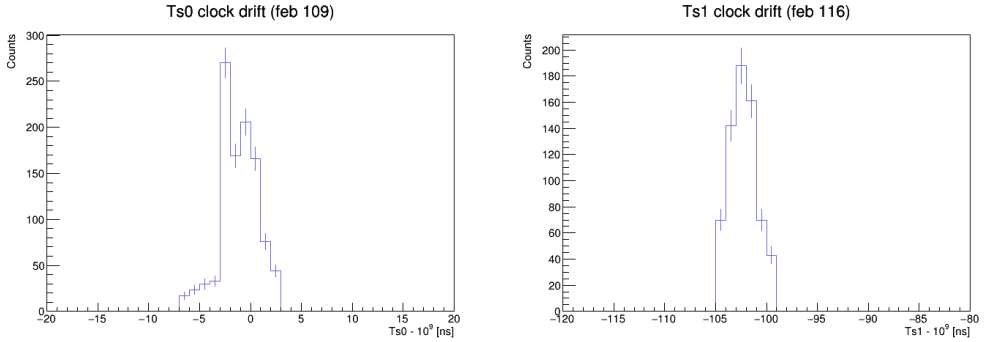

Figure 5.8: Clock drift distributions for the T_0 (left) and T_1 (right) reset signals.

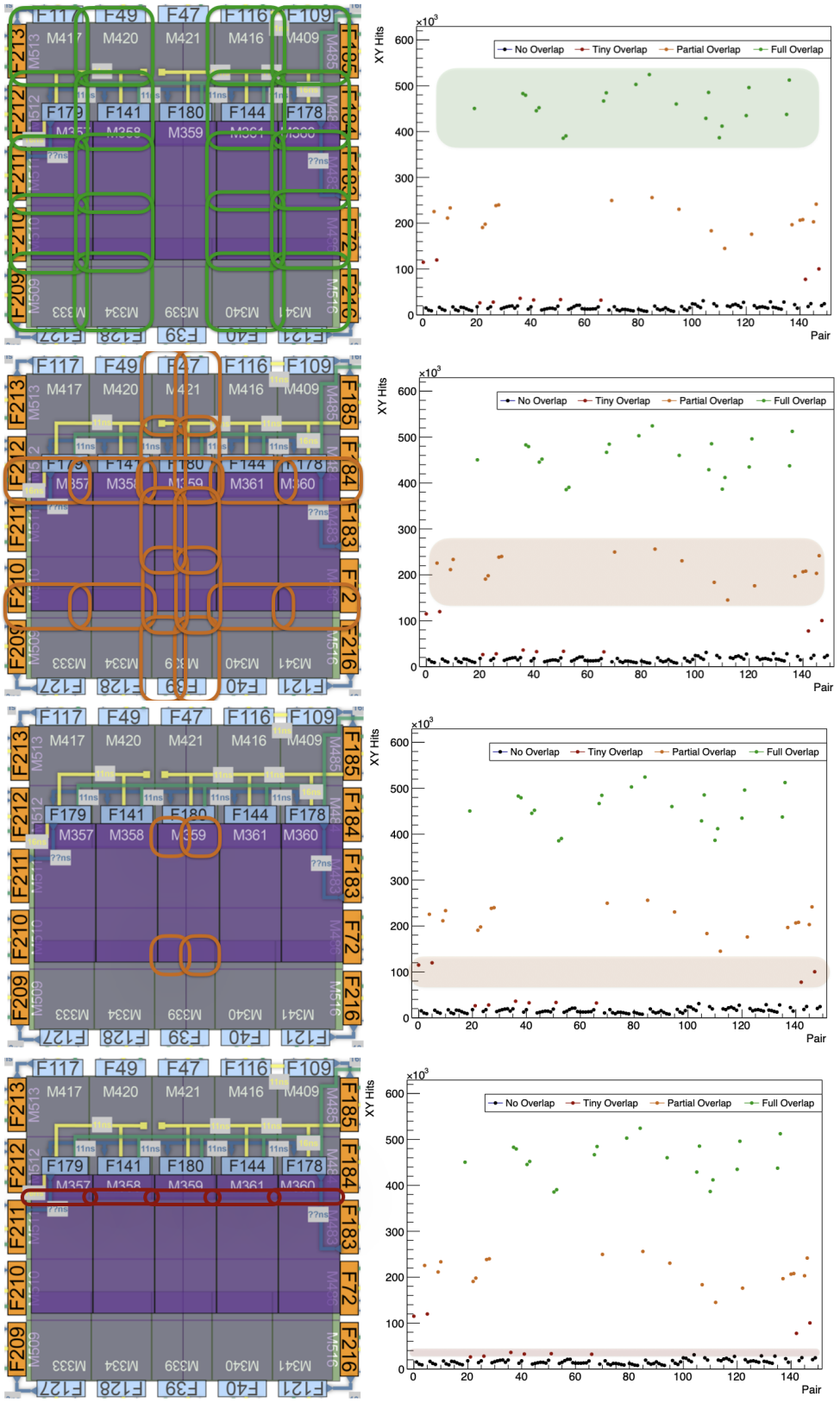

Figure 5.9: Image showing the correspondence between the rates and the geometric overlap of the different modules. From top to bottom, respectively: full, partial, minor partial and tiny overlaps.

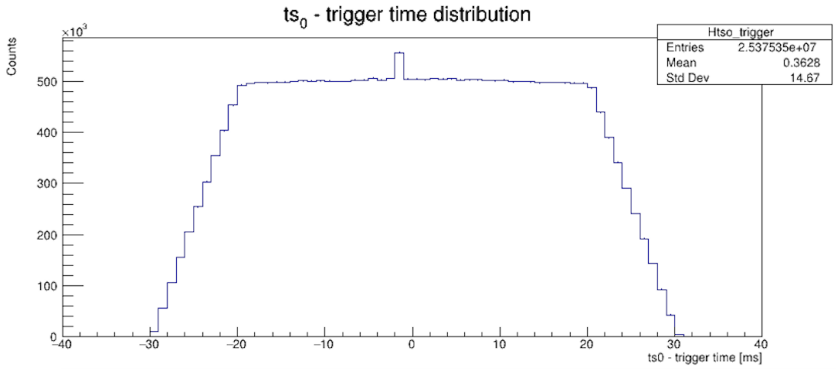

Figure 5.10: Time distribution of the signals, based on T_0, with respect to the trigger time.

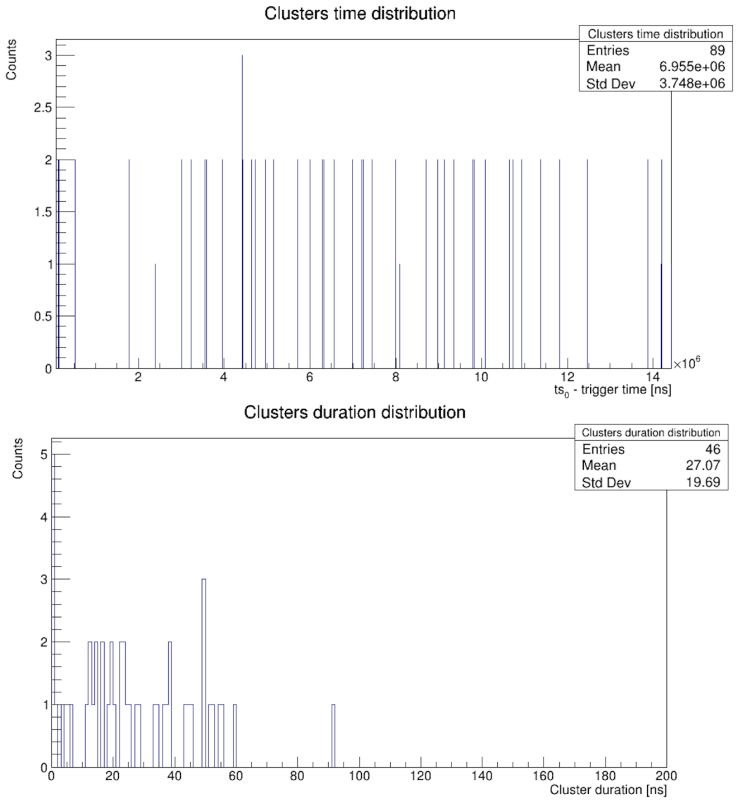

Figure 5.11: In the top image, the distribution of events corresponding to physical signals (flag = 3 [0011] indicating that the FEBs are receiving both T_0 and T_1 signals) within a trigger window is shown, with events clearly grouped into clusters. In the bottom image, the temporal distribution of events within one cluster is displayed, revealing that the events are grouped within a 200 ns window.

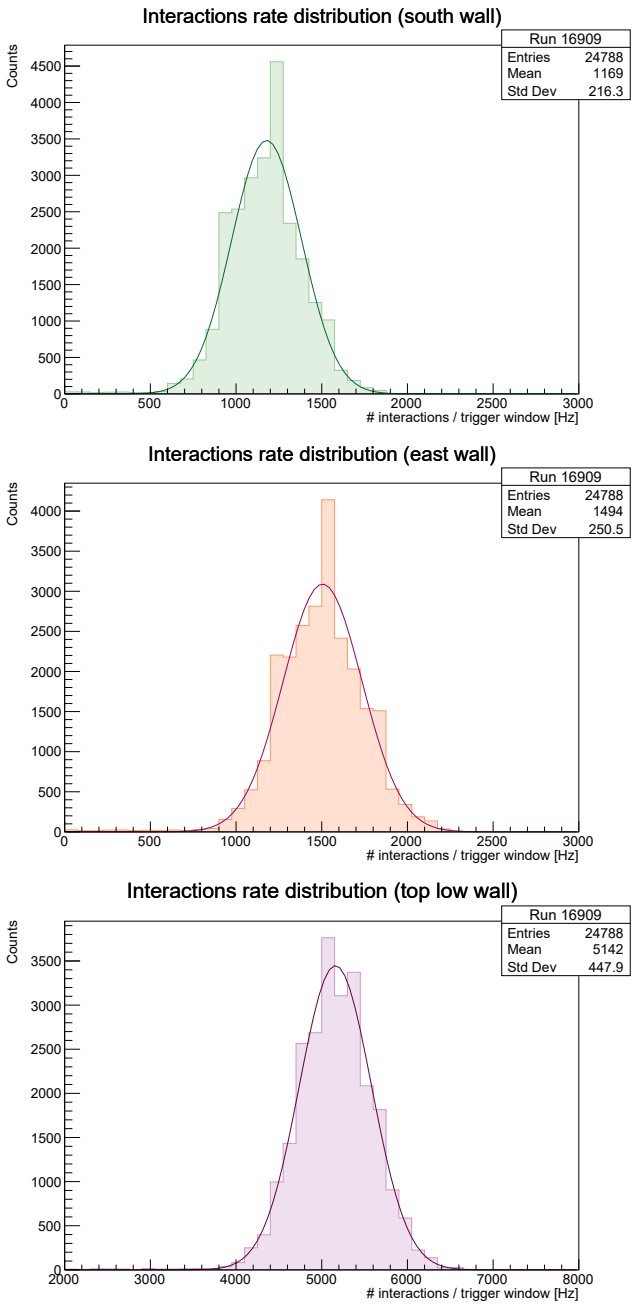

Figure 5.12: Distribution of the cosmic ray rate in the south, east, and Top Low walls of the Cosmic Ray Tagger.

6 Analysis of CRT–PMT Time Offsets

The aim of this analysis is to investigate in greater detail the relationship between the signals produced by the SBND Cosmic Ray Tagger (CRT) and those recorded by the Photon Detection System (PDS), with the goal of assessing the feasibility of exploiting such correlations as a discriminator between incoming and outgoing tracks in the detector.

In this context, incoming tracks are predominantly due to cosmic rays and are not of primary interest, whereas outgoing tracks are associated with neutrino interactions with argon nuclei. The primary process of interest in this work is the muon neutrino charged-current (CC) interaction:

$$\nu_\mu + \mathrm{Ar} \;\longrightarrow\; \mu^- + X, \tag{6.1}$$

in which the produced muon exits the detector and is identified by the CRT, as illustrated in Figure 6.1. Such signal topologies are characterized by a particle track originating within the liquid argon volume, propagating outward to the detector boundary, and corresponding to a CRT hit. A significant background for this analysis is, conversely, represented by incoming cosmic muons that stop inside the detector.

Figure 6.1: Visualization of a muon neutrino charged-current interaction within the SBND detector, projected onto the vertical collection plane. The image highlights a muon track exiting the detector, which should be taggable with the CRT

A powerful discriminant for distinguishing these two event topologies is the time difference between the CRT and PDS signals. The PDS provides a precise time reference for the event inside the detector, while the CRT records the moment a particle passes through its scintillator panels. This Time-of-Flight information can be used to determine the particle's directionality: for an exiting particle, the PDS signal will precede the CRT signal, whereas for an incoming particle, the CRT signal will be recorded first.

The present study evaluates the effectiveness of this approach for background rejection, providing a methodology and results of a detailed analysis aimed at establishing the correlation between CRT and PDS signals. It is important to note that the final state particles represented by X in Eq. (6.1) are at the theoretical ("truth") level and are not necessarily all observable or fully reconstructible.

SBND records an event—i.e., stores the detector signals to disk—whenever the photomultiplier tubes (PMTs) detect scintillation light within the 1.6 μs beam spill window. The neutrino beam is delivered in spills at a rate of up to 5 Hz. Approximately, the recorded events consist of 50% neutrino interactions within the active volume, 20% cosmic interactions, and 30% other beam-related activity. To estimate and subsequently subtract the cosmic contribution from downstream analyses, additional events are also recorded in a "fake" or "off-beam" window, where no beam is present.

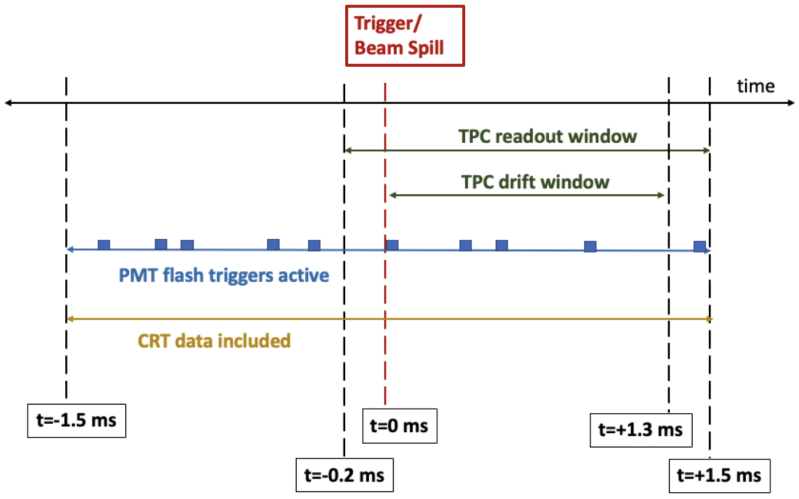

Figure 6.2: Schematic illustration of the temporal structure of an event in SBND, showing the relative timing of CRT and PDS signals.

Effective background rejection and event selection can be achieved by comparing

the CRT and PMT timing, determining the direction of a particle, and identifying whether the primary event trigger corresponds to a CRT hit. In this chapter, the first results of the combined CRT-PMT analysis are presented, highlighting how relative timing can be exploited for calibration, background rejection, and event selection.

6.1 Isochronous tracks and distance of closest approach

In the initial stage of the analysis, we selected and focused on the so-called *isochronous tracks*, i.e., tracks that maintain a constant distance from the cathode along the x-direction of the detector. To better study the behavior of cosmic rays, and thus the background signals, we used data from a run in which the neutrino beam was turned off, corresponding to so-called off-beam events. A dedicated trigger was employed to ensure the sample was enriched in these "crossing muon" events. Among these events, we initially selected signals corresponding to tracks traversing the detector from south to north, i.e., tracks passing through both the CRT and the TPC.

Starting from the sample of isochronous tracks, the analysis subsequently focused on the study of the distance of closest approach (DCA), defined as the minimum distance traveled by the scintillation photons produced along the track. Operationally, the DCA is given by the minimal distance between the reconstructed track (obtained from CRT space points) and the positions of the photomultiplier tubes (PMTs) located on both anode planes of the detector.

Formally, given a reconstructed track ℓ represented by a parametric equation

$$\vec{r}(t) = \vec{r}_0 + t\,\vec{v}, \quad t \in \mathbb{R}, \tag{6.2}$$

with $\vec{r}_0 \in \mathbb{R}^3$ a reference point on the track and $\vec{v} \in \mathbb{R}^3$ its direction vector, and a PMT located at position $\vec{p} \in \mathbb{R}^3$, the DCA is defined as

$$\mathrm{DCA}(\ell, \vec{p}) = \min_{t \in \mathbb{R}} \|\vec{r}(t) - \vec{p}\|. \tag{6.3}$$

The minimum can be computed analytically as

$$\mathrm{DCA}(\ell, \vec{p}) = \frac{\|(\vec{p} - \vec{r}_0) \times \vec{v}\|}{\|\vec{v}\|}, \tag{6.4}$$

where $\times$ denotes the vector cross product. This expression provides the shortest distance between the infinite straight line representing the reconstructed track and the PMT position (see Figure 4.10).

Figure 6.3 shows examples of the selected isochronous tracks, highlighting the point from which the DCA is calculated as well as the DCA itself. For reference, an indicative value of the photon time-of-flight (TOF) can be obtained by considering that the group velocity of scintillation photons in liquid argon is approximately 15 cm/ns (as obtained in Section 6.4).

From a physical perspective, isochronous tracks constitute an ideal test case for the study of the CRT-PDS correlation. Since they maintain a constant distance from the cathode, their topology is relatively simple and symmetric with respect to the drift direction. This makes them particularly well-suited to benchmark the reconstruction of the DCA and to investigate the timing correlation between CRT hits and PDS signals.

6.1.1 TITUS event dispaly

Another way to visualize the recorded events, and in particular the isochronous tracks acquired during off-beam runs, is by using the TITUS Event Display. This Python-based software provides a graphical interface that allows one to visualize the contributions of the three SBND subdetectors, namely the TPC, the PDS, and the CRT, for the purpose of reconstructing the full track topology.

Regarding the TPC, tracks can be visualized either from the two induction planes, oriented at $\pm 60^\circ$, or from the vertical collection plane. The latter provides the most straightforward interpretation, as it offers a projection equivalent to a "top view" of the TPC. In this representation, the x-axis corresponds to the wire coordinate, while the y-axis represents the drift time, i.e., the time required for the ionization electrons to reach the anode. Figure 6.4 shows an example of an isochronous track reconstructed using the collection plane. A long, straight track crossing the entire active TPC volume can be clearly identified, a topology characteristic of cosmic muons.

In addition to the TPC reconstruction, the TITUS display also enables the inspection of signals recorded by the Photon Detection System. In particular, one can analyze the waveforms measured by individual PMTs, which provide timing information on the scintillation light produced along the track (as shown in Figure 6.5). This information is essential for studying the correlation between track geometry and optical response.

Finally, for a complete description of the event, one can also exploit the information provided by the Cosmic Ray Tagger (see Figure 6.6). In the case of

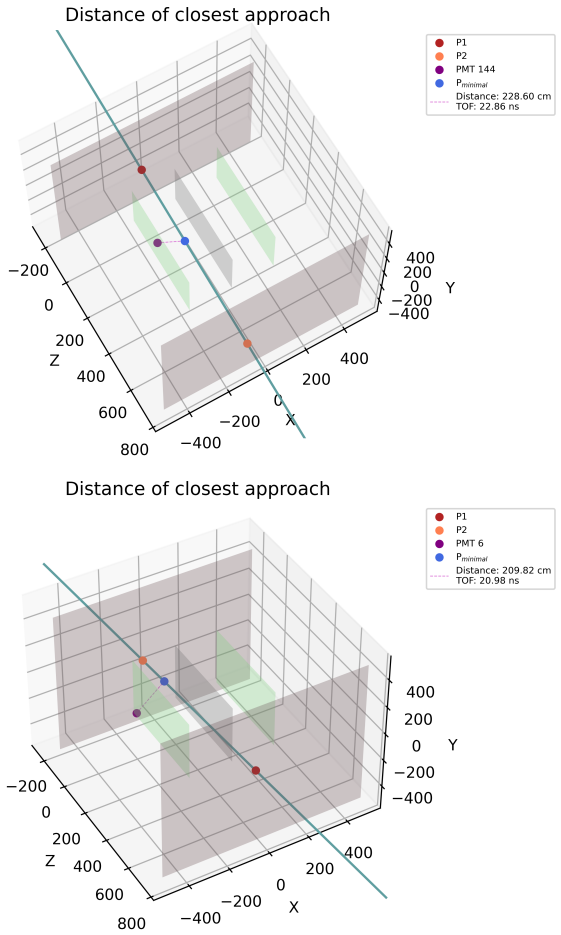

Figure 6.3: Schematic representation of cosmic ray tracks traversing the detector. The outer gray planes represent the north and south walls of the CRT. The smaller internal planes show the PDS planes located behind the two TPC collection planes. The red and orange points, referred to as space points, indicate where the track crosses the CRT. The light blue point represents the origin for the calculation of the DCA, while the purple point shows the specific PMT being considered in the analysis.

isochronous tracks, the CRT contributes by identifying space points located on the north and south external faces of the detector, where the muon associated with the selected track is expected to enter and exit. The combination of TPC, PDS, and CRT views thus offers a powerful tool for validating reconstruction algorithms and for characterizing cosmic-ray background events.

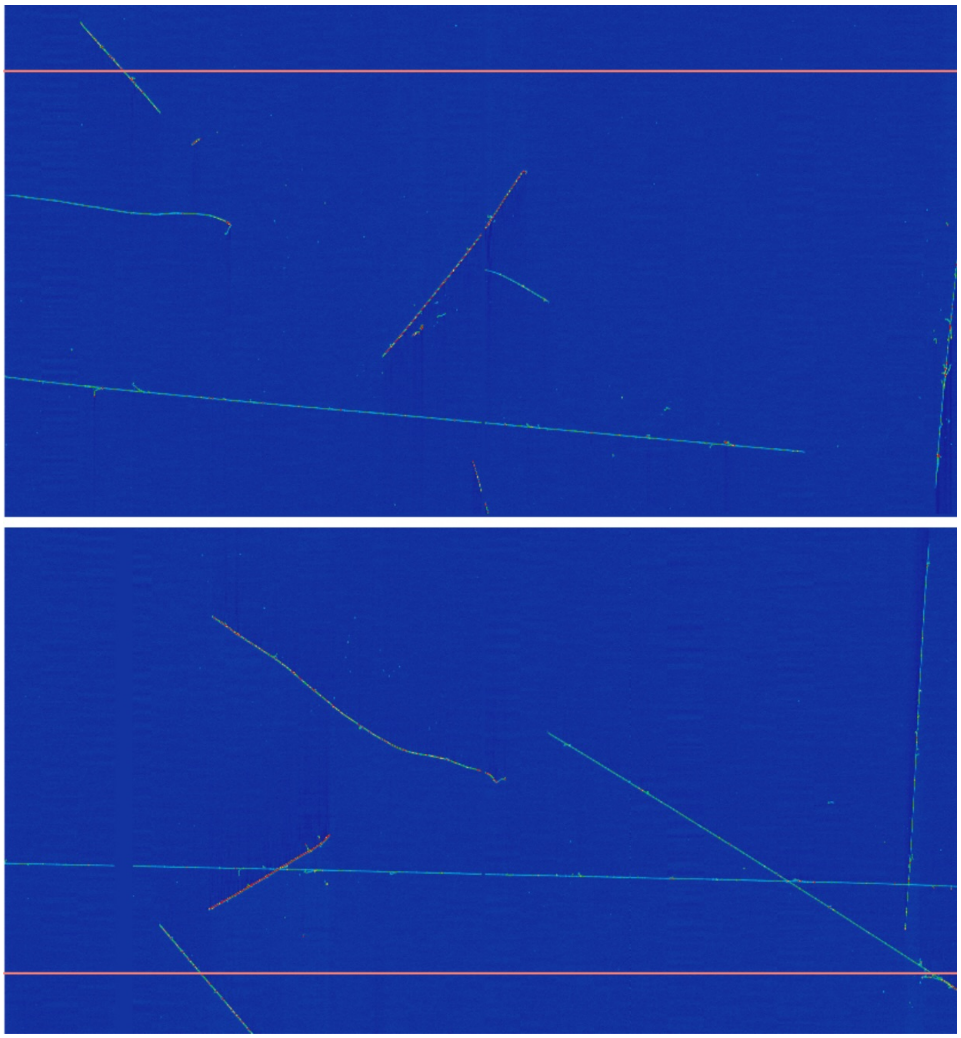

Figure 6.4: Reconstruction of an isochronous event topology, the top panel represents TPC 1 (West) while the bottom panel shows TPC 0 (East). The red lines indicate the anode planes of the TPCs. The visualization is obtained from the vertical collection planes. A distinct isochronous track is visible in TPC 0 (run 18253, subrun 1, event 511972).

6.2 Time correlation CRT ts0 - closest PMT flash

The first study performed to investigate the correlation between the signals from the Photo-Detection System (PDS) and the Cosmic Ray Tagger (CRT) consisted of analyzing the temporal correlation between isochronous CRT tracks and the first optical flash recorded by the PMTs in the TPC crossed by the track.

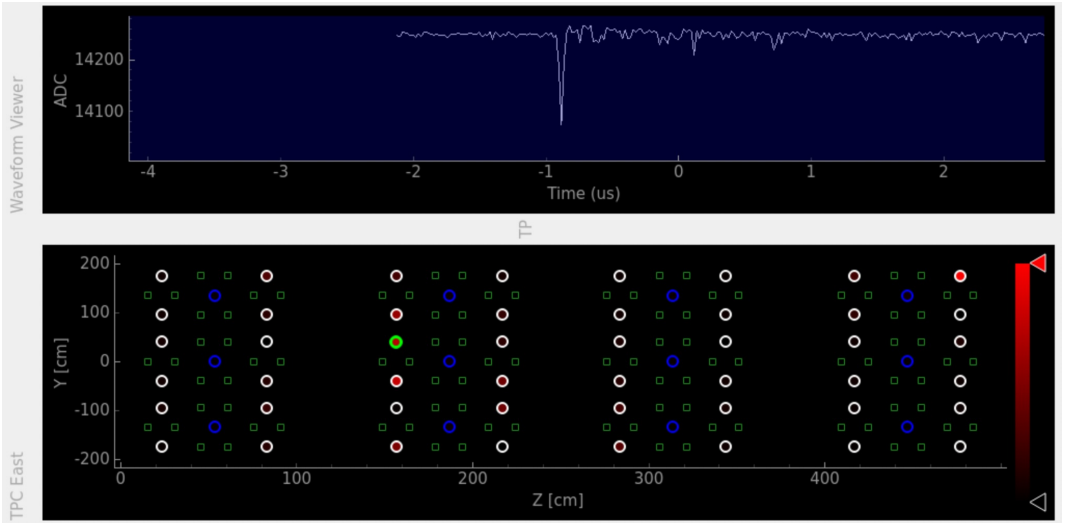

Figure 6.5: Visualization of the PDS data. The figure shows the recorded waveforms for each individual PMT in a given event. Each plot displays the signal in ADC counts as a function of time.

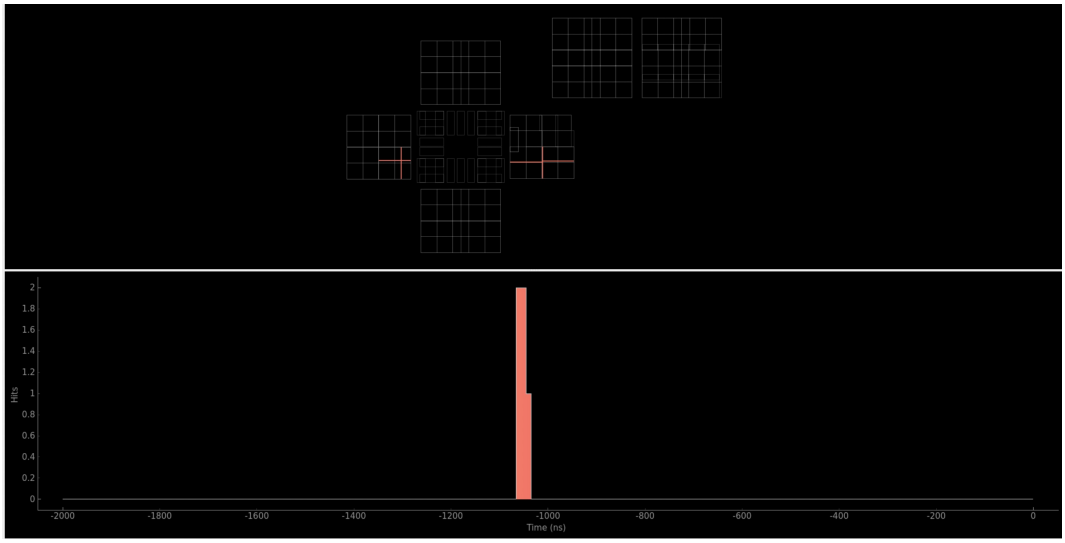

Figure 6.6: Visualization of the data from the CRT. The figure shows two distinct space points where the isochronous track, visible in the TPC, passed through the north and south walls of the CRT.

As a first step, a dedicated ROOT script was developed to select isochronous CRT tracks according to the following criteria:

1. The track is reconstructed with hits in both the North and South taggers, but not in the Top tagger, which identifies it as a through-going (crossing) muon candidate.

2. The start and end x positions are required to lie within the active volume of the TPC, so as to guarantee that the associated optical flashes originate from the muon crossing the detector. Specifically, we require

$$x_{\text{start}},\ x_{\text{end}} \in [-200, 200]\ \text{cm} \quad y_{\text{start}},\ y_{\text{end}} \in [-200, 200]\ \text{cm},$$

   ensuring that the track lie within the projection of the active volume in both x and y directions.

3. The start and end x positions are required to lie within the projection of the same TPC to ensure that the muon does not cross the cathode.

4. The difference in x between the start and end points is required to be less than 20 cm, in order to select only isochronous tracks.

For each selected CRT track, the PMT signals recorded in the corresponding entry of the event tree were analyzed. To identify the first flash among all PMTs, the following selection criteria were applied:

1. The flash is required to be reconstructed in the same TPC as the CRT track.

2. The time difference between the flash and the CRT timestamp is within 1200 ns (where 200 ns is a known offset correction).

In this way, each CRT track was associated with its corresponding PMT flash. Subsequently, the time difference between the flash signal and the CRT $ts0$ was computed:

$$\Delta t = t_{PMT\ flash} - ts0$$

It should be noted that the CRT $ts0$ corresponds approximately to the time at the midpoint of the track, since it is defined as the arithmetic mean of the timestamps of the space points recorded at the two CRT walls.

The resulting distributions of the time differences, obtained separately for the two TPCs, are shown in Figure 6.7. Both TPCs exhibit distributions centered around -100 ns, indicating that, on average, the CRT signal precedes the PMT flash by this amount. The distributions have a width on the order of $O(10\ \text{ns})$, reflecting

both the intrinsic timing resolution of both systems and additional detector and reconstruction effects.

The observed shift between CRT hits and the optical flash distributions is expected. This difference is primarily due to an intrinsic timing offset between the CRT and the PDS, rather than the physics of track propagation itself, as the corresponding time-of-flight for a cosmic muon traveling from the CRT plane to the active liquid argon volume where the flash is reconstructed is only a few nanoseconds.

The goal of this analysis is to understand the factors affecting the spread of these distributions. Some contributions, such as the time-of-flight of cosmic muons, are physical in nature and can be corrected for, whereas others arise from detector effects, representing current limitations of the study. A better understanding of these effects is crucial for improving the timing correlation between CRT and PDS signals, which in turn can enhance the discrimination between incoming and outgoing cosmic-ray tracks and improve background rejection in neutrino interaction studies.

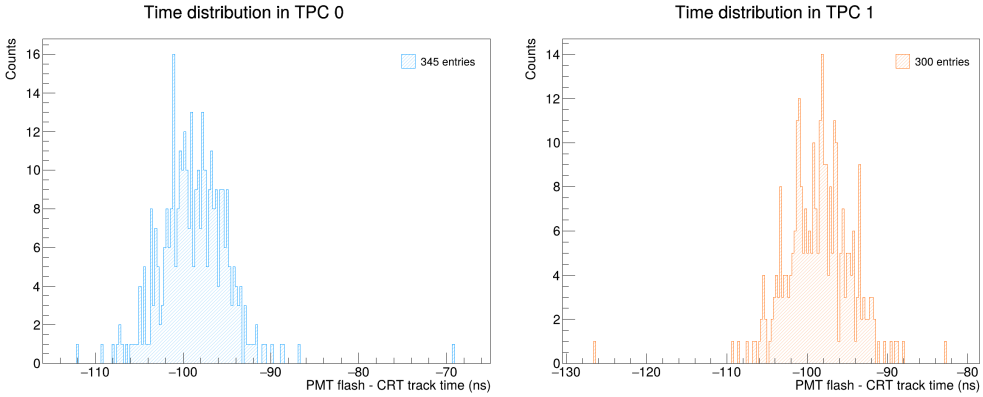

Figure 6.7: Distribution of the time difference between the first PMT flash and the CRT $ts0$ for the two TPCs. The CRT $ts0$ corresponds approximately to the midpoint of the CRT track, defined as the mean of the timestamps of the space points recorded at the two CRT walls. The distributions are centered around −100 ns, indicating that, on average, the CRT signal precedes the PMT flash. The width of the distributions, of the order of $O(10\ \text{ns})$, reflects the intrinsic timing resolution of the system.

6.3 Time correlation CRT ts0 - closest PMT optical Hit

An optical flash is a PMT-related data product that groups together all optical hits in a small coincidence window, expected to result from the same physical origin. Each optical hit corresponds to a digitized and sampled PMT waveform, carrying information on timing (both absolute timestamps and relative to the digitized global trigger signal), amplitude (pulse height and its conversion to photoelectrons), and spatial position (PMT location). The PMT waveforms are sampled over a 10 μs window, which can be extended if an additional flash trigger occurs during this interval. Each optical flash is assigned the timestamp corresponding to the optical hit with the highest pulse height.

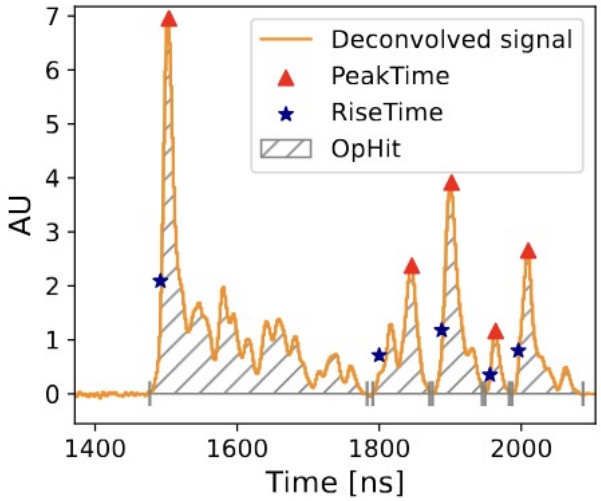

Figure 6.8: Schematic illustration of the structure of an optical flash, which is composed of multiple optical hits. Each hit contributes timing, amplitude, and spatial information to the overall flash signal.

To optimize the CRT–PDS matching, the analysis was refined by studying the detailed structure of optical flashes. Each flash is essentially a collection of individual optical hits, as illustrated in Figure 6.8. Rather than simply selecting the first flash recorded among all PMTs in a given wall, the analysis focused on the first optical hit within each flash and its correlation with the distance of closest approach (DCA) to the selected PMT.

By considering only the first optical hit, the impact of effects such as Rayleigh scattering, which can delay the arrival of light, is reduced. This approach aims to

be sensitive primarily to the most direct path of light to the PMT, ensuring that the DCA provides a good approximation of the true path.

To identify the first optical hit, we iterated over the first flash selected in the initial analysis and extracted the earliest recorded signal. This procedure was repeated for each PMT. The resulting plots associate the time difference between the CRT $ts0$ and the first optical hit with the DCA, which depends on the positions of the two CRT space points and the PMT location, as described in Section 6.1.

The distributions obtained, shown in Figures 6.9 and 6.10, display an unexpected structure characterized by several sub-distributions at different time intervals. Moreover, the distributions vary significantly among different PMTs, whose positions on the TPC wall are shown in Figure 4.10.

6.3.1 Photoelectron distribution in Optical Hits

The approach we adopted to explain the observed distributions was to study the behavior of the time difference as a function of quantities related to both the CRT and the PDS. In particular, we analyzed the relationship between the time difference and the number of photoelectrons recorded by the various PMTs in the optical hits of different events. This analysis was intended to test the hypothesis that signals with different Δt values might be associated with low-photon-count optical hits.

Figures 6.11 and 6.12 show that a number of signals cluster around a primary distribution at $\Delta t < 100$ ns, while a secondary structure emerges at larger Δt values (> 100 ns), characterized by a low photoelectron yield. To distinguish between these two populations, a threshold of 20 photoelectrons was applied: hits with fewer than 20 photoelectrons were classified as belonging to the secondary distribution.

To verify that the issue observed in Figures 6.9 and 6.10 was indeed due to low-photon-count hits, the same type of plots was produced again, this time imposing an additional condition that the first optical hit recorded by the PMT must contain at least 20 photoelectrons. The inclusion of this single condition effectively removed the secondary distributions at higher Δt values, leaving for each PMT a single, narrower distribution with time values approximately in the range $[50, 100]$ ns.

It is important to note that, in addition to eliminating the distributions at different time intervals, this selection also reduced the data sample of "good" tracks. As a consequence, this type of selection could introduce inefficiencies and may need to be implemented differently in future analyses to preserve statistics while still mitigating the effect of low-photon-count hits.

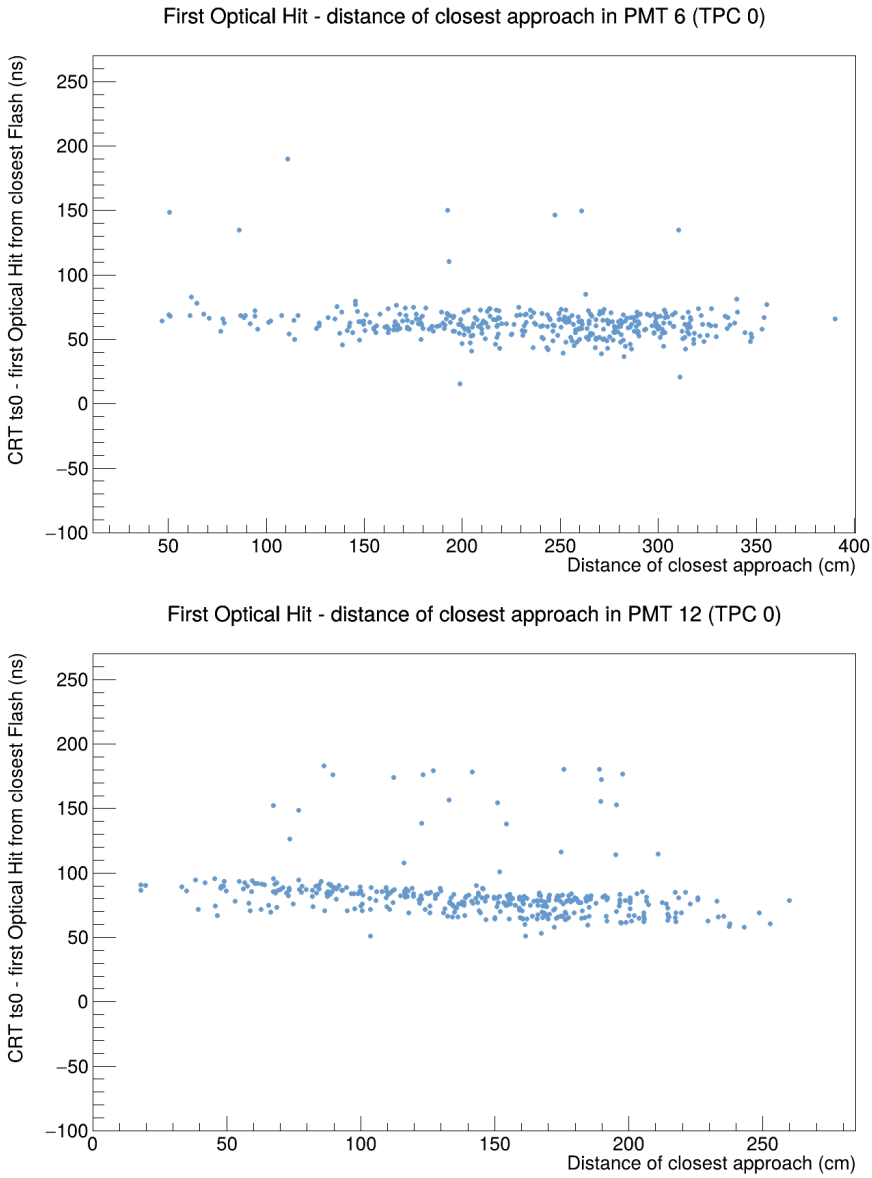

Figure 6.9: Distributions of the first optical hit associated with CRT tracks as a function of the distance of closest approach (DCA) for selected PMTs in TPC 0. Different PMTs exhibit variations in the timing structure of the hits.

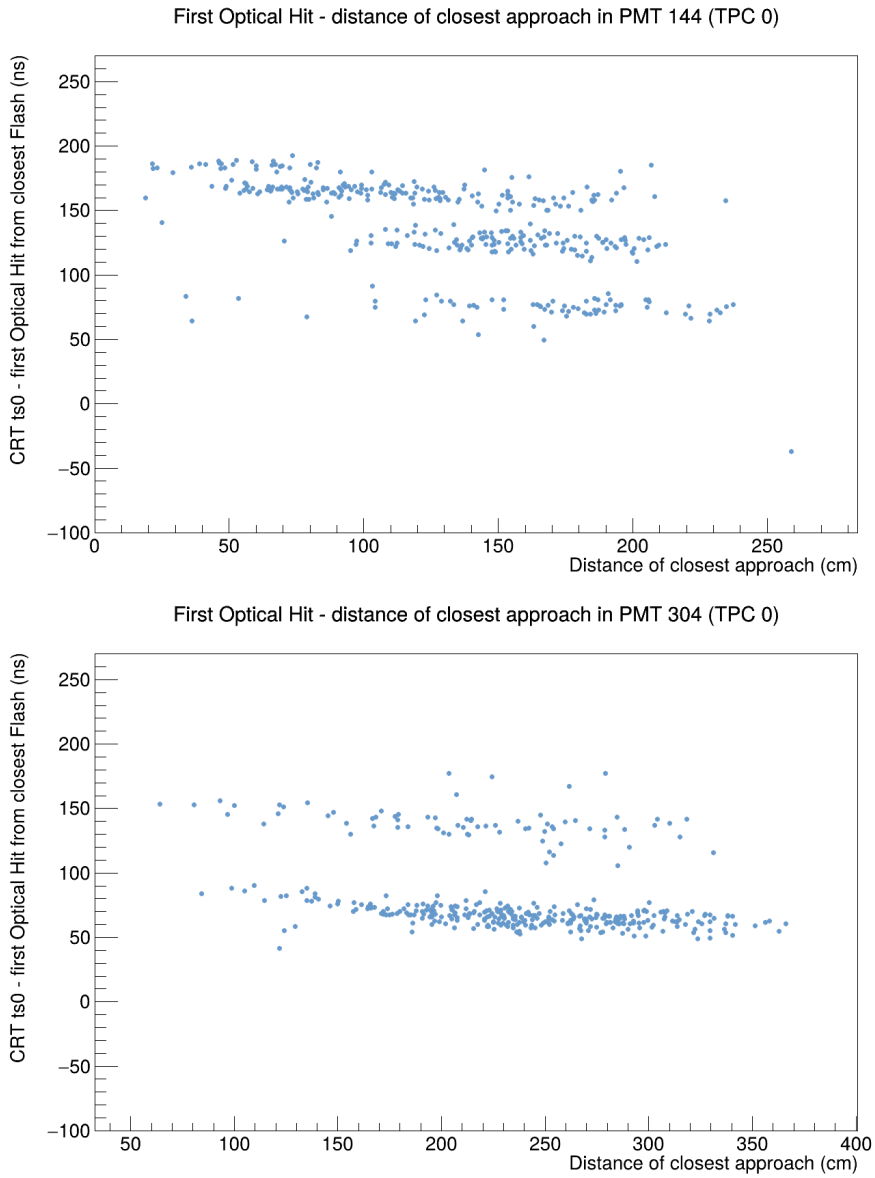

Figure 6.10: Distributions of the first optical hit associated with CRT tracks as a function of the distance of closest approach (DCA) for selected PMTs in TPC 0. Different PMTs exhibit variations in the timing structure of the hits.

6.3.2 Refinement of CRT timing

Thanks to the analysis described in the previous section, we obtained a more precise estimate of the signals produced by the PDS by moving from the first reconstructed

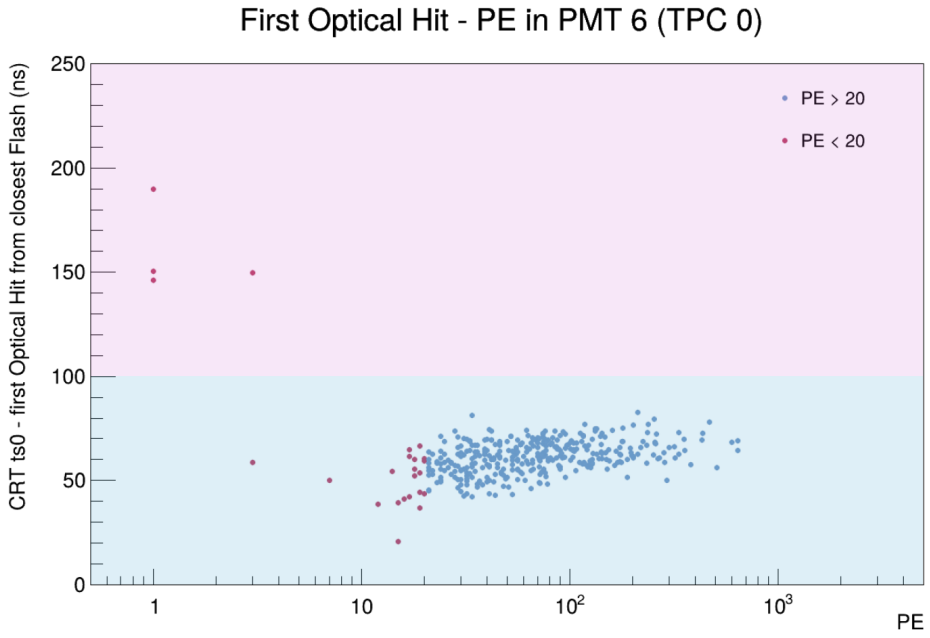

Figure 6.11: Photoelectron distributions for selected PMTs showing the correlation between Δt and the number of detected photoelectrons. The secondary distribution at higher Δt corresponds to low-photon-count hits.

flash to the first optical hit. This provided a more accurate indication of the arrival time of the first scintillation photon produced in liquid argon by the passage of a muon.

In parallel, it is necessary to validate and, if needed, refine the timing information provided by the CRT. In particular, special care must be taken to account for signals recorded by PMTs located at the edges of the detector, where geometric effects may introduce systematic shifts with respect to the simplified assumptions used in the central region.

The first step was to verify the correctness of the CRT track reconstruction algorithm. Specifically, we compared the measured time of flight (TOF) of a muon across the CRT system with the expected track length, assuming that muons propagate at the speed of light. The difference is defined as

$$\Delta t = (TOF \cdot c) - L_{\mathrm{CRT}}, \tag{6.5}$$

where L_{CRT} is the analytically computed track length obtained from the coordinates of the two CRT space points.

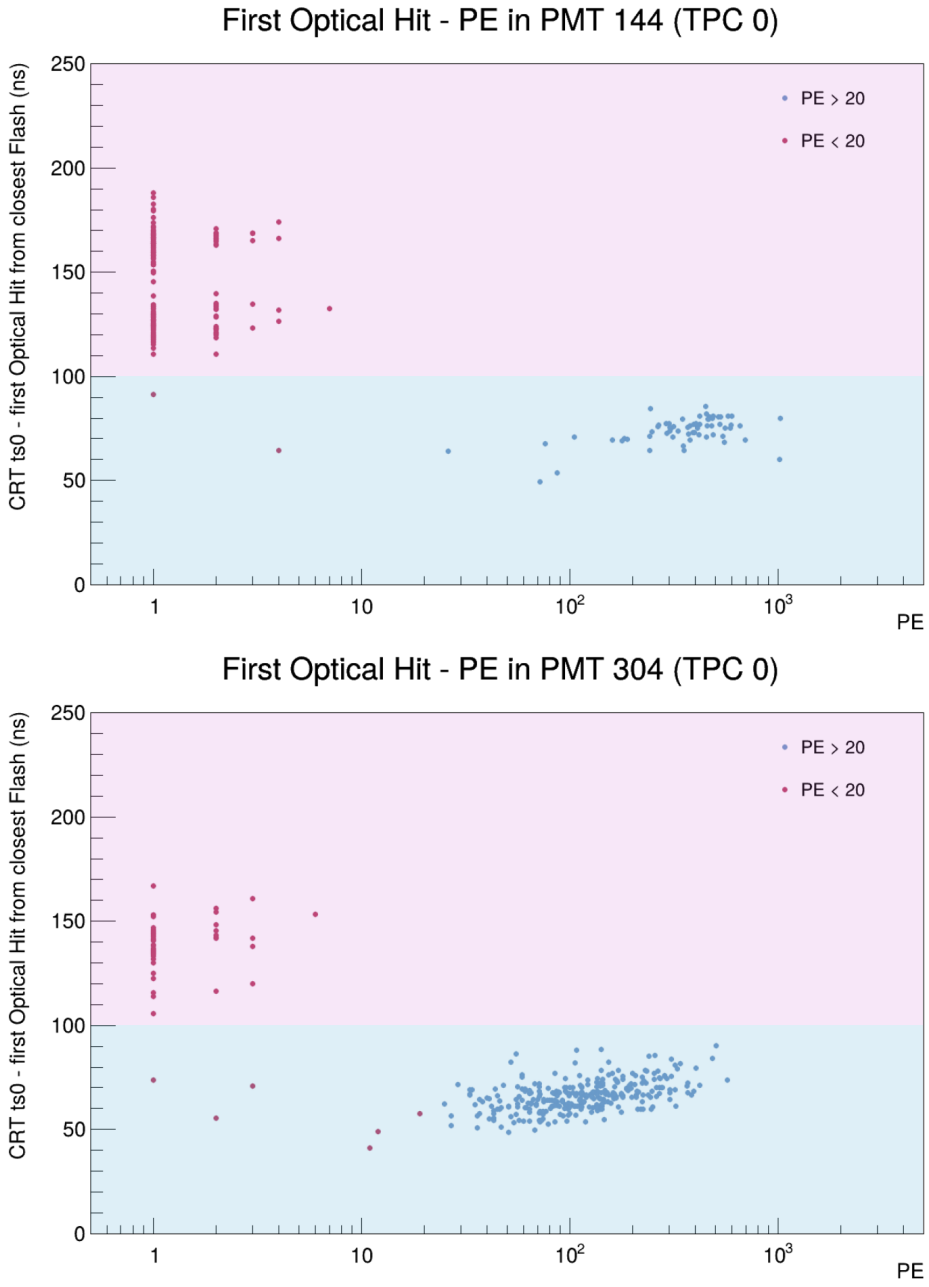

Figure 6.12: Photoelectron distributions for selected PMTs showing the correlation between Δt and the number of detected photoelectrons. The secondary distribution at higher Δt corresponds to low-photon-count hits.

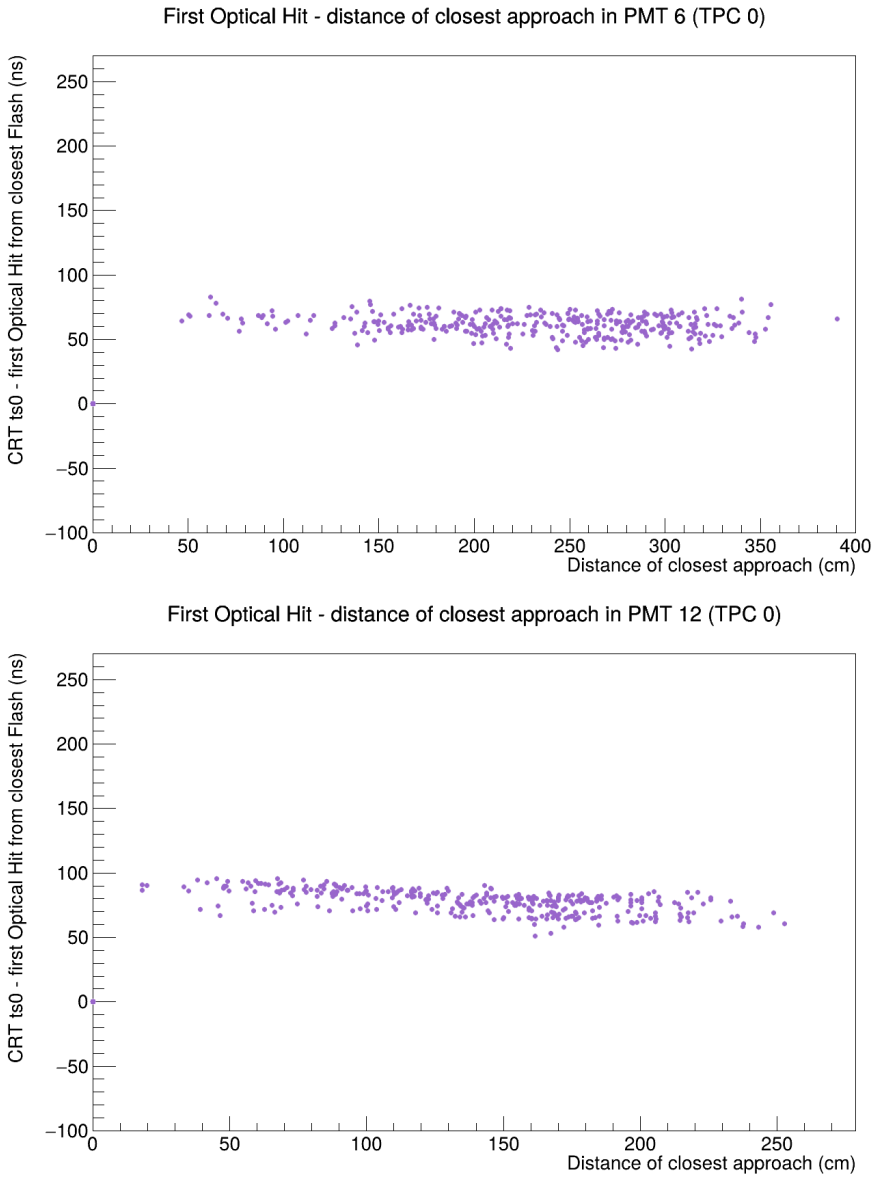

Figure 6.13: Distributions of the first optical hit associated with CRT tracks after applying a minimum threshold of 20 photoelectrons. The secondary high-Δt peaks are removed, leaving a single, narrower distribution.

The resulting distribution is shown in Figure 6.14. As expected, the distribution is approximately Gaussian and centered around zero, confirming the validity of the reconstruction. To improve the quality of the dataset and exclude poorly recon-

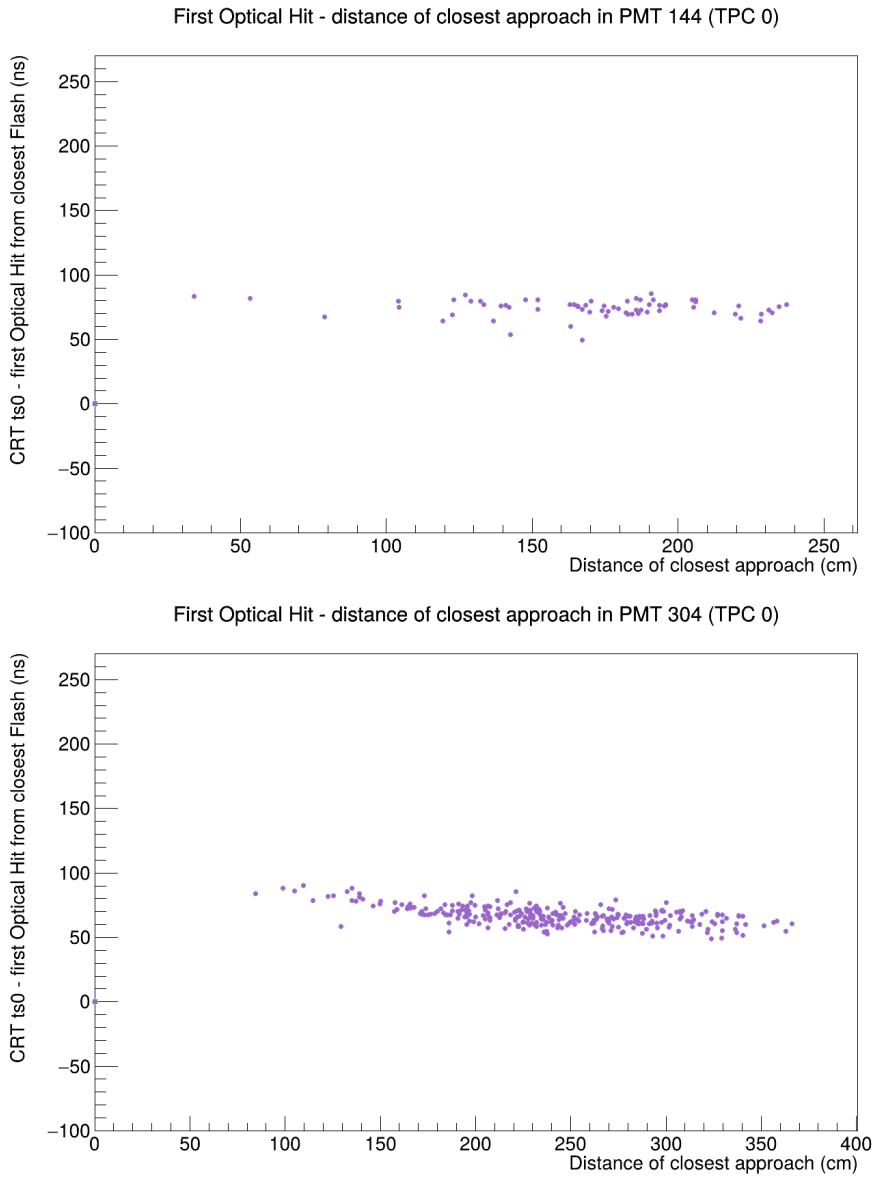

structed tracks, a cut was applied on this difference: only tracks with $|\Delta t| < 5$ ns, corresponding to a maximum deviation of about 450 cm, were retained.

As discussed in Section 6.1, the timestamp $ts0$ assigned to isochronous CRT tracks corresponds to the arithmetic mean of the times recorded at the two space points. This definition provides a good approximation of the average crossing time, and it is accurate for PMTs located near the center of the PDS (e.g. PMTs 144

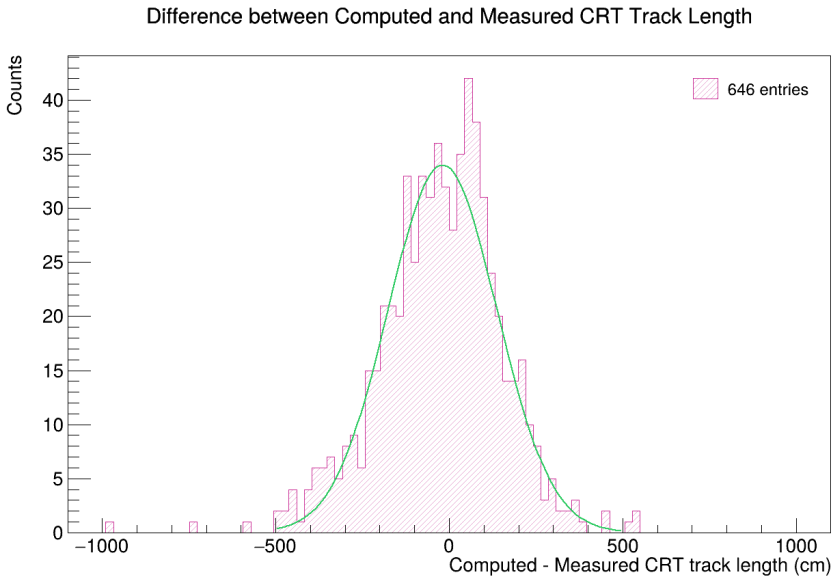

Figure 6.14: Distribution of the difference between the reconstructed CRT track length and the expected value computed from the measured time of flight. The Gaussian distribution centered at zero confirms the accuracy of the reconstruction.

and 145, see Figure 4.10). However, this approximation is less reliable for PMTs positioned near the detector edges, particularly those close to the North or South CRT walls.

To account for this effect, a correction was introduced by redefining the time at the position of closest approach (DCA) to the PMT. The corrected time is computed as

$$t_{closest} = ts0_{sp1} + (ts0_{sp2} - ts0_{sp1}) * \frac{d_{P_{min}}}{total\ length}$$

where $ts0_{sp1}$ and $ts0_{sp2}$ are the timestamps of the two CRT space points, $total\ length$ is the full track length, and $d_{P_{min}}$ is the distance from the first space point to the point of closest approach to the PMT. A schematic representation of the geometry is provided in Figure 6.3.

The effect of this correction is illustrated in Figure 6.15. For central PMTs, the distributions remain essentially unchanged, while for peripheral PMTs the corrected $ts0$ produces a significant improvement. In particular, the apparent double structures observed before the correction collapse into single, narrower distributions once the correction is applied.

A residual slope is observed in the corrected distributions. This effect is inter-

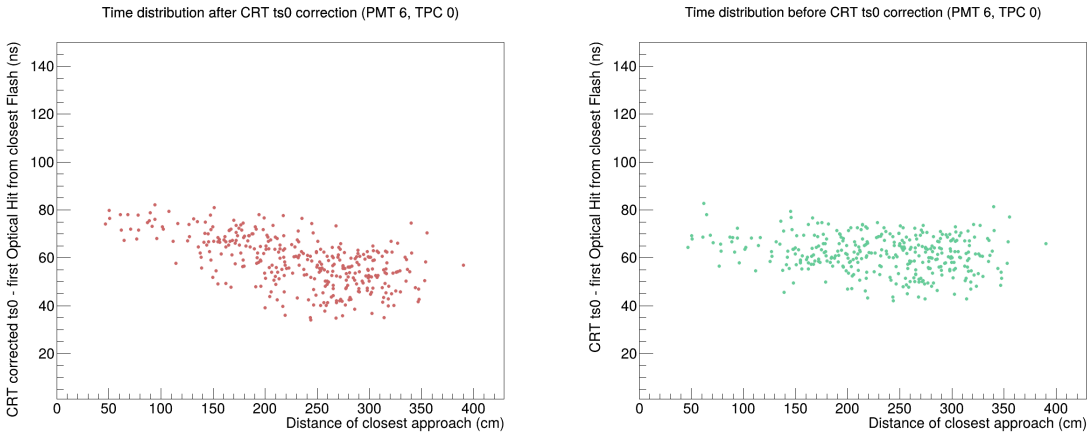

Figure 6.15: Distributions of the time difference between the CRT timestamp and the first optical hit before and after applying the $ts0$ correction, for PMTs located near the detector edges. The correction reduces the spread and eliminates the presence of double structures.

preted as a consequence of the group velocity of scintillation photons propagating from their production point along the muon track to the PMT location. Such behavior will be further investigated in the following sections.

6.4 Group velocity

As previously discussed, the observed distributions can be attributed to the group velocity of photons produced during ionization and subsequently propagating through liquid argon. Preliminary studies indicate that the expected photon propagation velocity is approximately 15 cm/ns.

To extract the effective photon velocity, we computed the inverse of the slope of the best-fit line to the distributions shown in Figure 6.15. In this way, the group velocity is obtained as the ratio between the distance, here represented by the DCA, and the time interval between the emission of the photon at the point along the muon track closest to the PMT and its detection by the PMT, which produces the first optical hit.

In this analysis, however, we slightly modified the selection criteria for isochronous CRT tracks in order to increase the available statistics. Up to this point, we required tracks to cross both CRT planes with start and end space points projected strictly within the lateral boundaries of the TPC, i.e. $x, y \in [-200, 200]$ cm. While this strict requirement ensured high-quality tracks, it also removed a significant fraction

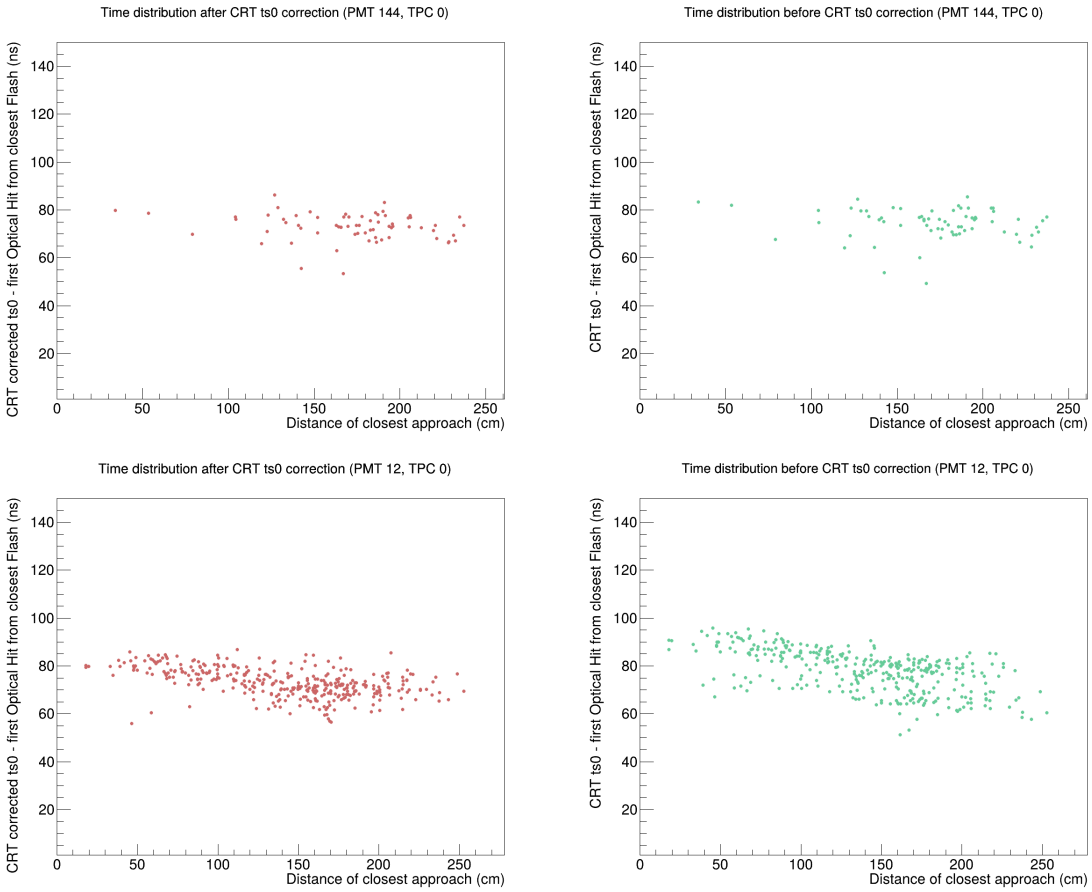

of potentially useful events. To recover statistics, we adopted a looser selection by including all isochronous tracks that maintained an approximately constant distance along the horizontal direction with respect to the cathode and anode, provided that the track segment inside the TPC extended for at least 200 cm. This condition guarantees the production of a sufficient number of scintillation photons (of order 10^7, assuming the energy loss of a Minimum Ionizing Particle), while substantially increasing the statistical sample.

The extracted group velocities were then analyzed separately for different PMTs, taking into account their design differences. In fact, SBND is equipped with 24 PDS boxes, each housing 5 photomultiplier tubes, for a total of 120 PMTs of 8″ diameter. 80% of these PMTs are *coated* with a thin layer of p-terphenyl (pTP or PTB), which acts as a wavelength shifter (WLS). This material absorbs the vacuum ultraviolet (VUV) scintillation light of liquid argon at 128 nm and re-emits it at longer wavelengths, with an emission spectrum peaked around 350 nm and a

broad width of about 50–70 nm. The remaining 20% of the PMTs are *uncoated*, and therefore not directly sensitive to scintillation light. However, they can detect secondary photons, such as those reflected from the cathode (itself covered with a WLS layer) or scattered off neighbouring coated PMTs.

Another refinement introduced in this stage of the analysis was the optimization of the timestamp assigned to the first optical hit. In the standard reconstruction, this value corresponds to the *peaktime* of the signal, i.e. the instant at which the waveform reaches its maximum amplitude. However, this choice introduces a systematic bias, since the actual arrival of the first photons precedes the waveform maximum. To mitigate this effect, we replaced the peaktime with the sum of the *start time* and the *rise time*, which provides a more accurate estimate of the instant when the waveform first departs from the baseline.

6.4.1 Coated PMT

As previously discussed, the coated PMTs are equipped with a wavelength-shifting (WLS) layer that absorbs the liquid-argon scintillation light at 128 nm and re-emits it at longer wavelengths, thereby matching the sensitivity range of the PMTs more effectively. For these PMTs, we therefore expect a correlation between the DCA and the first photon detected, which is directly connected to the photon group velocity in liquid argon. To investigate this, we performed linear fits to the distributions shown in Figs. 6.16 and 6.17, which correspond to TPC 0 (east wall) and TPC 1 (west wall), respectively. The fits were restricted to the region where the linear behavior is most evident, namely for DCA values between approximately 50 and 250 cm. The photon group velocity was then extracted as the inverse of the slope of the fitted line.

This procedure was repeated for all coated PMTs in the two TPCs. The results are summarized in the heatmaps shown in Figs. 6.18 and 6.19. Overall, the extracted group velocities exhibit a strong dependence on the specific PMT under consideration. This behavior is mainly due to the fact that the DCA is not an accurate approximation of the true photon path. Consequently, one should not expect to reliably extract the group velocity using the DCA as the distance estimate.

The missing data are due to PMTs that were either non-functional or turned off during the acquisition of this particular run.

In contrast, this type of analysis is not meaningful for uncoated PMTs. Since these devices are insensitive to direct liquid-argon scintillation light, the detected photons predominantly originate from secondary sources such as cathode re-emission, neighboring PMTs, or Čerenkov light produced by the muons themselves.

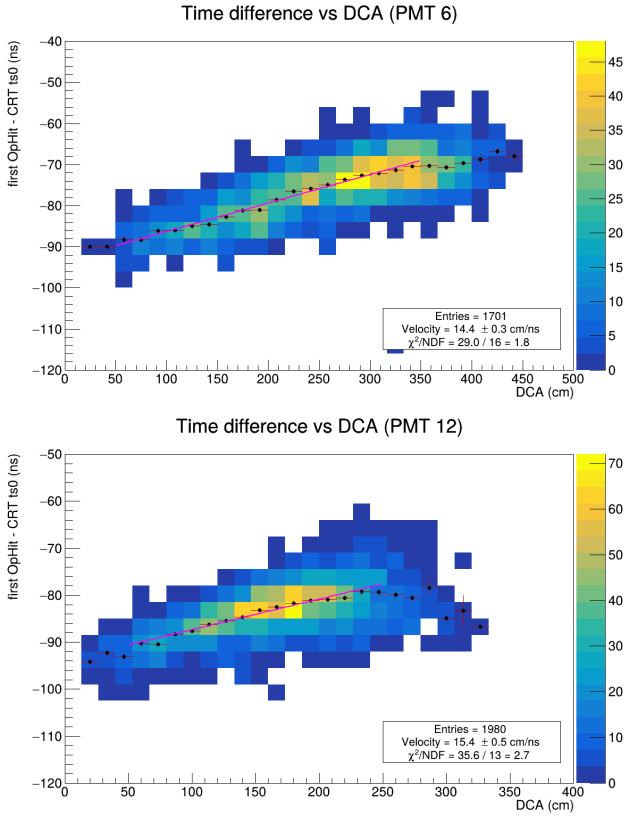

Figure 6.16: Linear fits of the correlation between DCA and the time difference for selected coated PMTs in TPC 0 (east wall). The slope of the fitted line provides an estimate of the photon group velocity in liquid argon.

6.4.2 Uncoated PMT

The distributions correlating the DCA with the time difference between the first optical hit and the CRT signal for the uncoated PMTs are, as discussed earlier, not directly linked to the group velocity of scintillation photons in liquid argon. A few representative examples of these distributions are shown in Figure 6.20.

A characteristic feature emerges in these distributions: for small DCA values ($0 \lesssim \text{DCA} \lesssim 150$ cm), the uncoated PMTs tend to record signals at earlier Δt compared to coated PMTs. At larger DCA values, the distributions become nearly uniform, with no clear dependence on distance.

To better investigate this behavior, the timing profile of an entire PDS box was analyzed. Each box consists of four coated PMTs positioned at the corners of a square and one uncoated PMT placed at the center. The resulting comparison

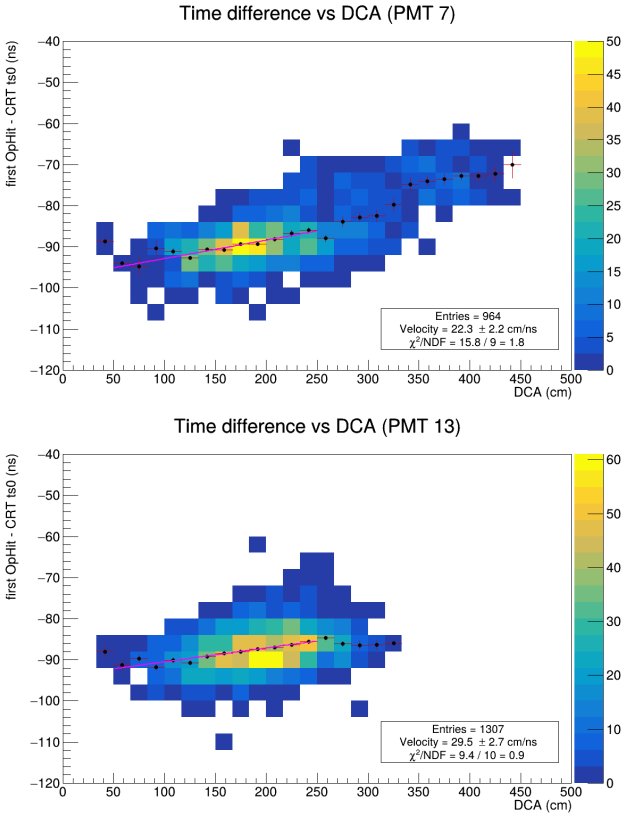

Figure 6.17: Same analysis as in Figure 6.16, but for coated PMTs in TPC 1 (west wall). The extracted slopes confirm the correlation with the photon group velocity.

is shown in Figure 6.21. A systematic trend is visible: for DCA values below $\sim$ 100 cm, the uncoated PMTs consistently register earlier signals than their coated counterparts.

One hypothesis to explain this behavior is the contribution of Čerenkov radiation generated by muons traversing the LArTPC. If the muon velocity exceeds the threshold $\beta > 1/n \approx 0.67$ (where n is the refractive index of liquid argon), which is always the case for relativistic muons, Čerenkov light can be emitted. Unlike scintillation, which produces narrow-band photons at 128 nm, Čerenkov emission spans a broad continuous spectrum, typically in the 200–600 nm range, with intensity scaling as $1/\lambda^2$ and favoring shorter wavelengths. While liquid argon is opaque below $\sim$ 120 nm, it remains transparent across most of the near-UV and visible range, allowing Čerenkov photons to propagate efficiently to the photodetectors.

This spectral difference explains why uncoated PMTs may register earlier signals

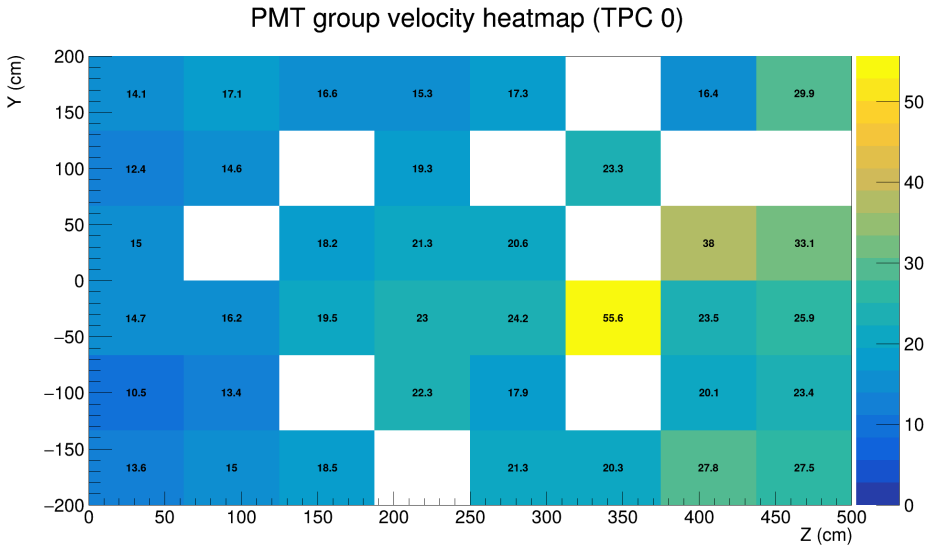

Figure 6.18: Heatmap of the extracted photon group velocities for coated PMTs in TPC 0 (east wall). Variations across PMTs reflect differences in individual timing offsets, which can be corrected using this method.

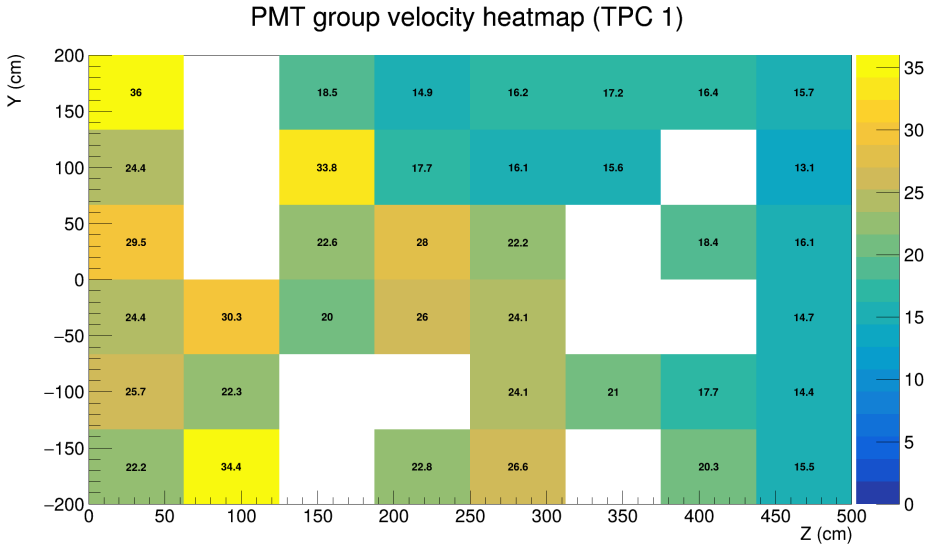

Figure 6.19: Heatmap of the extracted photon group velocities for coated PMTs in TPC 1 (west wall). Similar variations are observed as in TPC 0, confirming the need for PMT-by-PMT timing calibration.

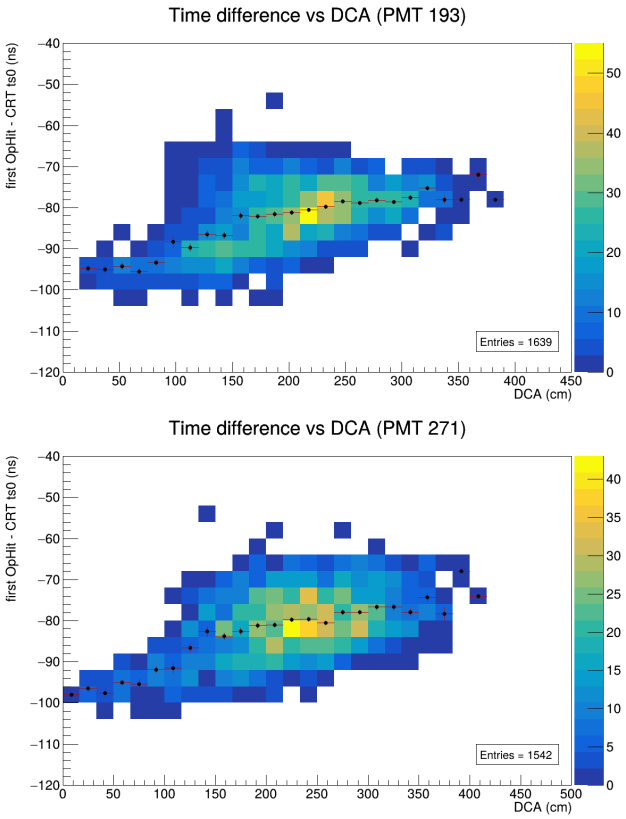

Figure 6.20: Distributions of DCA versus the time difference between the first optical hit and the CRT signal for two uncoated PMTs. These profiles do not exhibit a clear linear correlation with DCA, in contrast to the coated PMTs.

than coated ones. The scintillation light at 128 nm cannot be directly detected by standard PMTs, as this wavelength lies outside their sensitivity range. To make scintillation visible, coated PMTs rely on a wavelength shifter (WLS), this conversion introduces both a delay and additional spatial smearing, since the re-emission occurs at the coating surface. Conversely, uncoated PMTs can directly detect Čerenkov photons in the near-UV/visible range, bypassing the WLS process and therefore recording earlier signals.

Furthermore, while scintillation light has characteristic time components (rise time and decay times of ~ns and ~µs, respectively), Čerenkov emission is essentially instantaneous with the muon passage. This further enhances the likelihood that uncoated PMTs observe an early signal component relative to coated devices. This interpretation is supported by previous studies, which emphasized that in

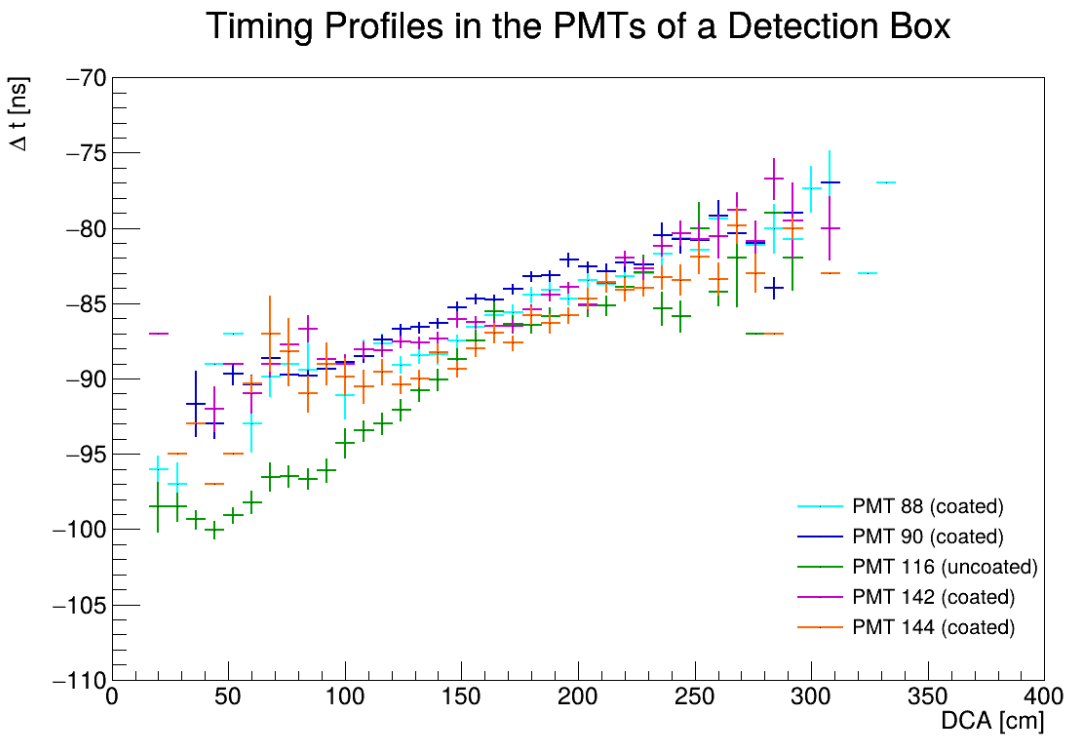

Figure 6.21: Timing profiles of a PDS box, consisting of four coated PMTs and one uncoated PMT. The uncoated device shows systematically earlier signals at small DCA (< 100 cm), possibly due to the detection of prompt Čerenkov light rather than scintillation photons.

LAr the narrow scintillation line at 128 nm leaves the Čerenkov spectrum largely uncontaminated above this wavelength, allowing uncoated detectors to access it directly [19].

This hypothesis was tested by visually inspecting the waveforms recorded by uncoated PMTs. An example is shown in Figure 6.22, where a small bump ($t \sim -1010$ ns) preceding the main scintillation peak can be attributed to Čerenkov radiation produced by the muon, arriving earlier than the scintillation signal detected by coated PMTs. This is consistent with preliminary simulations of the impact of Cerenkov light on PMT waveforms by the SBND PMT group.

6.5 Incoming - Outgoing tracks separation

After obtaining estimates of the group velocity of photons produced by muons traversing the LArTPC, we can finally assess whether the timing information pro-

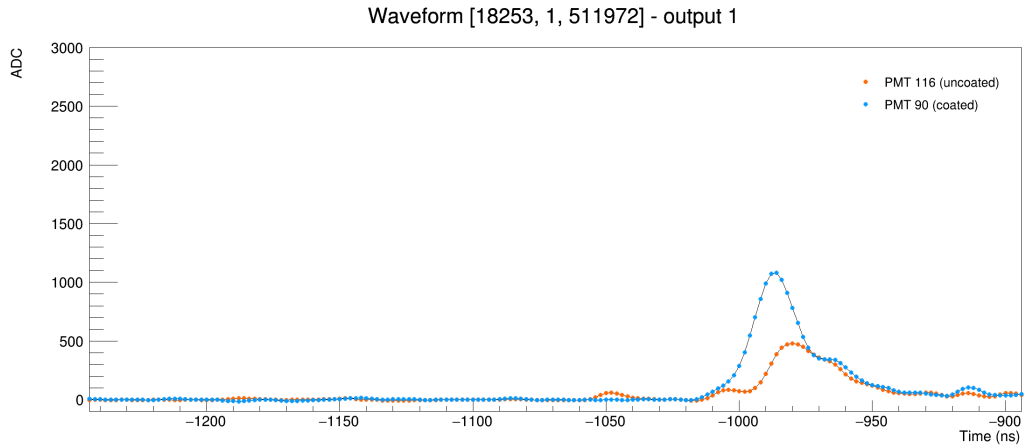

Figure 6.22: Example waveform from an uncoated PMT. The small bump at earlier times (∼ 1010 ns), preceding the main scintillation peak, can be interpreted as Čerenkov radiation produced by the traversing muon.

vided by the CRT and PDS can be effectively exploited to distinguish outgoing tracks, potentially associated with neutrino interactions occurring inside the detector, from incoming tracks, which correspond to cosmic-ray background.

Specifically, for incoming tracks, we expect the CRT signal to precede the PDS signal, whereas for outgoing tracks the opposite behavior should be observed. For this method to be effective, these two distributions must be well separated.

To test this hypothesis, we analyzed the temporal distributions of CRT-PDS signals. Since no dataset recorded during BNB operation was available, we modified the existing crossing-muon sample by partitioning each track into two halves, as illustrated in Figure 6.23.

In this way, we created two categories of tracks:

- **Incoming tracks**: trajectories that hit one of the CRT planes and then stop inside the LArTPC.
- **Outgoing tracks**: trajectories originating inside the LArTPC and leaving a signal in the CRT upon exiting the detector.

For each track, we studied the timing signal from the PMT closest to the midpoint of the segment contained within the TPC, i.e., the PMT with the minimum DCA. The first optical hit from this PMT was identified, and the time difference with respect to the first CRT space point was calculated to simulate the signal produced by an incoming track. Conversely, the difference with respect to the second space

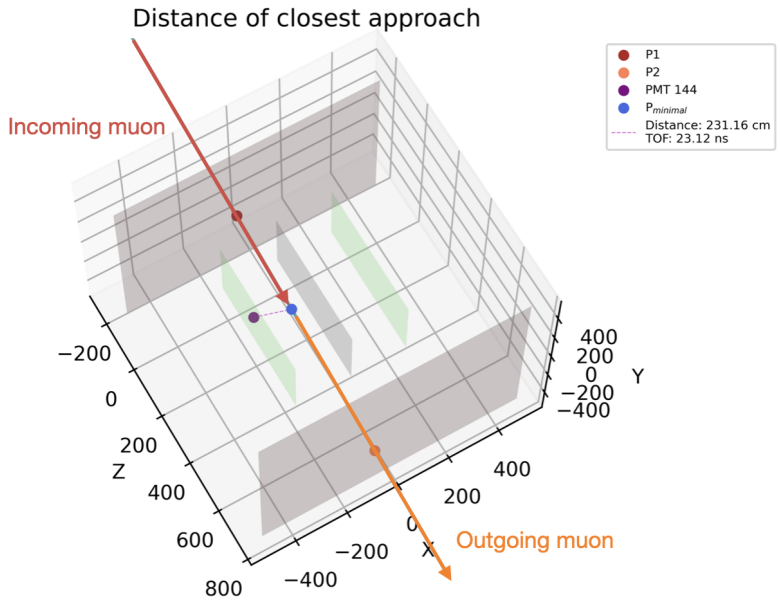

Figure 6.23: This 3D plot shows the reconstructed track of a muon entering and exiting SBND. The red and orange lines represent the incoming and outgoing muon tracks, respectively.

point was calculated to simulate the signal from an outgoing track. Each of these differences was corrected for the time-of-flight of the photons from the track midpoint to the PMT, assuming a reference photon propagation speed of approximately 12 cm/ns.

The resulting distributions are shown in Figure 6.24.

As evident from the figure, the two track categories are clearly separated. This confirms the potential of using CRT-PDS timing correlations as an additional veto to discriminate physically interesting tracks—likely associated with neutrino interactions—from those generated by cosmic-ray background.

In particular, the peaks appear separated by approximately 40 ns, which is consistent with the $O(10\text{ m})$ distance between the north and south walls. The offset from zero indicates a bias between the two systems, possibly due to uncalibrated cable lengths, which still needs to be accounted for. However, this does not affect the results, as the key feature is the separation between the peaks. The efficiency of this method is further highlighted by the minimal overlap observed between the two distributions.

Such a method not only improves background rejection but also enriches the dataset of events that will be collected by SBND in future data-taking campaigns.

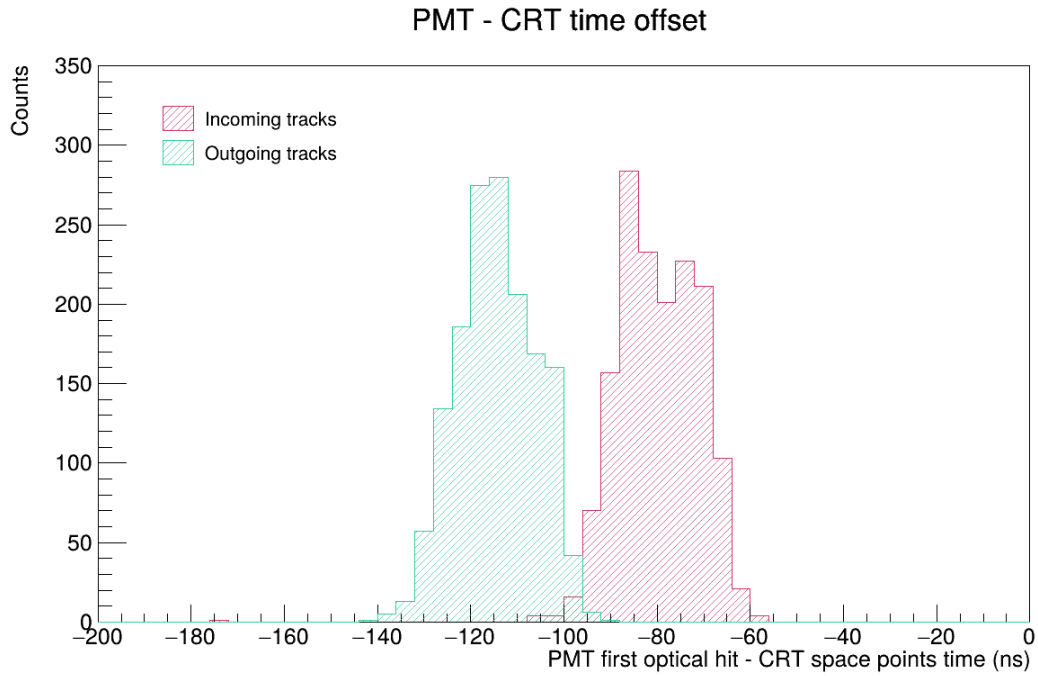

Figure 6.24: Simulated time difference distributions between the first optical hit of the nearest PMT and the CRT space points for incoming and outgoing tracks. Time-of-flight corrections for photon propagation within the LArTPC are applied, assuming a group velocity of 12 cm/ns.

In particular, this timing-based discrimination provides a complementary tool to geometrical selection and optical hit analysis, enhancing the overall capability to identify exiting muons from neutrino interactions with high purity.

It is important to note, however, some limitations of the present study. The approach adopted here effectively maximizes the expected time-of-flight difference by artificially splitting tracks halfway through the TPC. In real scenarios, many entering or exiting muons will traverse only a short distance within the TPC, with their start or end point close to the detector edges. In these cases, the time-of-flight difference would be significantly smaller, making the separation less pronounced and the discrimination more challenging.

7 Conclusions & Outlook

In this thesis, we have presented a comprehensive study on the commissioning, characterization, and performance evaluation of the Cosmic Ray Tagger (CRT) system in the Short-Baseline Near Detector (SBND), with particular emphasis on its timing correlation with the Photon Detection System (PDS). This work systematically addressed key challenges inherent to surface-based liquid argon time-projection chambers (LArTPCs) and developed a methodology that combines hardware validation with detailed software-based event selection. The results obtained demonstrate that the CRT can provide an effective veto against cosmic-induced backgrounds, which constitute the dominant source of contamination in surface detectors, while preserving the efficiency for genuine neutrino interactions. The estimated veto efficiency is about **96.4%**, although this value should be regarded as a lower bound, since in this first study the frequencies measured by individual CRT walls were treated independently, without accounting for correlations between multiple walls.

The analysis of CRT–PDS timing correlations has shown that temporal information can be exploited to distinguish between incoming and outgoing particle tracks. Incoming tracks, primarily due to cosmic rays, exhibit CRT signals preceding the PDS flashes, whereas outgoing tracks, typically associated with neutrino interactions within the LArTPC, show the opposite behavior. By carefully selecting isochronous CRT tracks and analyzing the first optical hits from the PDS, we were able to measure the photon group velocity in liquid argon. These studies revealed that coated PMTs, with wavelength-shifting layers, are sensitive to scintillation light from the LAr at 128 nm, while uncoated PMTs predominantly detect reflected or secondary photons, including contributions from Čerenkov radiation. This distinction allowed us to refine the timing measurements and improve the correlation between CRT and PDS signals, ultimately enabling a more accurate separation of neutrino-induced events from cosmic backgrounds.

To further validate this approach, we simulated datasets of incoming and outgoing tracks by partitioning crossing muon tracks and analyzed the temporal differences between the first optical hit and the CRT timestamps. The resulting distributions demonstrated a clear separation between incoming and outgoing tracks, confirming the feasibility of using CRT–PDS timing information as an additional veto for cosmic

backgrounds. This methodology provides a powerful tool to enrich the neutrino sample and increase the purity of physics analyses in SBND.

While the results presented here constitute a significant step forward, several areas require continued development. Further optimization of the CRT and PDS timing calibrations, improved reconstruction algorithms, and validation on in-beam neutrino data are necessary to achieve the high-precision performance required for oscillation analyses. Moreover, long-term stability studies of the CRT–PDS combined approach will be crucial to ensure reliability over extended data-taking periods.

Looking ahead, SBND plays a central role in the Short-Baseline Neutrino (SBN) program, which aims to definitively probe the sterile neutrino hypothesis and to provide high-statistics measurements of neutrino–argon interaction cross-sections. By precisely characterizing the Booster Neutrino Beam and enabling near–far comparisons with the ICARUS detector, SBND will contribute to resolving longstanding anomalies in neutrino physics. Even in the absence of new physics discoveries, the datasets produced will be invaluable for the modeling of neutrino interactions and for informing the design and analysis of next-generation experiments such as DUNE.

In conclusion, this thesis has demonstrated the capabilities and potential of the SBND CRT–PDS system for precision event selection and cosmic background rejection. The methodologies developed and validated here establish a solid foundation for future physics analyses, and the insights gained will contribute to advancing our understanding of neutrino properties, their interactions in liquid argon, and their role in physics beyond the Standard Model.

Bibliography

[1] C. Andreopoulos, C. Barry, S. Dytman, H. Gallagher, T. Golan, R. Hatcher, G. Perdue, and J. Yarba. **The GENIE neutrino Monte Carlo generator: physics and user manual**. *arXiv preprint arXiv:1510.05494* (2015) (see page 28).

[2] DONuT Collaboration. **Final tau-neutrino results from the DONuT experiment**. *Phys. Rev. D* 78:5 (2008), 052002 (see page 7).

[3] DUNE Collaboration. **Deep Underground Neutrino Experiment (DUNE): Far detector technical design report. Volume I. Introduction to DUNE**. *J. Instrum.*: 8 (2020) (see page 26).

[4] ICARUS Collaboration. **Design, construction and tests of the ICARUS T600 detector**. *Nucl. Instrum. Methods A* 527:3 (2004), 329–410 (see page 35).

[5] ICARUS Collaboration. **ICARUS at FNAL**. *arXiv preprint arXiv:1312.7252* (2013) (see page 36).

[6] ICARUS Collaboration. **The ICARUS experiment**. *Nucl. Part. Phys. Proc.* 306 (2019), 154–162 (see page 37).

[7] KATRIN Collaboration. **Direct neutrino-mass measurement with sub-electronvolt sensitivity**. *Nature Physics* 18:2 (2022), 160–166 (see page 13).

[8] LSND Collaboration. **Evidence for neutrino oscillations from the observation of $\bar{\nu}_e$ appearance in a $\bar{\nu}_\mu$ beam**. *Phys. Rev. D* 64:11 (2001), 22 (see page 16).

[9] MiniBooNE Collaboration. **Significant excess of electronlike events in the MiniBooNE short-baseline neutrino experiment**. *Phys. Rev. Lett.* 121:22 (2018), 221801 (see page 16).

[10] SNO Collaboration. **Direct evidence for neutrino flavor transformation from neutral-current interactions in the Sudbury Neutrino Observatory**. *Phys. Rev. Lett.* 89:1 (2002), 011301 (see page 10).

[11] Super-Kamiokande Collaboration. **Evidence for oscillation of atmospheric neutrinos**. *Phys. Rev. Lett.* 81:8 (1998), 1562 (see page 10).

[12] C. L. Cowan, F. Reines, F. B. Harrison, H. W. Kruse, and A. D. McGuire. **Detection of the free neutrino: a confirmation**. *Science* 124:3212 (1956), 103–104 (see page 6).

[13] J. A. Formaggio and G. P. Zeller. **From eV to EeV: Neutrino cross sections across energy scales**. *Rev. Mod. Phys.* 84:3 (2012), 1307–1341 (see page 28).

[14] C. Giunti and C. W. Kim. **Fundamentals of neutrino physics and astrophysics**. Oxford University Press, 2007 (see pages 6, 9).

[15] Particle Data Group. **Review of particle physics**. *Prog. Theor. Exp. Phys* 2020:510 (2020), 083C01 (see page 11).

[16] Particle Data Group. **Review of particle physics**. *Phys. Rev. D* 110:3 (2024), 030001. DOI: 10.1103/PhysRevD.110.030001 (see pages 14, 29).

[17] K. J. Kelly. **The MiniBooNE Anomaly**. In: *Mini SBN-Theory workshop*. 2021 (see page 13).

[18] I. Kreslo, M. Auger, and D. Lorca. **SBND Cosmic Ray Tracker Design and Performance Technical Note**. Tech. rep. SBN-doc-32663-v1. June 2019 (see pages 40, 44, 54).

[19] L. Lebanowski, J. Klein, and G. Orebi Gann. **Cherenkov and Scintillation in an optical LAr neutrino detector**. In: *APS Meeting Abstracts*. 2023, E12–011 (see page 92).

[20] P. A. N. Machado, O. Palamara, and D. W. Schmitz. **The Short-Baseline Neutrino Program at Fermilab**. *Annu. Rev. Nucl. Part. Sci.* 69 (2019), 363–387. DOI: 10.1146/annurev-nucl-101917-020949. URL: https://doi.org/10.1146/annurev-nucl-101917-020949 (see page 41).

[21] F. Mandl and G. Shaw. **Quantum field theory**. John Wiley & Sons, 2013 (see page 11).

[22] LAr1-ND MicroBooNE and ICARUS Collaborations. **A proposal for a three detector short-baseline neutrino oscillation program in the Fermilab booster neutrino beam**. Tech. rep. SLAC National Accelerator Laboratory, 2015 (see pages 15, 18, 25, 39).

[23] A. Rubbia. **Phenomenology of particle physics**. Cambridge University Press, 2022 (see page 7).

[24] C. Rubbia. **The liquid-argon time projection chamber: a new concept for neutrino detectors**. Tech. rep. 1977 (see page 25).

[25] V. Shiltsev. **Fermilab proton accelerator complex status and improvement plans**. *Mod. Phys. Lett. A* 32:16 (2017), 1730012 (see page 23).

[26] S. Tufanli. **The Short Baseline Neutrino Program at Fermilab**. In: Oct. 2017, 141. DOI: 10.22323/1.314.0141 (see page 21).